OXIDACIÓN FOTOELECTROCATALÍTICA DE GLICEROL CON LUZ VISIBLE USANDO NANOTUBOS DE TiO_2 SENSIBILIZADOS CON $CoFe_2O_4$-ÓXIDO DE GRAFENO

INGRID NATALIA SEQUEDA PICO

UNIVERSIDAD INDUSTRIAL DE SANTANDER
FACULTAD DE CIENCIAS
ESCUELA DE QUÍMICA
MAESTRÍA EN QUÍMICA
BUCARAMANGA
2017

OXIDACIÓN FOTOELECTROCATALÍTICA DE GLICEROL CON LUZ VISIBLE USANDO NANOTUBOS DE TiO_2 SENSIBILIZADOS CON $CoFe_2O_4$-ÓXIDO DE GRAFENO

INGRID NATALIA SEQUEDA PICO

Tesis de grado para optar por el título de Magister en Química

Directora
Dra en Química. MARTHA EUGENIA NIÑO GÓMEZ

Codirector
Dr. en Ciencias Químicas ÁNGEL MANUEL MELÉNDEZ REYES

UNIVERSIDAD INDUSTRIAL DE SANTANDER
FACULTAD DE CIENCIAS
ESCUELA DE QUÍMICA
MAESTRÍA EN QUÍMICA
BUCARAMANGA
2017

Dedication

This work is dedicated to God,
To the life,
To my whole family and my cat.
For the unconditional support,
By the teachings,
By understanding,
For love,
And for everything else,
Thank you.
Natalia Pico

"Todo el mundo es un genio. Pero si juzgas a un pez por su habilidad para escalar un árbol, pasará toda su vida pensando que es un necio"
…Albert Einstein

ACKNOWLEDGMENT

To Universidad Industrial de Santander, Laboratorio en Ciencia de Superficies SURFLAB, Laboratorio de Electroquímica of Centro de Materiales y Nanociencias (CMN) and Centro de Investigaciones en Catálisis (CICAT) for allowing me to develop this research project. To Laboratorio de Difracción de Rayos X, LEAM and CENIVAM for their cooperation. To Universidad de Antioquia (UDEA). To Colciencias and VIE for your generous contribution to the scholarship program at the UIS. To my academic parents Dra. Martha Eugenia Niño and Dr. Ángel M. Meléndez for their dedication, guidance and support. To the teachers who accompanied my professional growth, of which I treasure the knowledge shared in each of their classes. To “chicos cuánticos” who shared their knowledge, dreams, joys with me and created nice bonds of friendship. To “chicos fotoelectroquímicos” because in each seminar something new is learned. To Sergillo, Isaías and Manu who have been great friends. To Pipe for your patience and dedication. To my beautiful “P”. To all those people who by my side made possible the realization of the project and all those who supported me and offered their helping hand in my training as a professional in this wonderful world of knowledge.

TABLE OF CONTENTS

Pag.

1. FUNDAMENTALS AND BACKGROUND 20

1.1 GLYCEROL OVERSUPPLY 20

1.2 ADVANCED OXIDATION PROCESSES FOR WATER DECONTAMINATION 20

1.2.1 Photoelectrocatalytic process 21

1.2.2 Titanium dioxide semiconducting photoelectrodes 22

1.2.3 Titanium dioxide nanotubes as photoanodes 24

1.2.4 Cobalt ferrite and their role as nanotubes sensitizer 24

1.2.5 Graphene oxide in the increment of charge carriers transport 26

2. HYPOTHESIS AND OBJECTIVES 28

2.1 HYPOTHESIS 28

2.2. GENERAL OBJECTIVE 28

2.3 SPECIFIC OBJECTIVES 28

3. EXPERIMENTAL METHODOLOGY 29

3.1 SYNTHESIS OF PHOTOANODES 29

3.1.1 TNT photoanode synthesis 29

3.1.2. TNT modification 29

3.2 CHARACTERIZATION OF PHOTOANODES 30

3.3 PHOTOELECTROCHEMICAL CHARACTERIZATION OF PHOTOANODES 31

3.3.1 Flat band potential determination using F photoelectrode 31

3.4 PEC GLYCEROL OXIDATION ON PHOTOANODES 32

4. RESULTS AND DISCUSSION 33

4.1 MODIFIED HYDROTHERMAL SYNTHESIS 33

4.1.1 Morphological, structural and optical characterization of photoanodes 33

4.1.2 Photoelectrochemical and photochemical characterization 46

4.1.2.1 Flat band potential determination using F photoelectrode 52

4.1.3 Photocatalytic activity of TNT based photoanodes 56

4.2 VARIATION OF THE HYDROTHERMAL MODIFIED METHOD BY USING DIP-COATING TECHNIQUE 58

4.2.1 Morphological, structural and optical characterization of DC-T and DC-TG photoanodes 58

4.2.2 Photoelectrochemical characterization of DC-T and DC-TG photoanodes 66

4.2.3 Photoelectrochemical glycerol oxidation 72

5. CONCLUSIONS 74

6. RECOMMENDATIONS 75

REFERENCES 76

BIBLIOGRAPHY 89

ANNEXES 106

LIST OF FIGURES

Pag.

Figure 1. Schematic representation of PEC using an n-type photoelectrode. 21

Figure 2. Schematic mechanism of charge transport in nanostructured photoelectrodes. 23

Figure 3. Schematic images of photogenerated electron pathway (left) in TNT (101) plane, in transversal (center), and side (right) views. Ti and O atoms are shown as gray and red balls, respectively. Ti5c denotes 5-fold coordinated titanium, O2c 2-fold coordinated and O3c 3-fold coordinated oxygen [14,15]. 24

Figure 4. Schematic diagram of energy band structure of a p-n heterojunction and the charge-carrier separation [20]. 26

Figure 5. FESEM images of (a) cross-section view of the bottom of the TNT arrays and (a',a'') top-view. FESEM images of (b,b',b'') G, (c,c',c'') F, (d,d',d'') FG and (e,e',e'') A-FG photoanodes. 34

Figure 6. FESEM images of F powder. 35

Figure 7. X-ray diffraction profiles of (a) TNT (b) F and (c) FG photoanodes. Diffraction lines of cobalt ferrite (continuous line; PDF-2 000-03-0864), magnetite (mn, dashed line; PDF-2 000-75-0449) and maghemite (mg, dotted line; PDF-2 000-39-1346) phases. Asterisks (*) and "a" lower letter indicate peaks from titanium substrate and anatase phase, respectively. 36

Figure 8. Raman spectra of TNT (a), GO (b), G (c), F (d) and FG (e). $CoFe_2O_4$ (f), γ-Fe_2O_3 (g) and Fe_3O_4 (h) spectra from literature [43] are comparatively presented. Asterisks (*) indicate peaks from anatase phase. 37

Figure 9. XPS high resolution spectra of C 1s, N 1s and Ti 2p of the G, F and FG photoanodes, as indicated in the figure legends. 39

Figure 10. XPS high resolution spectra of Fe 2p, Co 2p and O 1s of the F and FG photoanodes 41

Figure 11. High-resolution transmission electron microscopy images of F powder. 43

Figure 12. Schematic diagrams of a) TNT, b) G and c) FG photoanodes. 44

Figure 13. Modified Kubelka-Munk function vs photon energy of (a) TNT, (b) G, (c) F and (d) FG photoanodes. Inset shows the close up view of absorption spectra. 45

Figure 14. OCP measurements of TNT, G, F, FG and A-FG photoanodes in absence and presence of glycerol as indicated in the figure legends. Inset shows the close up view of A-FG. Measurement conditions: geometric area of 2.4 cm^2, 1 mM glycerol, 0.1 M KH_2PO_4 and K_2HPO_4 at pH 6.8. Light Source: LED driver 655 nm. 47

Figure 15. LSV of (a) F photoanode under illumination of 617, 627 and 655 nm and (b) TNT, G, F, FG and A-FG photoanodes with chopped light of 655 nm. Measurement conditions: active area of 2.4 cm^2, 0.1 M KH_2PO_4 and K_2HPO_4 electrolyte at pH 6.8 and scan rate 0.01 V/s. 48

Figure 16. Photocurrent transients at 0.8 V of TNT, G, F, FG and A-FG photoanodes. Inset is a zoom for all photoanodes. Measurement conditions: active area of 2.4 cm^2, 0.1 M KH_2PO_4 and K_2HPO_4 at pH 6.8. Light source: LED driver of 655 nm. 50

Figure 17. LSV of TNT, G, F, FG and A-FG photoanodes with chopped light of 655 nm. Measurement conditions: active area of 2.4 cm^2, 1 mM glycerol and 0.1 M KH_2PO_4 and K_2HPO_4 electrolyte at pH 6.8 and 10 mV s^{-1}.....51

Figure 18. (a) OCP measurements of TNT photoanode and F photoelectrode under visible light illumination (b) Current-potential curves for the TNT photoelectrode at the scan rate of 0.01 V/s (c) and (d) Mott–Schottky plot calculated from variation of space charge capacitance with the applied potential at different frequencies of TNT photoanode and F photoelectrode, respectively. Solution: 0.1 M KH_2PO_4 and K_2HPO_4 electrolyte at pH 6.8. F photoelectrode illumination source: LED driver (λ = 655 nm). TNT photoanode illumination source: 150 W metal halide (Philips, MHN-TD) with UV-block. TNT photoelectrode active area: 2.4 cm^2. 54

Figure 19. Schematic mechanism of electron transport and photoactivation for TNT/F heterojunction. 55

Figure 20. C/C_o versus time curves of TNT, G, F and FG photoanodes obtained under visible-light irradiation for crude and pure glycerol solutions. 56

Figure 21. Indirect photoelectrocatalytic mechanism of glycerol degradation mediated by hydroxyl radicals according to [112,113]. 58

Figure 22. Top-view FESEM images of (a-a'') DC-T and (b-b'') DC-TG photoanodes. 59

Figure 23. Raman spectra of (a) DC-T (b) Fe_2TiO_5 obtained from literature [114] (c) Ti foil (d) TNT (e) G (f) DC-TG photoanodes. (A) TiO_2 anatase, (*) Fe_2TiO_5, (T) Titanium foil, D and G indicate graphene oxide vibrations. 60

Figure 24. XPS high-resolution spectra of C 1s, O 1s, N 1s, F 1s, Ti 2p and Fe 2p for TNT and DC-TG photoanodes, as indicated in the figure legends.....62

Figure 25. Kubelka-Munk function vs energy absorption of (a) TNT (b) G (c) DC-T and (d) DC-TG photoanodes. Inset shows the zoom view of photon energy. 65

Figure 26. OCP measurements of (a) TNT (b) G (c) DC-T and (d) DC-TG photoanodes. Measurement conditions: active area of 2.4 cm^2, 0.1 M KH_2PO_4 and K_2HPO_4 electrolyte at pH 6.8. Light Source: LED driver λ = 655 nm. 66

Figure 27. OCP measurements of (a) G (b) TNT (c) DC-T and (d) DC-TG photoanodes in presence of glycerol. Measurement conditions: active area of 2.4 cm^2, 0.1 M KH_2PO_4 and K_2HPO_4 and 1 mM glycerol at pH 6.8. Light Source: LED driver λ = 655 nm. 67

Figure 28. LSV of (a) TNT (b) G (c) DC-T and (d) DC-TG photoanodes using chopped light of 655 nm. Measurement conditions: active area of 2.4 cm^2, 1 mM glycerol and 0.1 M KH_2PO_4 and K_2HPO_4 electrolyte at pH 6.8 and 10 mV s^{-1}. 68

Figure 29. LSV of (a) TNT (b) G (c) DC-T and (d) DC-TG photoanodes under chopped light of 655 nm. Measurement conditions: active area of 2.4 cm^2, 1 mM glycerol and 0.1 M KH_2PO_4 and K_2HPO_4 electrolyte at pH 6.8 and 10 mV s^{-1}. 71

Figure 30. Photocurrent transients at 0.8 V of (a) TNT (b) G (c) DC-T and (d) DC-TG photoanodes. Measurement conditions: active area of 2.4 cm^2, 0.1 M KH_2PO_4 and K_2HPO_4 at pH 6.8. Light Source: LED driver λ = 655 nm. 72

Figure 31. C/C_o versus time plots obtained of PEC glycerol oxidation in crude and pure glycerol solutions using TNT, G, DC-T and DC-TG photoanodes.....73

LIST OF TABLES

Pag.

Table 1. XPS single chemical components of TNT, G, F and FG photoanodes. ...42

Table 2. Calculated absorption edges of TNT, G, F and FG photoanodes. 46

Table 3. Photopotential generated by TNT, G, F, FG and A-FG photoanodes in absence and presence of glycerol (V vs Ag/AgCl). 47

Table 4. Difference between photocurrent under illumination and current under dark obtained from LSV plots for TNT, G, F, FG and A-FG photoanodes in the region potential of 0.8 V in absence and presence of glycerol (μA cm^{-2}). 52

Table 5. Retention time and areas acquired from GC obtained for 1 M glycerol solution and solutions obtained from PEC glycerol oxidation after 1 hour, 1.5 hours and 2 hours. The retention times are given in minutes. 57

Table 6. XPS contributions for all photoanodes. 63

Table 7. Photopotential generated by TNT, G, F, FG, DC-T and DC-TG photoanodes in absence and presence of glycerol (V vs Ag/AgCl 3 M KCl). 68

Table 8. Difference between photocurrent under illumination and current under dark conditions generated by TNT, G, F, FG, A-FG, DC-T and DC-TG photoanodes (μA cm^{-2}). 69

LIST OF ANNEXES

Pag.

ANNEX A. Crude glycerol composition supplied by Biocombustibles Sostenibles del Caribe S.A. 106

ANNEX B. Wide-scan XPS spectrum and high-resolution spectra of C 1s, N 1s, F 1s, Ti 2p and O 1s for TNT 107

ANNEX C. Wide-scan XPS spectra of G, F and FG photoanodes, as indicated in the figure legends. 108

ANNEX D. Mott-Schottky equation to obtain flat band potential 109

ANNEX E. Gas chromatography spectrum of glycerol solution at the first 20 minutes of reaction using FG photoanode under visible light illumination 110

ANNEX F. Mass spectra fragmentation obtained from peaks in glycerol solution at the first 20 minutes of reaction using FG photoanode under visible light illumination 111

RESUMEN

TÍTULO: Oxidación fotoelectrocatalítica de glicerol con luz visible usando nanotubos de TiO_2 sensibilizados con $CoFe_2O_4$-óxido de grafeno*****

AUTOR: SEQUEDA PICO, Ingrid Natalia******

PALABRAS CLAVES: nanotubos de TiO_2, ferrita de cobalto, óxido de grafeno, fotoelectrocatálisis, glicerol

Electrodos basados en nanotubos de TiO_2 modificados con $CoFe_2O_4$ y óxido de grafeno (FG) fueron obtenidos por síntesis hidrotérmica modificada y fueron comparados con aquellos obtenidos usando la técnica dip-coating (DC-TG). El efecto del aumento de la cantidad de óxido de grafeno (GO) en la fotoelectroactividad de los fotoánodos fue estudiado. Los fotoánodos de TiO_2 (TNT) modificados con ferrita de cobalto (F) y óxido de grafeno (G) fueron preparados para mostrar el efecto sinérgico entre ambos modificadores. Las micrografías FESEM del fotoánodo FG mostraron la formación de nanotubos verticalmente orientados con granos y aglomeraciones sobre estos. Los resultados de XRD y espectroscopia Raman mostraron la presencia de anatasa, ferrita de cobalto, magnetita, maghemita y óxido de grafeno en el fotoánodo FG, mientras que la fase Fe_2TiO_5 fue observada en el fotoánodo DC-TG. El análisis de XPS evidenció el dopaje de los TNT con nitrógeno, carbono y flúor durante el proceso de anodización electroquímica y con hierro durante la modificación. Los resultados de DRS mostraron un desplazamiento de la absorción hacia la región visible en los TNT y los DC-TG, mientras que los fotoánodos FG presentaron absorciones en todo el intervalo visible. Un incremento en el transporte de electrones en el fotoánodo FG fue observado en un medio neutro de fosfato cuando se incorporó el GO. Las posiciones de las bandas de valencia y conducción estimadas electroquímicamente mostraron un alineamiento favorable para la inyección de electrones desde la ferrita de cobalto hacia los nanotubos de TiO_2. La degradación fotoelectrocatalítica en una celda de tres electrodos empleando los fotoánodos FG y DC-TG alcanzó una conversión del 82% y 90% respectivamente, durante la oxidación fotoelectroquímica de glicerol bajo iluminación con luz visible en una hora.

_____

* Trabajo de Investigación

** Facultad de Ciencias, Escuela de Química. Directores: Dra. Martha Eugenia Niño Gómez, Profesor Dr. Ángel Manuel Meléndez Reyes.

ABSTRACT

TITLE: Photoelectrocatalytic oxidation of glycerol with visible light using TiO_2 nanotubes sensitized with $CoFe_2O_4$-graphene oxide*****

AUTHOR: SEQUEDA PICO, Ingrid Natalia******

KEYWORDS: TiO_2 nanotubes, cobalt ferrite, graphene oxide, photoelectrocatalysis, glycerol

TiO_2-based electrodes modified with $CoFe_2O_4$ and graphene oxide (FG) were obtained using the modified hydrothermal synthesis and were compared with those obtained using dip-coating technique (DC-TG). The effect of increasing the amount of graphene oxide (GO) on the photoelectroactivity of the photoanodes was studied. TiO_2 photoanodes (TNT) modified with cobalt ferrite (F) and graphene oxide (G) were prepared to study the synergistic effect between both modifiers. FESEM micrographs of FG showed nanotubes vertically oriented with grains and agglomerations on the top. XRD and Raman spectroscopy results showed the presence of anatase, cobalt ferrite, magnetite, maghemite and graphene oxide in FG photoanode, while Fe_2TiO_5 phase was observed in DC-TG. XPS analysis revealed the doping with nitrogen, carbon and fluorine during anodization process and with iron during modification. DRS results showed an absorption displacement towards the visible range of TNT and DC-TG, while FG photoanodes presented absorptions throughout the visible light range. An increment of electrons transport in FG in neutral phosphate medium was observed when GO is incorporated. Band positions estimated electrochemically showed a favorable alignment in the electron injection from the modifier oxides to the TiO_2 nanotubes. The photoelectrocatalytic degradation in a three electrodes cell using FG and DC-TG reached a conversion of 82% and 90% respectively, during PEC glycerol oxidation under visible light illumination for one hour.

_____

* Investigation project

** Facultad de Ciencias, Escuela de Química. Advisers: Dra. Martha Eugenia Niño Gómez, Professor Dr. Ángel Manuel Meléndez Reyes.

INTRODUCTION

In the last years, the world industry of transesterification of palm oil for biodiesel production has been increasing notably. The crude glycerol derived from this process achieves enormous amounts, which is characterized by low purity levels. Many efforts have been carried out to purifying the crude glycerol but the high costs becoming it in an environmental issue. The photoelectrocatalysis (PEC) has been considered as a potential process to remove organic pollutants of water, it involves the use of semiconducting photoanodes composed generally by TiO_2. This has motivated the modification of TiO_2 photoanodes to improve its performance. Aiming to contribute to improve the electronic transport through TiO_2 and extent its photoactivity in the visible region, modification of TiO_2 nanotube arrays (TNT) with both $CoFe_2O_4$ (F) and graphene oxide (GO) is proposed. Being the PEC a promising technology, the modification of TNT with $CoFe_2O_4$ by a hydrothermal method was studied. Morphological, structural, optical and photoelectrochemical properties of FG photoanodes and their effects on photoelectrocatalytic performance are herein presented and compared with another modification by using dip-coating technique (DC-T and DC-TG).

1. FUNDAMENTALS AND BACKGROUND

1.1 GLYCEROL OVERSUPPLY

Annually huge amounts of contaminants are being discarded causing damage to the environment [1]. In the last 5 years, almost 20 million of m^3 of biodiesel has been produced of which 10% correspond to crude glycerol [2]. This has generated a crude glycerol oversupply with purity levels about 50-75%, which represents an issue [2]. Some researches has proposed to purify the crude glycerol or become in value-added products, however, those processes has usually high cost [3]. An alternative against to pollution is the use of solar energy which is one of the most clean and accessible energy sources in the world [4]. The solar light energy has been widely used in water decontamination [1,4], and its application in Advanced Oxidation Processes (AOP's) is friendly with the environment [5].

1.2 ADVANCED OXIDATION PROCESSES FOR WATER DECONTAMINATION

Since 1980s the concept of AOP's has been recognized [5]. AOP's are based on the intermediacy of highly reactive species as hydroxyl radical ($OH^{\bullet}$), which are powerful oxidants for organic contaminants oxidation [6]. Recently, new AOP's based on electrochemical technology has been appeared [6]. Some advantages as high efficiency, possibility of automation, safety (have into account the operation conditions), and the wide range of applicability become these technologies promising in wastewaters decontamination [6]. AOP's include process as heterogeneous, homogeneous and photoelectrocatalytic methods, in which, the last one has attracted considerable attention.

1.2.1 Photoelectrocatalytic process. Researches in PEC have been increased notoriously, because it takes advantage of photocatalytic and electrochemical processes to obtain greater efficiencies in water decontamination. PEC is based on irradiation of a photoelectrode with a suitable band gap and the application of constant bias potential, where $OH^{\bullet}$ are generated at the photoanode surface. The applied potential causes that photogenerated electrons being transported through the external circuit of the cell, favoring the generation of holes and hence enhancing the efficiency in regard to photocatalysis [6]. One of their principal advantages of PEC is the decrease of charge carriers recombination. Fig. 1 shows the scheme of the photoelectrochemical process when a photoanode is used.

Figure 1. Schematic representation of PEC using an n-type photoelectrode.

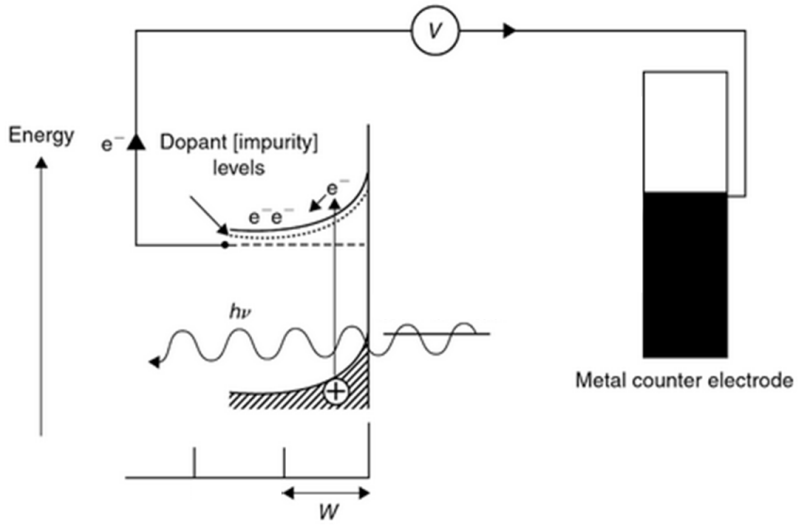

When the photoanode is put in contact with an electrolyte, a charge transfer is carried out, hence a rearrangement through the interface matches the Fermi level of the solution with the Fermi level of the photoanode [7]. In the rearrangement, electrons are transferred to the solution, while inside photoanode the formation of a space charge layer is given by the electrons diminution on photoanode surface. When a bias potential is applied, an electric field generated into semiconductor

promotes the separation of electron-hole pairs photogenerated. Thereby, photogenerated holes within the depletion layer can be efficiently transported toward the semiconductor/electrolyte interface, where they can form hydroxyl radicals, while electrons diffuse to the back contact [7].

1.2.2 Titanium dioxide semiconducting photoelectrodes. The increasing amount of PEC researches has focused on obtaining high performance reactions using mostly semiconducting photoanodes with high chemical stability, non-toxicity and high cost-effective relation. Titanium dioxide (TiO_2) photoelectrodes has been extensively used due to properties as high stability, low toxicity and wide band gap becoming it in a promissory material [8]. Accordingly to TiO_2 band gap, the minimum energy required to promote electron-hole pairs photogeneration is 3.2 eV (for anatase structure) which are directly related in reduction-oxidation reactions. Thus, the irradiation of TiO_2 photoelectrodes with energy, $\lambda < 380$ nm, promotes that electron and holes are generated as shown in (1).

$$TiO_2 + h\upsilon \rightarrow e_{CB}^- + h_{VB}^+ \quad (1)$$

Then, organic compound can be oxidized directly by holes (2) or indirectly by $OH^{\bullet}$ (3) and (4) on TiO2 surface as follows:

$$TiO_2 + h^+ + R - H \rightarrow R^{\bullet} \rightarrow \text{Oxidation products} \quad (2)$$

$$TiO_2 + h^+ + H_2O \rightarrow TiO_2\,[OH^{\bullet}] + H^+ \quad (3)$$

$$TiO_2\,[OH^{\bullet}] + R - H \rightarrow R^{\bullet} + H_2O \quad (4)$$

Since the TiO_2 nanostructured photoelectrodes were obtained, many studies about the charge carrier diffusion and photoactivation enhancement has been conducted. The charge-transport is given by electrons transport through the interconnected

particles and holes diffusion to particles surface creating a potential gradient [9]. Consequently, charge separation has no dependence with electric field application, but is determined by transference kinetics on semiconductor/electrolyte interface. In the nanostructured photoelectrodes, the only existence of a surface introduces intrinsic surface states. Also, defects and impurities species introduce extrinsic surface states. The presence of those states could limit electron diffusion by trap-limited diffusion process, in which states localized inside band gap could acts as recombination centers or trap states [10]. In Fig. 2 is shown a schematic mechanism of generation of electron-hole pairs when a semiconductor film is illuminated. The electron in conduction band can combined with the formed hole in a recombination process, can be trapped by bulks traps or can be trap and release by surface traps and can be transfer to species in solution [11]. The surface states are localized physically on particles surface or within a distance from it [11].

Figure 2. Schematic mechanism of charge transport in nanostructured photoelectrodes.

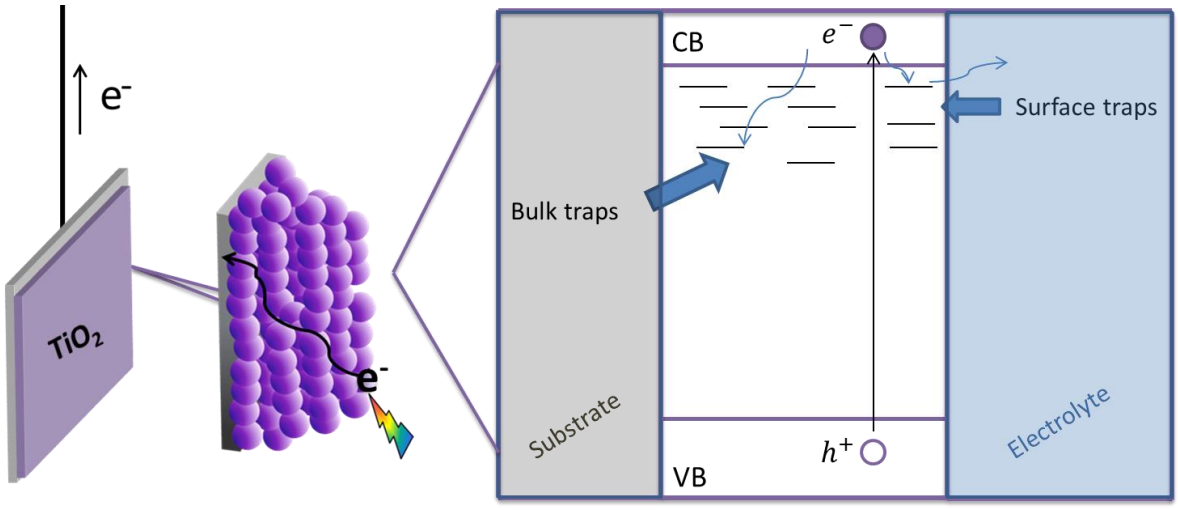

1.2.3 Titanium dioxide nanotubes as photoanodes. As it is well known, there is a dependence of the morphology with the photoelectrodes performance. As shown above, the random particles promote slow electrons diffusion which limits hugely the process efficiency (Fig. 2). In contrast, the TiO_2 crystalline nanotube arrays (TNT) promotes excellent pathways for charge transfer improving the transport and collection of charge carriers [12]. The TNT architecture provides high surface area to harvest solar light for higher energy conversion [13]. Also, the arrangement of the TNT fabricated by electrochemical anodization has a very strong mechanical strength due to TNT grows directly on titanium substrate [13]. Fig. 3 shows the direct pathway to electrons transport and a schematic crystalline anatase structure of TNT in (101) plane.

Figure 3. Schematic images of photogenerated electron pathway (left) in TNT (101) plane, in transversal (center), and side (right) views. Ti and O atoms are shown as gray and red balls, respectively. Ti5c denotes 5-fold coordinated titanium, O2c 2-fold coordinated and O3c 3-fold coordinated oxygen [14,15].

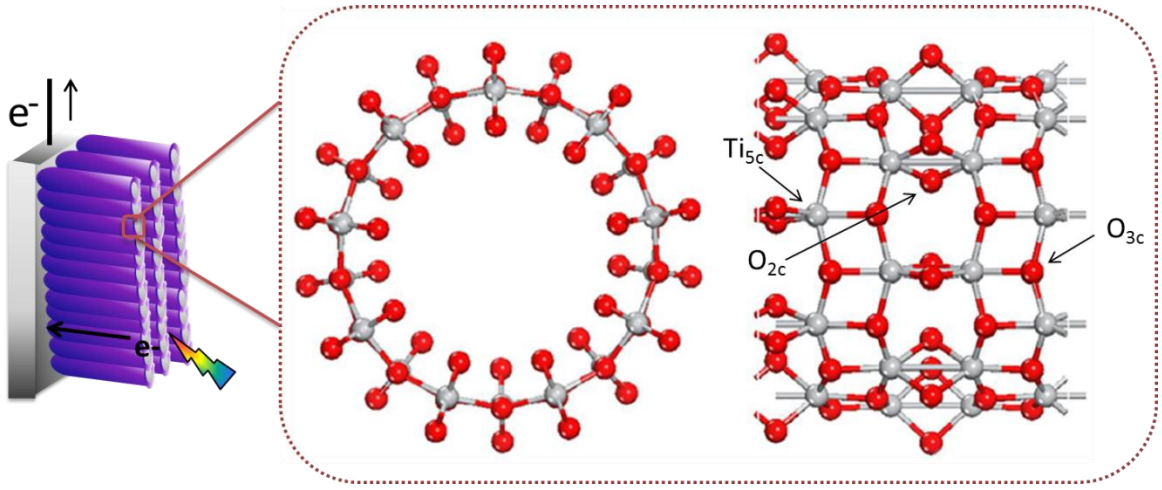

1.2.4 Cobalt ferrite and their role as nanotubes sensitizer. Although TNT has great properties, its wide band gap ~3.2 eV limits the technological applications. Intrinsically, the material absorbs light in UV region, only about 4-5 % of solar

spectrum [16]. From the point of view of solar energy applicability, is necessary extend TNT absorption from UV to visible light region, which corresponds to ~46% of solar light [17]. Extensive efforts have been made to improve the TNT visible light absorption; these include metal and non-metals doping. Although these researches have improved the visible light absorption, issues as carrier-recombination centers and thermal instability generates the necessity of focus investigations on additional strategies [18]. One of the strategies to extend absorption from UV to visible light region is the combining TNT with narrow band gap semiconductor. This combination is also known as heterojunctions which were suggested for first time by Shockley in 1951 [19].

The p-n heterojunctions has been greatly known for the highly efficient charge collection and separation [20,21]. Generally, when p-type and n-type semiconductors are in contact, a p-n heterojunction is formed (Fig. 4). In the interface is produced a space-charge region by electron diffusion creating a built-in electrical field. The electron diffusion from n-type to p-type semiconductor results in the generation of negative charge accumulated in p-type region near to the junction. Likewise, holes diffuse from p-type to n-type semiconductor creating positive charges near the junction in the n-type region. When heterojunction is illuminated with photons energy higher or equals to their band gaps, electrons and holes photogenerated are separated efficiently. The electrons in p-type are transferred to the CB of the n-type semiconductor and the holes to the VB of the p-type. Advantages as more effective charge separation, rapid charge transference, longer lifetimes of the charge carriers and separation of locally incompatible reduction and oxidation reactions are provided.

Figure 4. Schematic diagram of energy band structure of a p-n heterojunction and the charge-carrier separation [20].

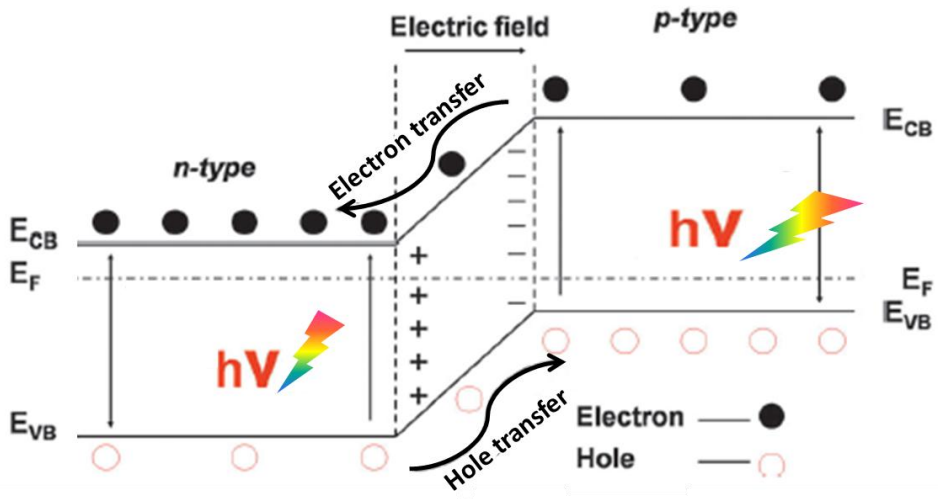

Some of these p-type semiconductors can be used as sensitizers to visible light absorption. Of particular interest is the inverse spinel cobalt ferrite ($CoFe_2O_4$), which despite has not been widely studied in PEC process [22], has been recognized by their excellent photocatalytic properties in water treatments when is coupled with TiO_2 [23]. In spite of $CoFe_2O_4$ band gap is still under debate, it has been demonstrated that $CoFe_2O_4$ can absorbs in visible light region ($\lambda < 2.2$ eV) [24,25]. Compared with other materials such as dye sensitizers and quantum dots (such as CdS, CdSe, and PbS), $CoFe_2O_4$ has receive singular attention due to its better stability, no toxicity and tunable band edge absorption, becoming it in an option to sensitize the TiO_2 [26].

1.2.5 Graphene oxide in the increment of charge carriers transport. Carbon is an extensively studied element with allotropic structures as fullerene, carbon nanotubes, graphite, diamond and graphene, which becomes it in an element of interest. Graphene structure is generally a single layer of sp2 bounded carbon atoms, and has a π configuration structure which brings excellent properties [27].

Graphene CB and VB have a cone configuration with a point of contact, also no has a band gap and is considered as a semi-metal [28]. Graphene have VB and CB which are constituted by bonding π and anti-bonding π* orbitals, respectively. When oxygen atoms are included, C-O type-bonds are created, generating a separation of π and π* orbitals resulting in a band gap in GO. Increasing the oxygenation grade, the VB maximum changes from the π orbital of graphene to the 2p orbital of oxygen, while the π* orbital remains as CB maximum [27]. A characteristic of graphene sheets is the hydrophobicity therefore is unsuitable for PEC process in water. On the contrary, graphene oxide (GO) sheets have tunable properties and is characterized by the functionalization with carboxylic acid, hydroxyl, and epoxide groups which confers it a hydrophilic character [27]. Also, have been receiving attention due to the improvement of PEC properties when is coupled with semiconductor oxides as TNT and the improvement of photocatalytic activity under visible-light where is combined with $CoFe_2O_4$ [29,30].

2. HYPOTHESIS AND OBJECTIVES

2.1 HYPOTHESIS

The photoelectrocatalytic oxidation of glycerol is enhanced by titanium dioxide nanotubes modified with $CoFe_2O_4$-GO in regard to titanium dioxide nanotubes.

2.2. GENERAL OBJECTIVE

To enhance the PEC performance of glycerol with visible light through the synergetic effect of TiO_2 nanotubes modification with $CoFe_2O_4$ and GO.

2.3 SPECIFIC OBJECTIVES

- ✓ To diminish the TNT photoactivation energy towards visible light absorption by modification with $CoFe_2O_4$.

- ✓ To increase the photocurrent response of TNT photoanode by coupling of $CoFe_2O_4$ with GO.

- ✓ To enhance the TNT photoelectrocatalytic performance under visible light illumination.

3. EXPERIMENTAL METHODOLOGY

3.1 SYNTHESIS OF PHOTOANODES

3.1.1 TNT photoanode synthesis. TNT were prepared by electrochemical anodization using titanium foils (99.5 % purity, Alfa Aesar) of 2 cm x 2 cm and thickness of 0.25 nm. The titanium foils were polished with SiC emery papers No. 400, 600, 1500 and cleaned with acetone (≥ 99.9 %), ethanol (≥ 99.5 %), and deionized (DI) water in an ultrasonic bath (Elmasonic E30H). Electrolyte was composed of 1 wt% of ammonium fluoride (≥ 98 %), 90 mL of ethylene glycol (≥ 99.8 %) and 10 mL of DI water. The electrochemical anodization was carried out in a two electrode-cell, composed of the titanium foil as anode and a platinum wire as cathode. A potential of 31 V was applied for 2 hours at 26°C. Then, the samples were rinsed with DI water and heat treated in air at 450°C at 1°C/min during 1 hour in a chamber furnace Carbolite CWF 1200.

3.1.2. TNT modification. The preparation of F photoanode was based on the procedure reported by Lei et al. [22]. Firstly, an aqueous dissolution of 5 mmol $FeCl_3.6H_2O$ (97 % of puritiy) and 2.5 mmol $CoCl_2.6H_2O$ (98 % of purity) was mixed under constant stirring at room temperature. Secondly, 1 mL $CH_3COCH_2COCH_3$ (≥ 99 %) and 45 mmol NH_2CONH_2 (≥ 99.5 %) were added to aforementioned solution. This mixture was introduced in a sealed Teflon recipient and heating in a furnace at 180°C for 12 hours in air. Finally, the films were washed with CH3CH2OH (≤ 0.005% water) and dried at 60°C for 6 h. On other hand, G photoanode was obtained by immersing TNT photoanode in a dispersion of 0.03 mg/mL of GO in DI water. Then a heating in a Teflon sealed recipient at 180°C for 12 hours was carried out. The GO used in the fabrication of G photoanodes was synthesized according to modification of Hummers method reported by Gómez et al. [31]. In the case of FG photoanode, it was obtained adding 5 mmol $FeCl_3.6H_2O$ (97 %) and 2.5 mmol $CoCl_2.6H_2O$ (98 %) to a GO dispersion of 0.03 mg/mL. The next synthesis

steps follow the identical preparation conditions of F photoanode. Finally, A-FG photoanode was obtained following the same synthesis steps of FG photoanode but using an autoclave instead of a Teflon recipient. The TNT photoanodes were immersed in the solution containing iron-cobalt salts and a GO dispersion of 0.08 mg/mL. Heating, washing and drying stages were identical to FG photoanode preparation.

3.2 CHARACTERIZATION OF PHOTOANODES

Morphology of photoanodes was observed in a field emission scanning electron microscopy (FESEM) using a JOEL Quanta 650 FEG. Elemental composition was acquired with an EDAX Apollo X energy dispersive X-ray spectroscopy (EDS). Superficial layer of F photoanode (named “F powder”) was obtained by rubbing the surface of electrode with a spatula, its morphology was obtained using a Tescan MIRA 3 FEG-SEM. The interplanar distance in F powder was obtained by using a high resolution transmission electron microscope Tecnai F20 Super Twin TMP equipment, with a field emission source, resolution of 0.1 nm in 200 Kv, maximum magnification in TEM 1.0 MX and GATAN camera US 1000XP-P. HRTEM images were analyzed using the Digital Micrograph software. The structural characterization of photoanodes was obtained by using conventional X-ray diffraction (XRD, radiation CuKα1) with a Bruker model D8 DISCOVER X-ray diffractometer with DaVinci geometry using a voltage of 40kV, 30 mA, divergent slit of 0.6mm, primary soller slit of 2.5°, sampling of 0.01526°, a nickel filter and a linear detector LynxEye. The phases were compared with the International Centre for Diffraction Data (ICDD) PDF–2 database. Raman spectra of GO, F, FG, DC-T and DC-TG photoanodes were obtained with a Horiba Lab Ram HR, by using a laser of 532 nm (~2.33 eV) with power of 1 mW. G and TNT photoanodes were measured with a laser of 473 nm (~2.62 eV). The correction of baseline by fluorescence was applied in the obtained by modified hydrothermal method. The chemical composition of photoanodes was analyzed by X-ray photoelectron

spectroscopy using a SPECS PHOIBOS150 spectrometer with a hemispheric analyzer operating X-ray energy of 1486.6 eV from Al Kα radiation. A polychromatic X-rays and a monochromator mirror with energy step of 0.025 eV was used. The polychromatic X-ray source used (Al−Kα) of the Ag $3d_{5/2}$ having FWHM = 0.8 eV while the FWHM of the monochromator mirror is 0.5 eV. The peak fitting of the high resolution measurement (by integrating the Ti, N, C, F, Fe, Co and O peaks) was determined with CASA-XPS software using a Tougaard-type background. The binding energy of each element in the sample was calibrated with the typical C 1s energy at 284.6 eV. Diffuse reflectance spectra of photoanodes were recorded with a Shimadzu PC 2401 UV-Vis spectrophotometer using an integrating sphere in the wavelength range 200 to 900 nm.

3.3 PHOTOELECTROCHEMICAL CHARACTERIZATION OF PHOTOANODES

Open circuit potential measurements, linear sweep voltammetry and photocurrent transients for all photoanodes were obtained in a potentiostat AUTOLAB PGSTAT 302N at room temperature in a three-electrode cell. An electrode of Ag/AgCl/ 3 M KCl introduced in a Luggin capillary was use as reference electrode, a graphite rod (99.99% pure, Alfa Aesar) as counter electrode and each photoanode was used as working electrode (geometrical area 2.4 cm^2). The solution was a buffer of 0.1 M K_2HPO_4 and KH_2PO_4 at pH 6.8, with or without 1mM glycerol. All the solutions were bubbled with nitrogen for 15 min to remove the dissolved oxygen. The illumination source was supplied by LEDs of 655, 627 and 617 nm and an intensity of 7 mA (1.74 W). The light illumination was chopped every 20 s in LSV measurements and 10 s in photocurrent transients. The potential applied in photocurrent transients was 0.8 V vs Ag/AgCl 3 M KCl and the scan rate was 0.01 V/s.

3.3.1 Flat band potential determination using F photoelectrode. Flat band potential value of both cobalt ferrite (F powder) and TNT was obtained by OCP

measurements. OCP and onset photocurrent measurements were performed with a lamp Philips MHN-TD 150 W metal halide with UV-block. Capacitance measurements and Mott-Schottky analysis were obtained from 0.1 to 10000 Hz, with signal amplitude of 10 mV.

3.4 PEC GLYCEROL OXIDATION ON PHOTOANODES

Photoelectrocatalytic activity was evaluated in a three-electrode cell with a potentiostat AUTOLAB PGSTAT 302N. The source of visible light irradiation was a Philips MHN-TD35 lamp with UV block. A bias potential of 0.8 V vs Ag/AgCl was applied for 1 hour. Two different solutions were used: 1) a solution of 1 M glycerol (85%) and 2) a solution of 1 M of crude glycerol (Annex A), both in 0.1 M K_2HPO_4 + KH_2PO_4 at pH 6.8 [32,33]. Glycerol concentration was monitored for 60 minutes, each 30 minutes, in an Agilent 6890 Series GC System G1540A gas chromatograph (GC) using Chemistation software. A HP Innowax Polyethylene glycol column (30 m x 320 µm x 0.25 µm) was employed during the measurements. An organic extraction of glycerol from solution was carried out using 0.5 mL of C_7H_8O (benzyl alcohol, 99 %) before injecting samples. The methodological steps include the following: 1) estimation of peak corresponding to benzyl alcohol by measuring the solvent, 2) estimation of peak corresponding to glycerol by measuring a 2.8 M glycerol solution and 3) confirmation of glycerol peak by measuring the initial 1 M solution at time 0. The intermediaries obtained in PEC glycerol oxidation were determined from gas chromatography with electron ionization, and full scan mass spectrometry (GC-MS, 70 eV; full scan).

4. RESULTS AND DISCUSSION

4.1 MODIFIED HYDROTHERMAL SYNTHESIS

4.1.1 Morphological, structural and optical characterization of photoanodes. FESEM image in Fig. 5a shows the morphology of TNT obtained by Ti anodization, the height of TNT was 2 µm. The averages of the inner and outer diameter of nanotubes were 112 nm and 87 nm, respectively, and a wall thickness ~25 nm. Nanotubes were densely connected without appreciable separation to one another. Ti and O atomic percent by EDS was in good agreement with a molar ratio of 1:2 in concordance with TiO_2. Top tubes vary in height (Fig. 5a',a''), thereby TNT arrays have a rough surface which increases the surface area of TNT. Fig. 5b-e shows FESEM images of G, F, FG and A-FG photoanodes. In the case of TNT coated with GO sheets (Fig. 5b',b'') a smoother texture than in TNT arrays is observed, which visibly diminishes the surface roughness in comparison with bare surface. EDS analysis showed a molar ratio 1:2 Ti:O, while the concentration of carbon increasing 6 times. This result indicates that carbon was incorporated in the material. On the other hand, FESEM images for F are given in Fig. 5c-c''. It can be seen that the film was coarse and cracked, with a thickness of ~4.7 µm. The magnified FESEM image displayed platelet-like morphology, which is typical of iron oxides [34]. Indeed, atomic percent in F was 52.17 % O, 16.29 % Fe, 11.13 % Ti, 5.8 % Co, 9.2 % C, 4.5 % N and 0.87 % Cl. It has been reported in the literature that chloride salts used for synthesis of solids promotes chloride trapping into the lattice or adsorption on the surface [35]. Besides, C and N could be incorporated into the film by the addition of urea modifier. On the FG surface (Fig. 5d,d'), it can be observed grains and aggregates with size less than 1 and 4 µm, respectively. EDS atomic composition for FG was 45.27 % O, 49.46 % Ti, 0.32 % Fe, 0.2 % Co, 4.3 % C and 0.45 % Cl. A slightly increase in nanotube wall thickness ~4 nm was observed for FG photoanode (Fig. 5a'',d''), showing that TNT arrays were modified.

Thus, GO avoid the formation of a thick layer and disperse the iron- and cobalt-bearing solid on the top of surface of TNT arrays.

Figure 5. FESEM images of (a) cross-section view of the bottom of the TNT arrays and (a',a'') top-view. FESEM images of (b,b',b'') G, (c,c',c'') F, (d,d',d'') FG and (e,e',e'') A-FG photoanodes.

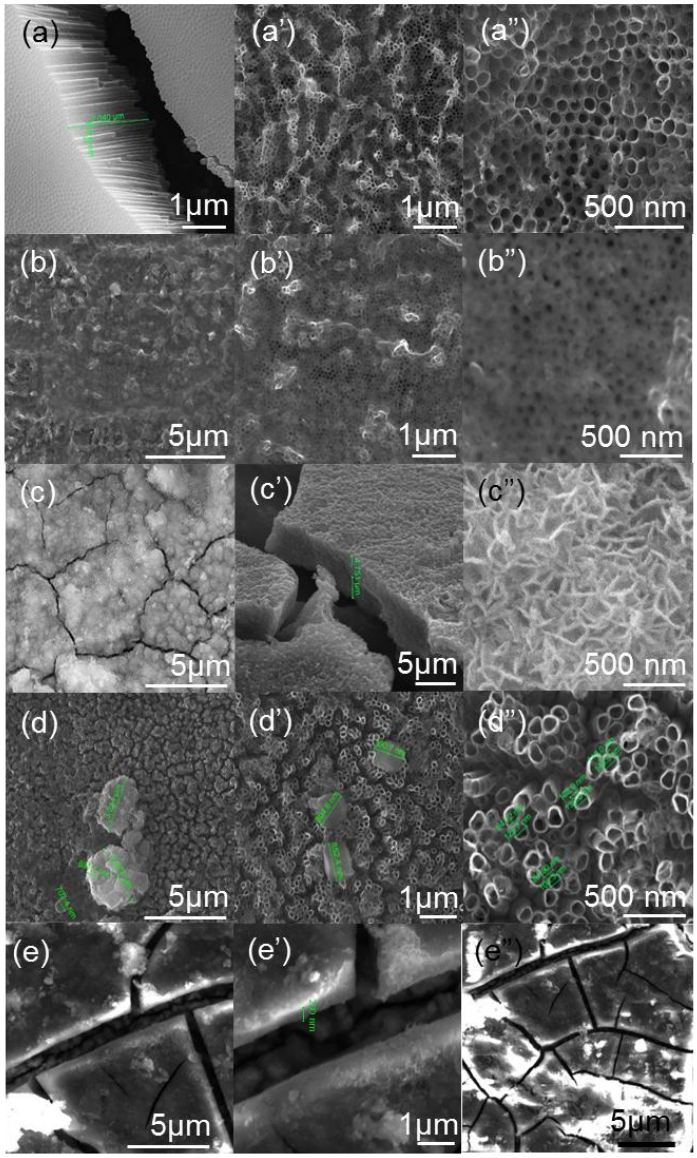

In addition, nanotubes were separated and a less dense nanotube network was obtained. A-FG photoelectrode showed a crack surface (Fig. 5e-e'') where the film covering the nanotubes had an average thickness of ~ 230 nm (Fig. 5e'). Fig. 6 shows FESEM images of F powder obtained from F photoanode. Typical cubic-like grains of ferrite with an average side length of 3.46 µm was measured [36–38]. Cubic grains appear as agglomerates segregated in FG (Fig. 5d-d').

Figure 6. FESEM images of F powder.

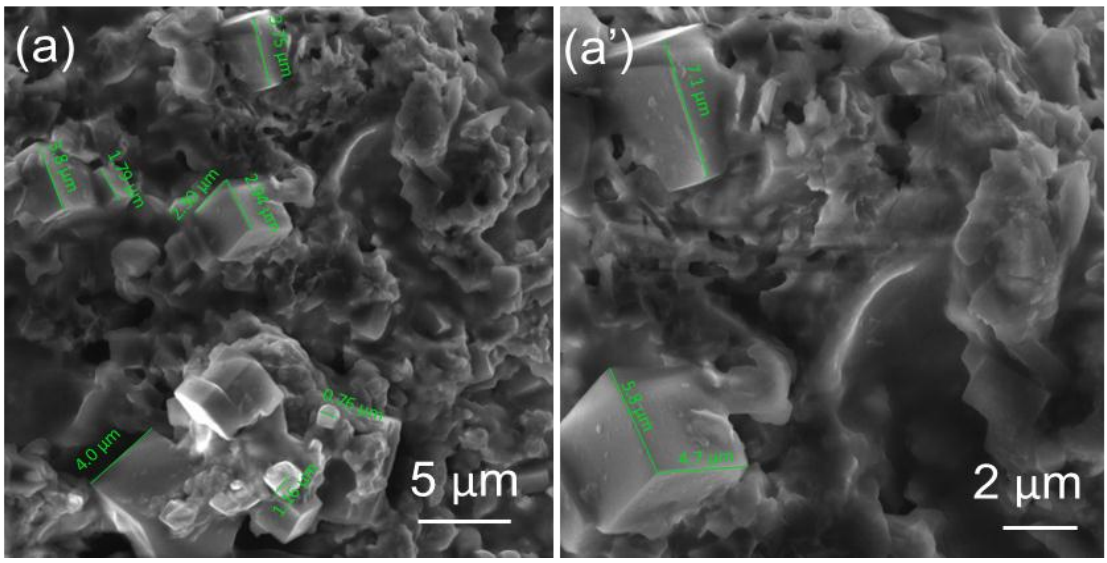

The crystallographic structure of TNT, F and FG photoanodes was studied by XRD (Fig. 7). Fig. 7a shows the XRD profile of TNT photoanode, in which the peaks at 2θ 25.38°, 37.22°, 48.12°, 54.11° and 55.14° correspond to anatase phase (PDF-2 000-89-4921) [39]. The strong peak at 25.38° indicates that TiO_2 nanotubes are oriented along the (101) plane. This preferential orientation is useful to improve the charge transport through nanotubes [40]. Diffraction peaks at 18.45°, 30.29°, 35.60° and 57.18° corresponding to (111), (220), (311) and (511) planes were assigned to cubic spinel structure $CoFe_2O_4$ in F photoanode (Fig. 7b) [41]. A broad and weak peak at 43.31° (400) indicates the presence of magnetite (Fe_3O_4) or maghemite (γ-Fe_2O_3) cubic phases [42]. The peak centered at 35.60°

(enlargement of Fig. 7) shows a better adjustment with the cobalt ferrite diffraction line, because it is in major amount. On the contrary, in FG photoanode (Fig. 7c), $CoFe_2O_4$ was undetectable. This is probably due to the differences of amount of material deposited on TNT surface. In order to identify the iron-bearing oxides in FG photoanode, a characterization by Raman spectroscopy and XPS was performed.

Figure 7. X-ray diffraction profiles of (a) TNT (b) F and (c) FG photoanodes. Diffraction lines of cobalt ferrite (continuous line; PDF-2 000-03-0864), magnetite (mn, dashed line; PDF-2 000-75-0449) and maghemite (mg, dotted line; PDF-2 000-39-1346) phases. Asterisks (*) and "a" lower letter indicate peaks from titanium substrate and anatase phase, respectively.

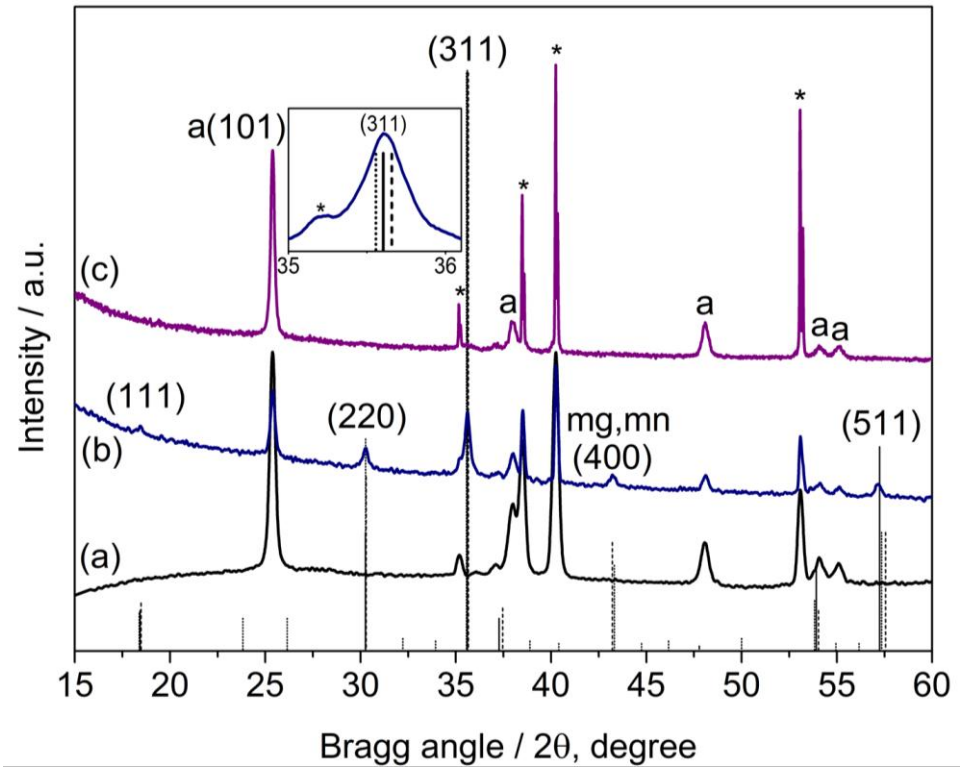

Fig. 8 shows Raman spectra of GO and TNT based photoanodes, besides $CoFe_2O_4$, Fe_3O_4 and γ-Fe_2O_3 spectra from literature are presented with

comparative purposes [43]. TNT based photoanode spectra shown bands at (144, 197, 394, 516 and 634) cm^{-1} assigned to E_g, E_g, B_{1g}, A_{1g} and B_{1g} vibrations of anatase phase (Fig. 8a) [44]. Anatase bands do not appear in F photoanode due to the large thickness of F layer. GO spectrum (Fig. 8b) shows the characteristics D and G bands at 1349 cm^{-1} and 1601 cm^{-1}, respectively. The D band (A_{1g} mode) is related to sp^3 hybridization by defects in the hexagonal structure of graphitic layer, while G band (E_g mode) is characteristic of sp^2 carbon hybridization [45]. Both G and FG photoanodes showed vibrations corresponding to GO (Fig. 8c,e). However, G band in FG showed a red shift from 1601 cm^{-1} to 1552 cm^{-1}, which is attributed to the inclusion of N containing chemical groups into the structure of GO coming from urea [46].

Figure 8. Raman spectra of TNT (a), GO (b), G (c), F (d) and FG (e). $CoFe_2O_4$ (f), γ-Fe_2O_3 (g) and Fe_3O_4 (h) spectra from literature [43] are comparatively presented. Asterisks (*) indicate peaks from anatase phase.

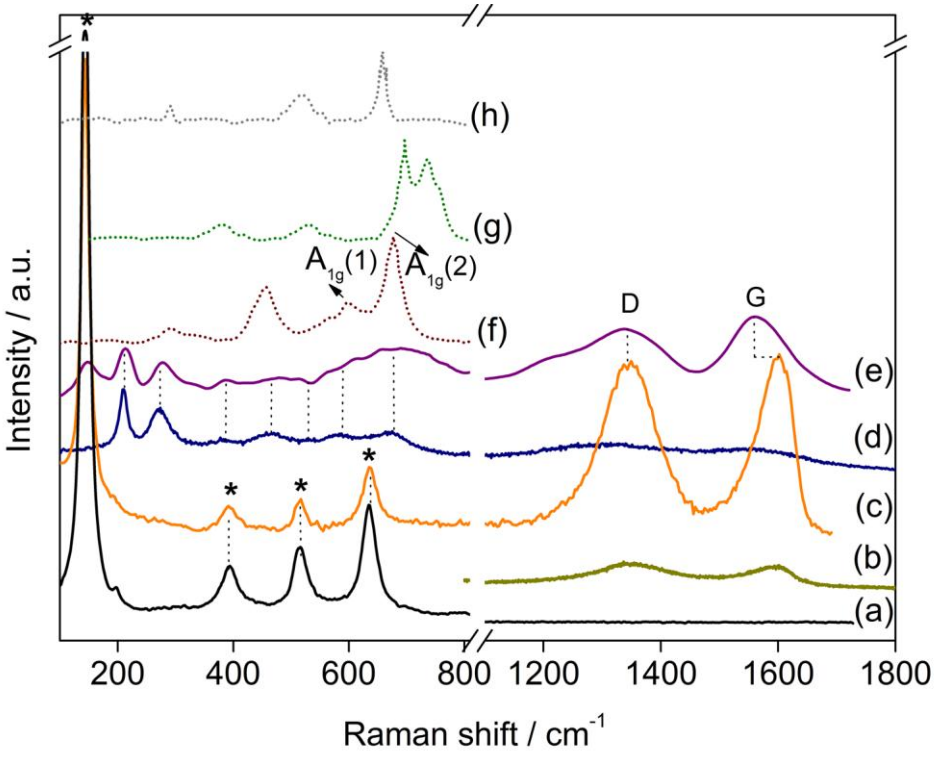

Raman spectra of both F and FG photoanodes (Fig. 8d,e) shown bands at (212, 277, 466) cm^{-1}, which are typical of Fe-O and Co-O vibrations in octahedral sites of $CoFe_2O_4$ [47]. In addition, bands at 586 and 675 cm^{-1} correspond to a splitting of the A_{1g} mode, which is ascribed to vibrations in tetrahedral sites including Co-O vibration [48–50]. In addition, bands at 516 cm^{-1} and 388 cm^{-1} are unequivocally associated to Fe_3O_4 and γ-Fe_2O_3, respectively [51,52].

In order to determinate the elemental composition and modification of the TNT based photoanodes, a XPS analysis was performed (Fig. 9-10 and Table 1). Annexes B and C shown general spectra of TNT, G, F, and FG photoanodes. C, N, K, Ti, F and O were observed in all these photoanodes. Peaks corresponding to K $2p_{3/2}$ (292.0 eV) and K 2s (376.7 eV) are attributed to phosphate buffer adsorbed on photoanode surface. Fe and Co were only detected in F and FG. High resolution C 1s spectrum of TNT and its deconvolution are given in Annex B. Six peaks centered at 282.7, 283.3, 284.6, 285.2, 286.3 and 288.4 eV are in good agreement with substitutional and interstitial C dopant (O-Ti-C and Ti-O-C), which possibly occurred during the anodization process as has been recently reported [53], and by other hand C-C, C-O-H, C-O C=O groups from adventitious contamination, respectively [53,54]. In the case of G photoanode, Ti-O-C peak centered at 283.4 eV confirms C-doping of TNT (Fig. 9). Only in G photoanode was observed the characteristic peak of C=C (284.1 eV) associated to GO. However, O=C-O contribution (288.9 eV) also characteristic of GO was observed in G and FG photoanodes. Additionally, for FG photoanode a peak at 287.0 eV reveals the existence of nitrogen functional groups [55,56].

High-resolution N 1s spectrum showed substitutional doping of nitrogen into TiO_2 lattice, it is well-known that NH_4F modify TNT during anodization process [53,57]. Fig. 9 reveals that an additional modification with N was observed in F and FG. Interstitial N doping was identified at 396.7 eV [58], it is attributed to the presence

of urea during cobalt ferrite synthesis. In FG photoanode additional contributions of nitrogen at binding energies of 398.1, 399.7, 402.2 and 404.1 eV were observed.

Figure 9. XPS high resolution spectra of C 1s, N 1s and Ti 2p of the G, F and FG photoanodes, as indicated in the figure legends.

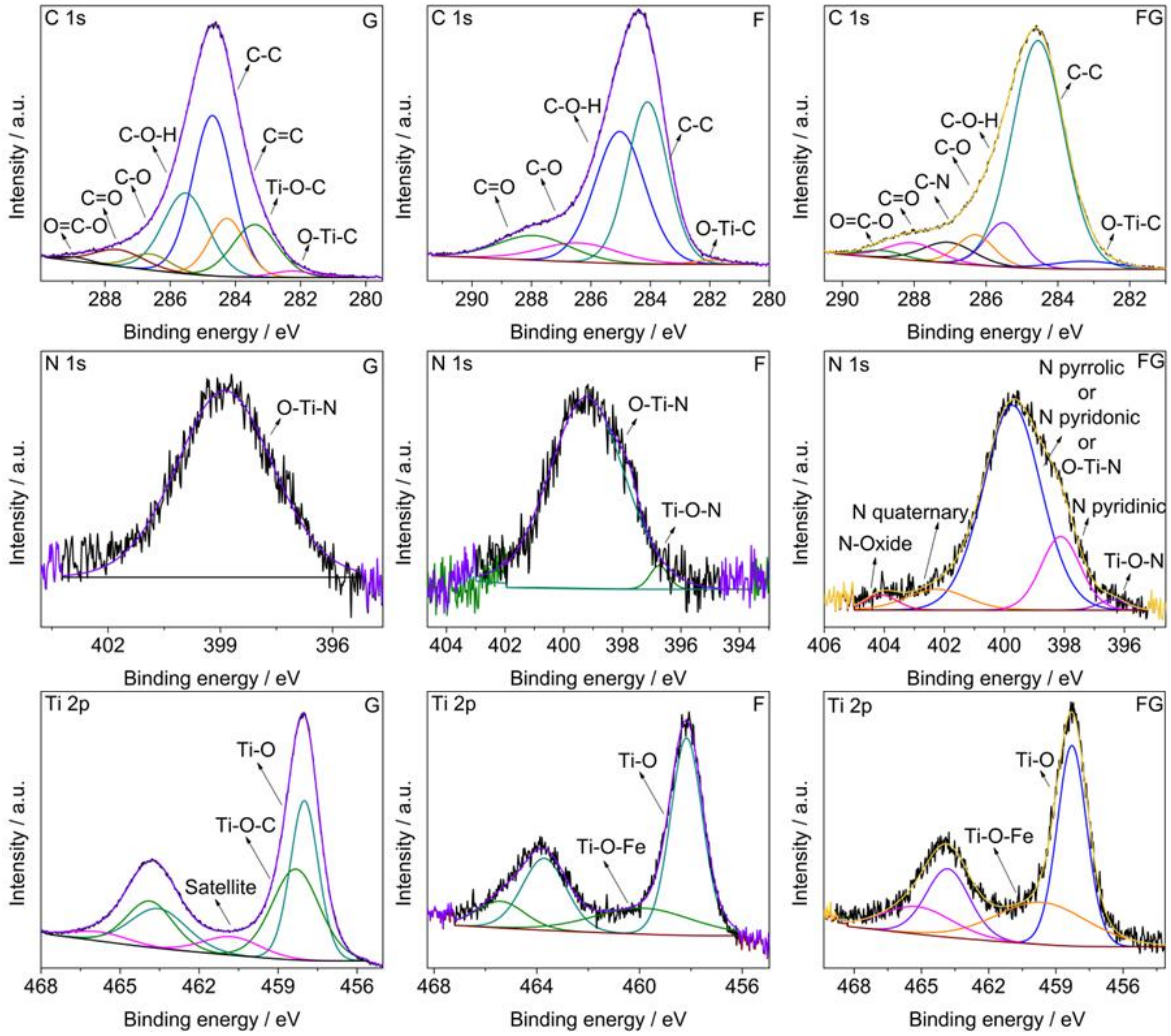

These peaks correspond to a pyridinic (C-N=C), pyrrolic or pyridonic (C-NH-C or N=C-O-H), quaternary nitrogen and N bonded to oxygen, respectively [46,59,60]. The peak at 399.7 eV could be overlap with the corresponding to O-Ti-N bonds. These results confirm the structural modification of GO by urea in accordance with

Raman analysis. Fig. 9 shows the high-resolution Ti 2p spectrum, where the typical peak of Ti-O bonds was identified at 458.0 eV for all photoanodes [61]. In addition, TNT and G photoanodes showed the contribution of Ti-O-C bonds at 458.8 [62]. On the other hand, an additional contribution for F and FG photoanodes reveals the isomorphic substitution of titanium by iron (Ti-O-Fe) associated to the signal centered at 459.8 eV [61,63]. Fluorine in substitutional positions was observed at 684 eV in all photoanodes (not shown) [64].

Fig. 10 shows Fe 2p and Co 2p spectra of both F and FG photoanodes. The peak at 709.9 confirms the presence of Fe_3O_4, while the peak at 710.9 eV could be attributed to either γ-Fe_2O_3 or $CoFe_2O_4$ in octahedral sites [61,65–67]. Indeed, the peak at 712.6 eV shows the presence of Fe^{3+} in tetrahedral sites corresponding to $CoFe_2O_4$ [68]. The peak observed at 710.9 eV associate to Ti-O-Fe bonds [61] confirms the Fe-doping in TNT. Satellite peaks of Fe appear at 715 and 718.3 eV [69]. High-resolution Co 2p spectra showed contributions of $CoFe_2O_4$ at 780.5 eV and 784.6 eV ascribed to the presence of Co^{2+} in octahedral and tetrahedral sites, respectively [68,70]. This shows that exists a certain inversion degree of the spinel structure. A satellite peak of Co appears at 789.9 eV [68]. High-resolution O 1s spectra at 527.8 has been attributed in the literature [71], to interaction of TiO_2 and Fe_3O_4 in composites oxides; whereas the peak at 529.4 eV is associated to Fe-O bonds. The peak at 530.0 eV corresponds to Ti-O bond in TiO_2 [72]. The peak at 530.7 eV could be attributed to either γ-Fe_2O_3 or Fe_3O_4 [65]. The peak at 531.5 eV matches with oxygen from $CoFe_2O_4$ [68]. In the case of G and FG photoanodes, the peak at 535.4 eV corresponds to O=C-O-H bonds from GO [73]. It is noteworthy that only a peak at 530.9 eV in TNT photoanode exhibited the presence of hydroxyl groups on its surface.

Figure 10. XPS high resolution spectra of Fe 2p, Co 2p and O 1s of the F and FG photoanodes

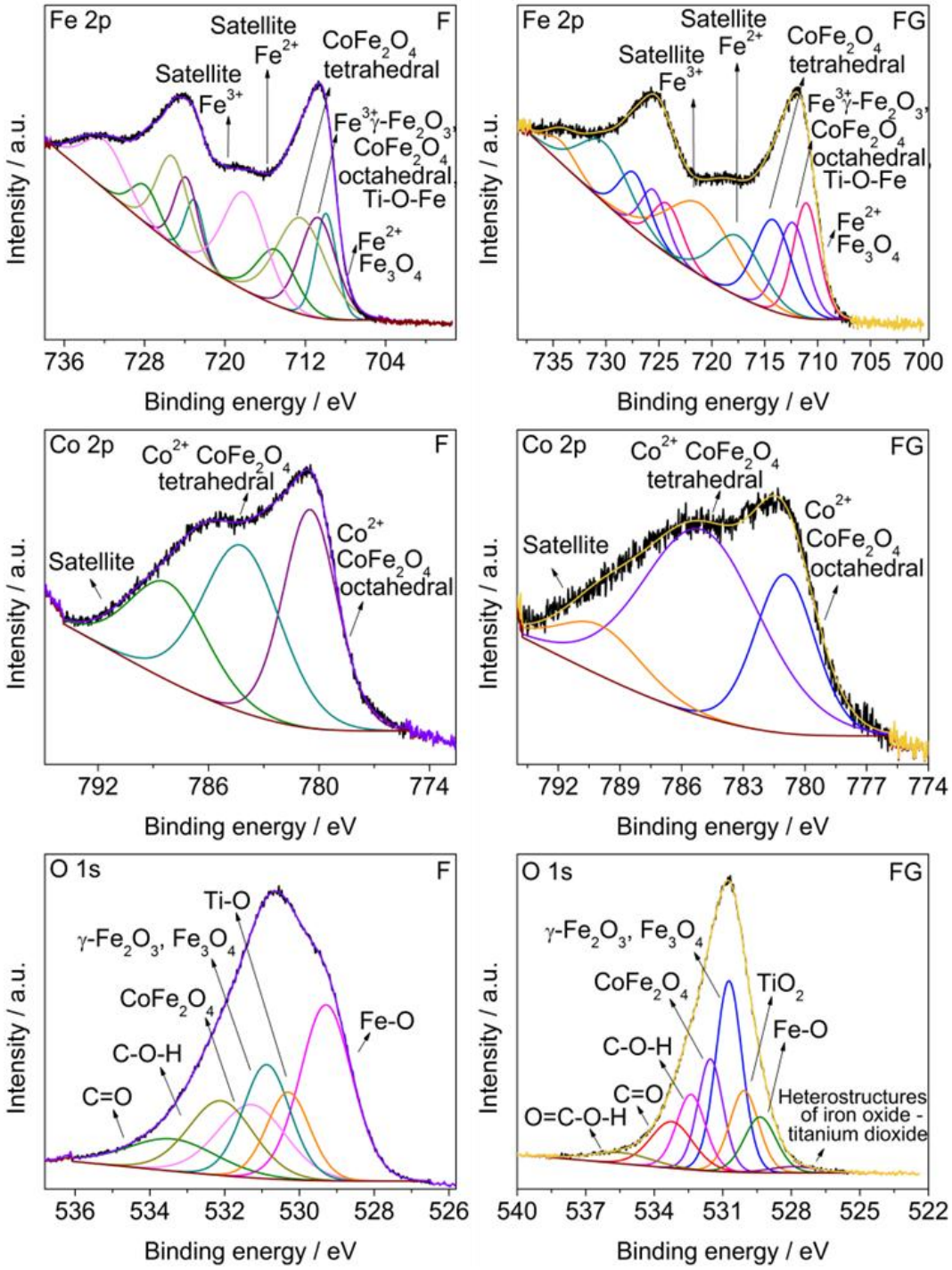

Table 1. XPS single chemical components of TNT, G, F and FG photoanodes.

		TNT	G	F	FG	Ref.
Element	**Bonds**	**Binding energy (eV)**				
Carbon	O-Ti-C	282.7	282.3	282.1	283.1	[53,54]
	Ti-O-C	283.3	283.4			[53,74,75]
	C=C		284.1			[53,74,75]
	C-C	284.6	284.6	284.6	284.6	[53,54]
	C-O-H	285.2	285.5	285.2	285.5	[53,54]
	C-O	286.3	286.6	286.4	286.2	[53,54]
	C-N				287.0	[55,56]
	C=O	288.4	287.5	288.1	288.1	[53,54]
	O=C-O		288.9		288.9	[53,74,75]
Nitrogen	Ti-O-N (Interstitial)			396.7	396.3	[58]
	C-N=C (Pyridinic)				398.1	[46]
	O-Ti-N (substitutional)					[53,57]
	or C-NH-C (pyrrolic)	399.6	399.3	399.2	399.7	[46]
	or N=C-O-H (pyridonic)					[46]
	Quaternary nitrogen				402.2	[59]
	N-oxide				404.1	[60]
Titanium ($2p_{3/2}$)	Ti-O-Ti	458.0	458	458.1	458.2	[76]
	Ti-O-C (interstitial)	458.8	458.4			[62,77]
	Ti-O-Fe			459.8	459.6	[61,63]
Fluorine	O-Ti-F	684.0	683.9	684.0	683.9	[64]
Iron ($2p_{3/2}$)	Fe^{2+} Fe_3O_4			709.9	709.4	[61,65–67]
	Ti-O-Fe					[61]
	or Fe^{3+} γ-Fe_2O_3			710.9	710.7	[61,65–67]
	or Fe^{3+} $CoFe_2O_4$ octahedral					[68]
	Fe^{3+} tetrahedral $CoFe_2O_4$			712.6	712.2	[68]
Cobalt	Co^{2+} octahedral $CoFe_2O_4$			780.5	780.9	[68,70]
	Co^{2+} tetrahedral $CoFe_2O_4$			784.6	785.0	[68,70]

Oxygen	Interaction Fe_3O_4 with TiO_2				527.8	[71]
	Fe-O			529.3	529.4	[71]
	Ti-O	529.9	529.8	530.2	530.0	[76] [72]
	γ-Fe_2O_3 or Fe_3O_4			530.8	530.7	[65]
	OH	530.9				[78]
	$CoFe_2O_4$			531.3	531.5	[68]
	C-O-H	532.3	532.0	532.1	532.3	[79]
	C=O		534.2	533.4	533.2	[73]
	O=C-O-H		535.8		535.4	[73]

Fig. 11 shows HRTEM image of F powder, which is formed by nanoparticles less than 25 nm in size. The lattice fringes showed a d-space of about 0.171 nm corresponding to the (422) plane of $CoFe_2O_4$.

Figure 11. High-resolution transmission electron microscopy images of F powder.

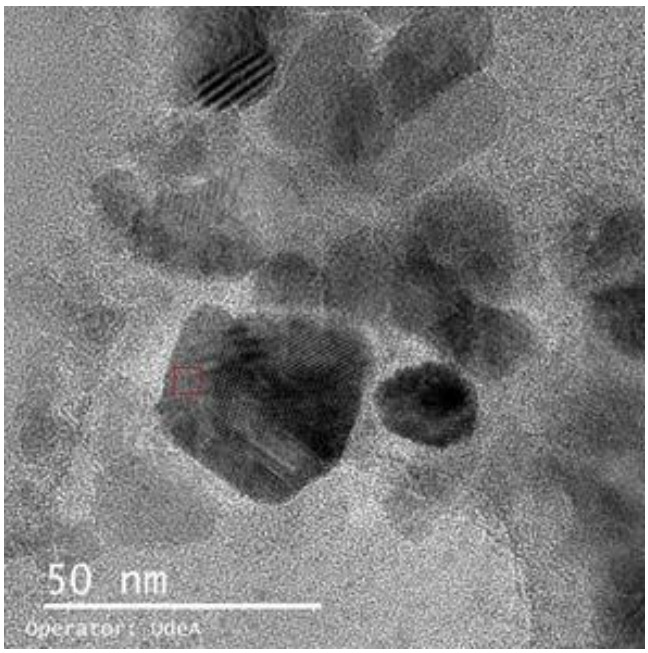

The HRTEM-EDX analysis showed a Co/Fe atom ratio of 1:2, which is in fair agreement with the stoichiometry of $CoFe_2O_4$. The lattice constant a was

calculated from Miller indices (h k l) using the relation $a = d_{h,k,l}\sqrt{h^2 + k^2 + l^2}$, where d is the interplanar distance [80]. The a value obtained was 8.387 Å. The cation distribution in the inverse spinel structure can be characterized by the so-called degree of inversion x, which is defined as the fraction of the divalent metal in octahedral sites as follows: $(Co_{1-x}Fe_x)_{tet}[Co_xFe_{2-x}]_{oct}O_4$. From the lattice constant herein obtained, the inversion degree is in the range of 0.75 < x <1 [76] [81].

From above characterization is possible to propose general schemes for TNT based photoanodes (Fig. 12).

Figure 12. Schematic diagrams of a) TNT, b) G and c) FG photoanodes.

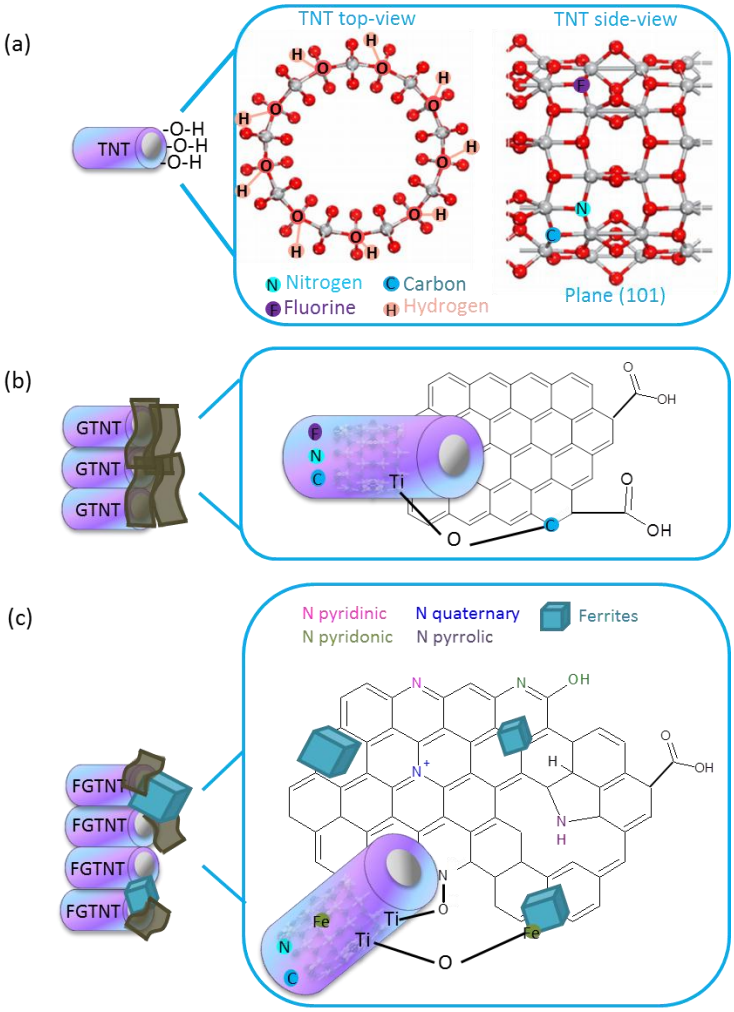

Fig. 13 shows the modified Kubelka-Munk function versus photon energy of TNT based photoanodes. TNT, F and FG showed two absorption edges, while G exhibited only one. Calculated absorption edges are given in Table 2. The principal band gap is about 3.2 eV, which is characteristic of TiO_2. In the case of TNT (Fig. 13a), the secondary absorption could be caused by the presence of sub-band gap states, because C, N and F modification promotes the generation of energetic states inside TiO_2 band gap [53]; hence, an absorption edge of 1.42 eV is observed.

Figure 13. Modified Kubelka-Munk function vs photon energy of (a) TNT, (b) G, (c) F and (d) FG photoanodes. Inset shows the close up view of absorption spectra.

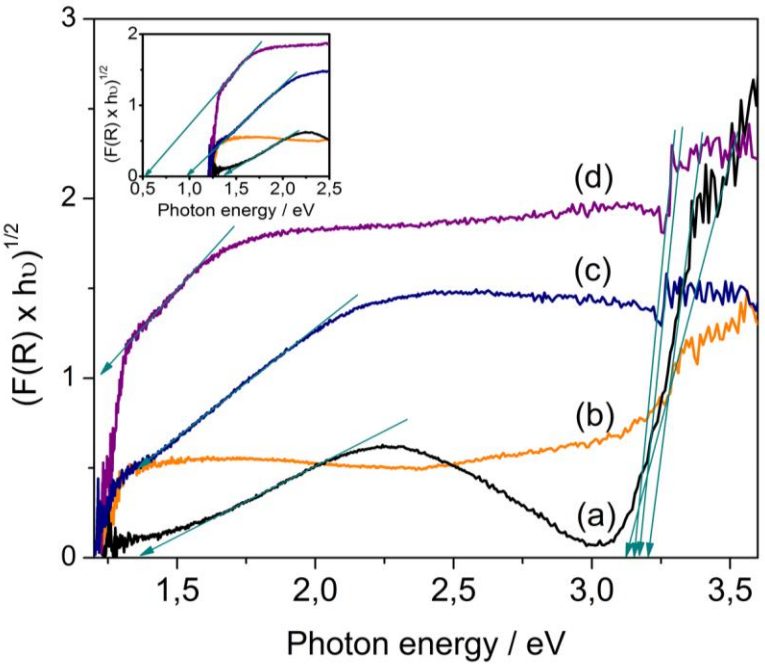

The spectrum of G photoanode shows a continuous absorption band in the visible light region (Fig. 13b), which is typical in materials containing carbon [82,83]. This has been attributed to the existence of various levels of GO sheets oxidation, in which, transitions $\pi \rightarrow \pi^*$ take place [83–86]. Both F and FG shown similar absorption features, which are distinct to the other photoanodes. Thus, the

continuous and large absorption in the visible region is ascribed to iron-bearing oxides (Fig. 13c). The absorption edges of F and FG photoanodes were 0.92 and 0.55 eV, respectively. Indeed, the band gap of cobalt ferrite, magnetite and maghemite iron-cobalt are in the range of 0.8 to 2.87 eV [87–91].

Table 2. Calculated absorption edges of TNT, G, F and FG photoanodes.

	TNT	G	F	FG
Edge 1	3.19	3.14	3.17	3.15
Edge 2	1.42	-	0.92	0.55

4.1.2 Photoelectrochemical and photochemical characterization. To evaluate photoactivity of the TNT, G, F, FG and A-FG photoanodes, measurements at zero net exchange photocurrent were carried out under illumination in absence and presence of glycerol (Fig. 14). OCP measurements were obtained under illumination of 655 nm in a 1 mM glycerol and 0.1 M buffer phosphate solution at pH 6.8. Firstly, when a semiconductor is in contact with a solution, under equilibrium Fermi level matches with redox potential electrolyte and a band bending occurs in the semiconductor. The band bending depends on the electrolyte redox potential, but in this case no redox pair was used. In the case of the buffer solution the Fermi level is not well defined and the band bending determines the magnitude of the photopotential (V_{ph}) developed [92,93]. The V_{ph} values of photoanodes are given in Table 3. For all photoanodes the shift to less positive potentials indicates a n-type behavior [93]. Also, with the exception of A-FG, higher V_{ph} values in presence of glycerol are observed. This indicates that glycerol has a scavenging effect by trapping holes photogenerated in valence band, promoting that more electrons photogenerated being accumulated in conduction band.

Figure 14. OCP measurements of TNT, G, F, FG and A-FG photoanodes in absence and presence of glycerol as indicated in the figure legends. Inset shows the close up view of A-FG. Measurement conditions: geometric area of 2.4 cm^2, 1 mM glycerol, 0.1 M KH_2PO_4 and K_2HPO_4 at pH 6.8. Light Source: LED driver 655 nm.

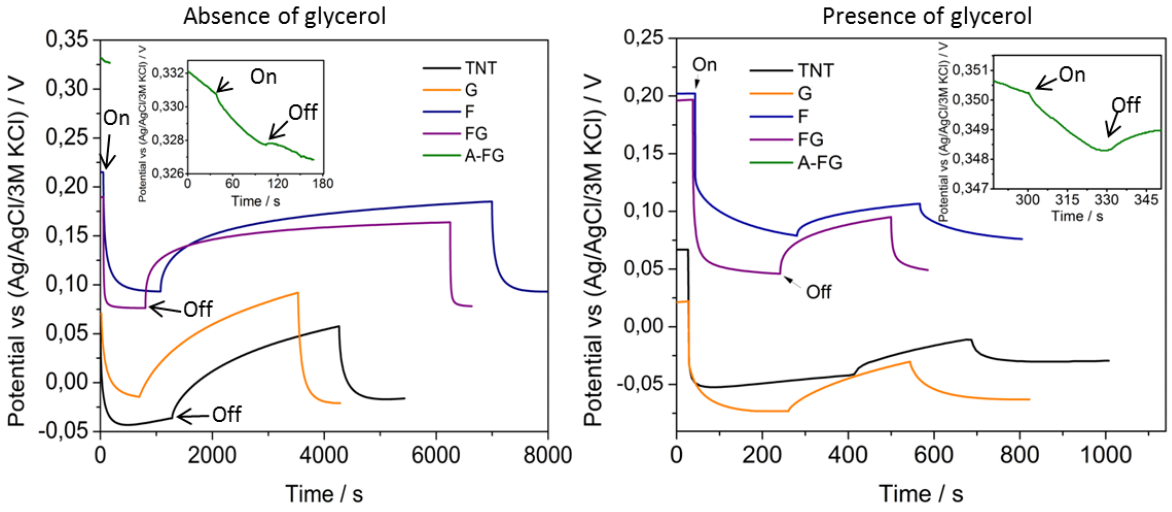

G and A-FG photoanodes exhibits lower V_{ph} values principally due to the GO avoided the passage of light efficiently. Also, A-FG is highly unstable have into account the changing potential at the time and its low mechanical stability. In the case of TNT photoanode the V_{ph} of 0.097 V indicates a photoresponse due to sub-band gap levels introduce by F, N and C doping. For F and FG, the higher V_{ph} values suggest the improvement in electron-hole separation explained by the existence of the built-in field in the heterojunction facilitates charge carriers separation [94–97].

Table 3. Photopotential generated by TNT, G, F, FG and A-FG photoanodes in absence and presence of glycerol (V vs Ag/AgCl).

	A-FG	G	TNT	F	FG
V_{ph} glycerol absence	0.003	0.085	0.097	0.122	0.129
V_{ph} glycerol presence	0.002	0.094	0.118	0.128	0.144

In Fig. 15 are shown linear sweep voltammograms (LSV) with chopped light of TNT, G, F, FG and A-FG photoanodes. A solution 0.1 M KH_2PO_4 and K_2HPO_4 at pH 6.8 was used. The potential range was from OCP to 1 V. When the potential sweep starts, an increment in photocurrent is generated due to potential applied produces an electric field which separates electrons from holes. Electrons are driven through external circuit of the cell to counterelectrode and holes promote water oxidation. When the rate in which electron-hole pairs generation is equal to the rate at which the anodic reaction occurs a current plateau is generated (saturation current). Firstly, the current was measured under illumination of 655, 627 and 617 nm to find the minimum energy of excitation (Fig. 15a). The corresponding energies were 1.89, 1.98 and 2 eV, respectively. The F photoanode was chosen for this measurement due to the exposed area to illumination only is composed by the iron and cobalt oxides. As the irradiation increases in energy the current density remains constant. This means that a radiation of 655 nm is sufficient to produce a photocurrent.

Figure 15. LSV of (a) F photoanode under illumination of 617, 627 and 655 nm and (b) TNT, G, F, FG and A-FG photoanodes with chopped light of 655 nm. Measurement conditions: active area of 2.4 cm^2, 0.1 M KH_2PO_4 and K_2HPO_4 electrolyte at pH 6.8 and scan rate 0.01 V/s.

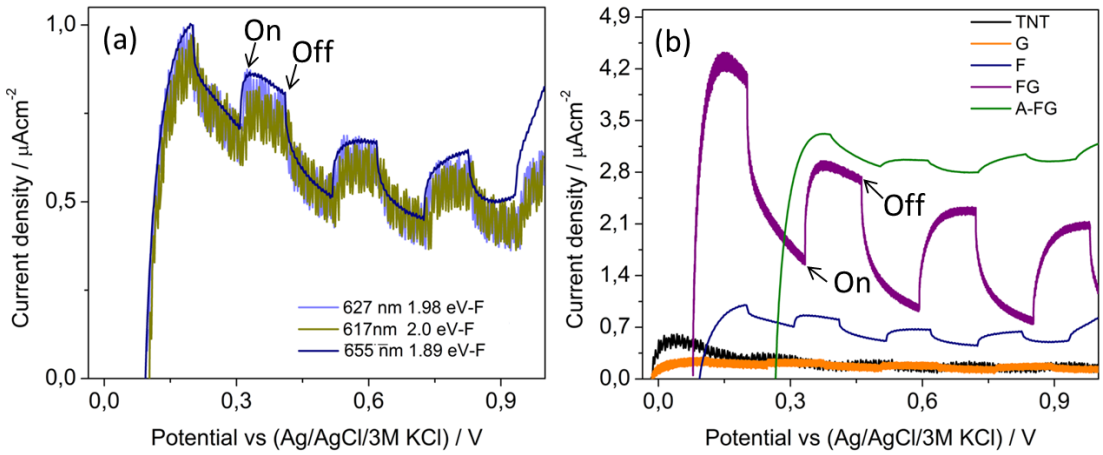

Given the above, LSV plots of TNT, G, F, FG and A-FG photoanodes under illumination of LED 655 nm were obtained (Fig. 15b). It can be observed the generation of photocurrent in all photoanodes when positive potentials are applied. In the case of FG photoanode the highest photocurrent in a first illumination cycle was obtained. However, when the illumination cycles and potential increase, the current density decreases even bellow A-FG photoanode. This shows a loss of activity given by a photodissolution process of FG photoanode [98]. For A-FG photoanode, the photocurrent density was lower than that of the first illumination cycle of FG photoanode. Based on this, two conjectures can be proposed. First, the increment in the amount of GO could incorporate carbon into TiO_2, promoting the formation of interfacial states in the GO/TiO_2 interface. These states could cause an upward band bending inhibiting the transport of electrons photogenerated and decreasing photocurrent density. Besides, the amount of GO could promote the decreasing of transmittance, which avoid the passage of light efficiently into the TiO_2 nanotubes [99]. The last could also explain the lower photocurrent density obtained by G photoanode. For F photoanode the lower photocurrent density is caused by the oxides thickness ~ 5 μm. The thickness influenced the photons absorption and the charge carriers transport. This is due to there is a long diffusion distance to transport electrons to conductor substrate [100].

On the other hand, despite the A-FG photoanode exhibits the highest photocurrent after the second illumination cycle of FG photoanode, the PEC photoresponse is expected to be limited. This is because of the difference between the current density under illumination and in dark (ΔI_o) is lower compared to the other photoanodes. The ΔI_o is taken as an indicative of the PEC photoresponse since it takes into account both illumination and darkness conditions and not only illumination. Table 4 shows a summary of the maximum and minimum current densities at 0.8 V (potential used in PEC glycerol oxidation). The ΔI_o at 0.8 V in ascending order are 0.0686, 0.1060, 0.1250, 0.1267 and 1.5684 (μA cm^{-2}) for A-FG, G, TNT, F and FG photoanodes, respectively.

The above behavior is observed in the photocurrent transients shown in Fig. 16, where the highest ΔI_o corresponds to FG photoanode. This is attributed to a synergistic effect of the heterojunction, where electrons photogenerated are effectively transferred from $CoFe_2O_4$ to TNT. Also, the GO modification with N could promote an increment of the charge carriers density improving the photoresponse [101,102].

Figure 16. Photocurrent transients at 0.8 V of TNT, G, F, FG and A-FG photoanodes. Inset is a zoom for all photoanodes. Measurement conditions: active area of 2.4 cm^2, 0.1 M KH_2PO_4 and K_2HPO_4 at pH 6.8. Light source: LED driver of 655 nm.

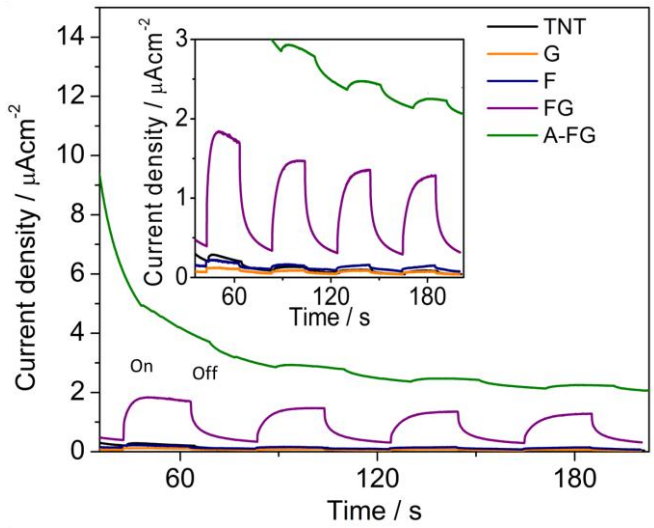

For F photoanode the lower photoresponse in comparison with FG is due to the thick layer, which promotes the recombination of charge carriers. In the case of TNT there is not contribution of heterojunction or GO. For G photoanode, despite the fact that a heterojunction was formed with the GO, this prevented the passage of light into the TNT. Finally, the lowest ΔI_o for A-FG photoanode confirms that its reuse is hardly viable due to its high instability. Also, a high contribution of dark current was observed. This can be attributed to charge accumulation behavior [103]. Have into account the above, the PEC photoresponse of photoanodes is suggested as follows: FG > F > TNT > G > A-FG.

Comparative photocurrent densities were taken at 0.8 V in presence of glycerol (Fig. 17, Table 4). In Fig. 17 can be observed that TNT and G photoanodes exhibited higher photocurrent densities in presence of glycerol (ΔI_g) that in absence of it (ΔI_0). A relation of $\Delta I_g/\Delta I_0$ of 2 was observed. This increment in photocurrent density could indicate direct oxidation of glycerol by holes photogenerated on photoanodes surface. This effect named “current doubling” has been recent studied in TiO_2 heterojunctions using glycerol as hole scavenger where glycerol radical intermediates are stabilized by liberating and injecting one electron to CB of TiO_2 [104]. Direct glycerol oxidation can be thought from the point of view of glycerol adsorption. Some previous investigation evidence the strong capacity of TiO_2 to adsorb glycerol molecules and also has revealed the direct electrons reaction with glycerol molecules [105,106].

Figure 17. LSV of TNT, G, F, FG and A-FG photoanodes with chopped light of 655 nm. Measurement conditions: active area of 2.4 cm^2, 1 mM glycerol and 0.1 M KH_2PO_4 and K_2HPO_4 electrolyte at pH 6.8 and 10 mV s^{-1}.

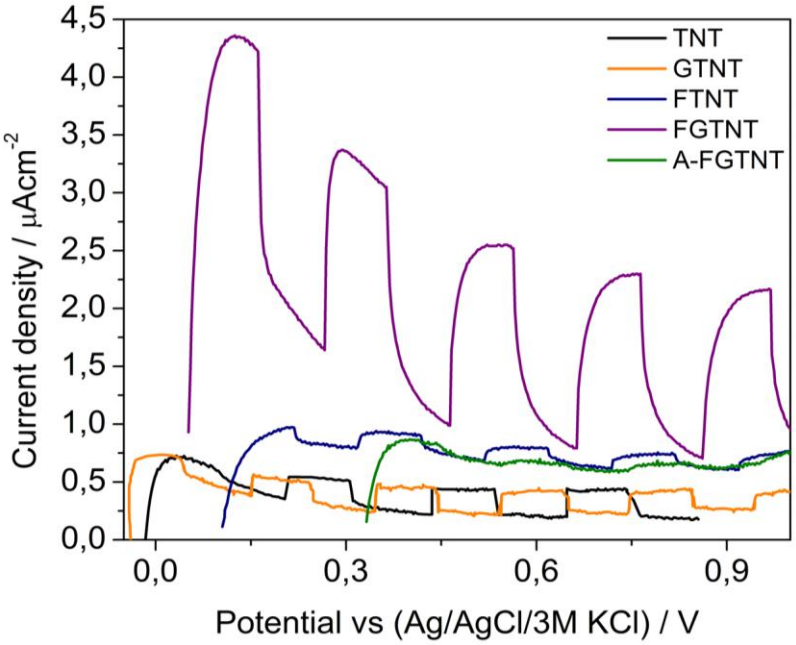

Have into account that the TiO_2 surface is hydroxylated Ti-OH, it can be suggest the adsorption of glycerol on OH terminations and subsequent reaction with holes [106]. Also, studies have shown that some Ti-OH hydroxylated surfaces present high energy stability, which are not oxidized by h^+ in valence band and therefore they participate in electronic exchange with species directly in solution [107]. On the contrary, in F and FG photoanodes the double current effect was not observed. However, the fact that current density does not increase in presence of glycerol does not necessarily mean that these are less efficient in organics degradation [108].

Table 4. Difference between photocurrent under illumination and current under dark obtained from LSV plots for TNT, G, F, FG and A-FG photoanodes in the region potential of 0.8 V in absence and presence of glycerol (μA cm^{-2}).

PHOTOANODE		A-FG	G	TNT	F	FG
Glycerol presence	Maximum photocurrent	0.6610	0.4337	0.4439	0.7520	2.3010
	Minimum current	0.5820	0.2160	0.1751	0.6030	0.7040
	Difference (ΔI_g)	0.0790	0.2177	0.2688	0.1490	1.5960
Glycerol absence	Maximum photocurrent	3.0377	0.2053	0.2222	0.6384	2.3200
	Minimum current	2.9691	0.0993	0.0972	0.5117	0.7516
	Difference (ΔI_0)	0.0686	0.1060	0.1250	0.1267	1.5684

4.1.2.1 Flat band potential determination using F photoelectrode. Flat band potential was determined by OCP, onset potential and Mott-Schottky analyses. In the case of OCP measurements, the maximum photopotential is related directly with Fermi level position of the oxide, and this position depends on semiconducting behavior of the oxide. Therefore, for F photoelectrode a p-type semiconducting

behavior showed a potential near to valence band. The maximum photopotential obtained was 0.226 V (Fig. 18a). To elucidate the electronic transport, the OCP measurements also have to carry out in TNT photoanode. For TNT photoanode, an n-type semiconducting behavior was observed, where the maximum photopotential obtained at -0.220 V can be estimated to be closer to conduction band.

In contrast, onset potential was carried out to compare the TNT flat band potential value obtained in OCP measurements (Fig. 18b). The onset potential is obtained of current-potential curves under light chopping illumination, where its value corresponds to potential region where bands are flattened, i.e. under ideal conditions the onset potential is the region where the accumulation zone changes to a depletion zone [109]. The TNT photoanode onset potential was found to be -0.210 V highly similar to that found by OCP.

On the other hand, Mott-Schottky analysis led to determine the flat band potential value from the intercept of the extrapolated straight lines involving the capacitance of the space charge layer of the semiconductor (Annex D) [110]. Also, the type of conductivity could be obtained. Fig. 18c shows the Mott-Schottky plot with a positive slope for TNT photoanode confirming the n-type behavior found by OCP measurements. The apparent flat band potential value can be estimated to be at -0.212 V, which is very close to the obtained by photocurrent onset and OCP measurements. Fig. 18d shows M-S plot for F photoelectrode, in which a line with negative slopes agrees with p-type conductivity found by OCP measurements. The estimated flat band potential value was 0.373 V which differ of the value obtained by OCP measurements. A possible reason is that M-S analysis depends principally on composition and crystallinity of sample [111]. Since F photoelectrode has a variable composition, the value obtained by OCP measurements is more closed to flat band potential value than that obtained by M-S analysis.

Figure 18. (a) OCP measurements of TNT photoanode and F photoelectrode under visible light illumination (b) Current-potential curves for the TNT photoelectrode at the scan rate of 0.01 V/s (c) and (d) Mott–Schottky plot calculated from variation of space charge capacitance with the applied potential at different frequencies of TNT photoanode and F photoelectrode, respectively. Solution: 0.1 M KH_2PO_4 and K_2HPO_4 electrolyte at pH 6.8. F photoelectrode illumination source: LED driver (λ = 655 nm). TNT photoanode illumination source: 150 W metal halide (Philips, MHN-TD) with UV-block. TNT photoelectrode active area: 2.4 cm^2.

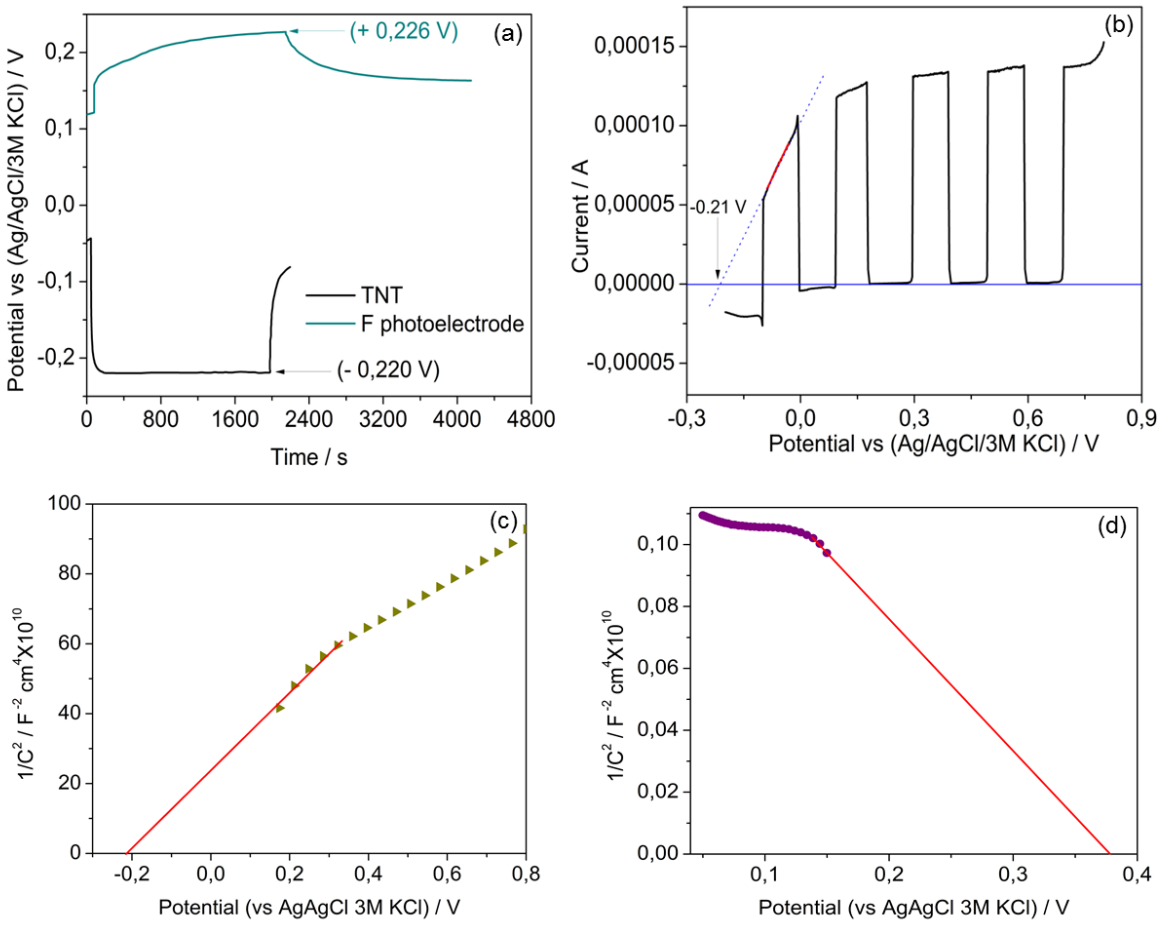

According to the morphological, structural, optical and photoelectrochemical analyses, the TNT visible light photoactivation was possible due to the codoped

with C, N and F. After sensitization, Fe was incorporated being able to improve their photoresponse to visible light illumination. In order to demonstrate that photoactivation does not only depend on C, N, F and Fe doping, the effect of iron-cobalt oxides sensitization in electron transport was evaluated. The principal factor to evaluate the electrons transport is through thermodynamic factors as conduction and valence band positions, which were obtained previously. The study separately of the TNT photoanode showed that the flat band potential value of -0.220 V can be approximate to conduction band, while the flat band potential value of 0.226 V for F photoelectrode is near to valence band. Considering the optical, morphological, structural, photochemical and photoelectrochemical analyses, it is possible stated that the sensitizer conduction band has a potential more negative than that for TNT. Thus, the transference of charge carriers photogenerated was given in an electron-hole cascade mechanism (Fig. 19), where electrons photogenerated in the oxides were transferred to TNT conduction band and holes were transferred from TNT valence band to the sensitizer valence band.

Figure 19. Schematic mechanism of electron transport and photoactivation for TNT/F heterojunction.

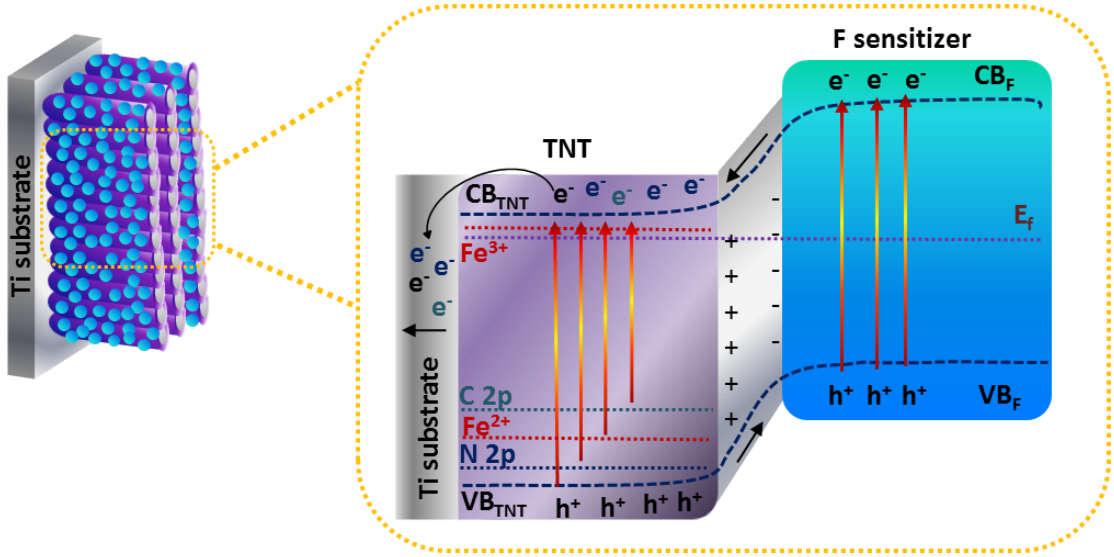

4.1.3 Photocatalytic activity of TNT based photoanodes. To evaluate the photocatalytic activity of all photoanodes, glycerol degradation was carried out. A solution of 1 M glycerol in phosphate buffer and an applied potential of 0.8 V vs Ag/AgCl was used in the evaluation. Figure 20 shows the C/C_o vs time plot, where C represents the concentration at time t and C_o at t = 0 s. For comparative purposes, pure and crude glycerol solutions were used.

Figure 20. C/C_o versus time curves of TNT, G, F and FG photoanodes obtained under visible-light irradiation for crude and pure glycerol solutions.

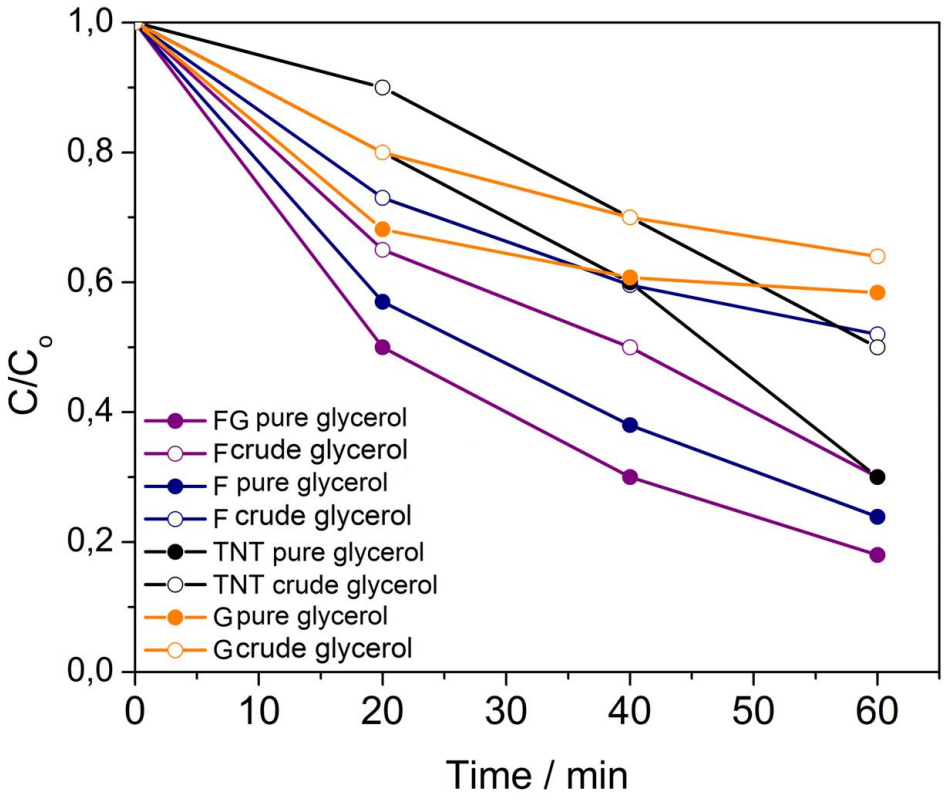

In Fig. 20, it can be observed higher percentages of glycerol oxidation for pure glycerol solutions than that for crude glycerol solution. The competitive oxidation between methanol and glycerol in crude sample explains the aforementioned performance. Photoelectrocatalytic oxidation of pure glycerol for FG, F, G and TNT

photoanodes showed percentages of about 82%, 76%, 42% and 70%; while with crude glycerol the percentages were 70%, 48%, 36% and 50%, respectively. Therefore, the photocatalytic activity of photoanodes in increasing order was: G < TNT < F < FG. Thereby, F and FG photoanodes exhibited greater activities in glycerol oxidation. In order to determine the type of photoelectrocatalytic reaction mechanism that occurs in FG photoanode, the intermediaries of glycerol oxidation were identified (ANNEX E and F). In Table 5 the results are summarized. Only glyceraldehyde was determined as intermediary at 20 min, according to literature [112,113]. Therefore, the mechanism corresponds to an indirect route, which is mediated by hydroxyl radicals. However, the determination of accurate mechanism is outside of the scope of the current work. A schematic representation of this process is shown in Fig. 21.

Table 5. Retention time and areas acquired from GC obtained for 1 M glycerol solution and solutions obtained from PEC glycerol oxidation after 1 hour, 1.5 hours and 2 hours. The retention times are given in minutes.

Initial solution		**After 1 hour**		**After 1.5 hour**		**After 2 hour**	
Retention time	Area	Retention time	Area	Retention time	Area	Retention time	Area
						1.850	2.36112
		22.703	137.67644	22.698	137.59741	22.90	28.2282
28.873	171.04857	28.730	30.46751				
		28.968	84.8139				

Figure 21. Indirect photoelectrocatalytic mechanism of glycerol degradation mediated by hydroxyl radicals according to [112,113].

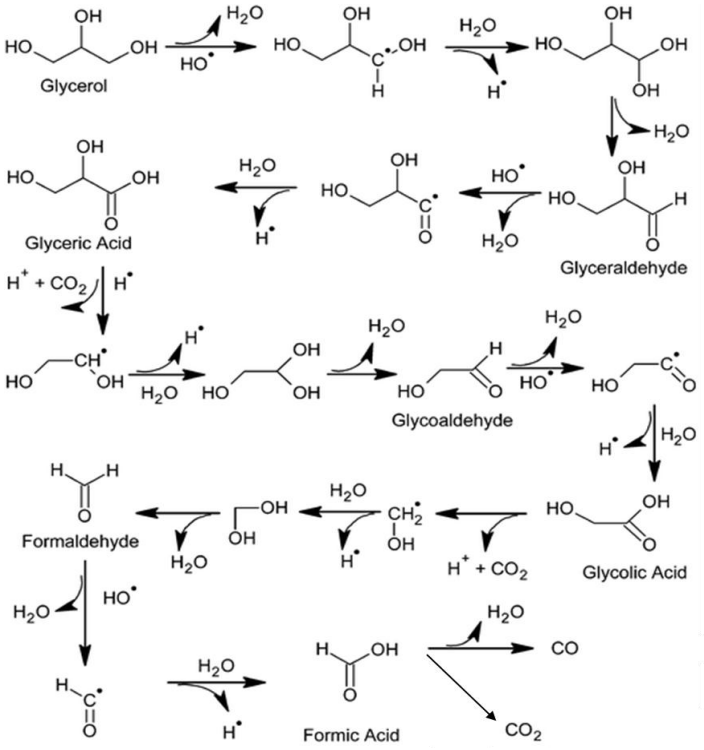

4.2 VARIATION OF THE HYDROTHERMAL MODIFIED METHOD BY USING DIP-COATING TECHNIQUE

4.2.1 Morphological, structural and optical characterization of DC-T and DC-TG photoanodes. Fig. 22a-b shows the FESEM images of DC-T and DC-TG photoanodes. For DC-T (Fig. 22a-a''), highly dispersed grains on nanotubes top with size around 1 μm were observed. Also, vertically oriented NT's are appreciated. The average wall width was found to be 28.81 nm while the wall thickness of TNT photoanodes was 25.03 nm, the increase of nanotube wall of about ~4 nm is due to a coating around TiO_2 nanotubes. EDS analysis showed the presence of oxygen, titanium, carbon and chlorine in atomic percentages of

62.37%, 32.89%, 4.61% and 0.13%, respectively. Fig. 22b-b'', shows the DC-TG photoanode surface. Separated nanotubes were observed. The increment in wall thickness from 25 nm to 42 nm results from the coating. EDS elemental composition evidenced the presence of oxygen, titanium and carbon with percentages of 60.83%, 36.71% and 2.46%, respectively. As shown in the EDS analyses, the elemental composition of the coatings was not elucidated. To confirm the identity of the coatings a characterization by Raman spectroscopy and XPS was performed.

Figure 22. Top-view FESEM images of (a-a'') DC-T and (b-b'') DC-TG photoanodes.

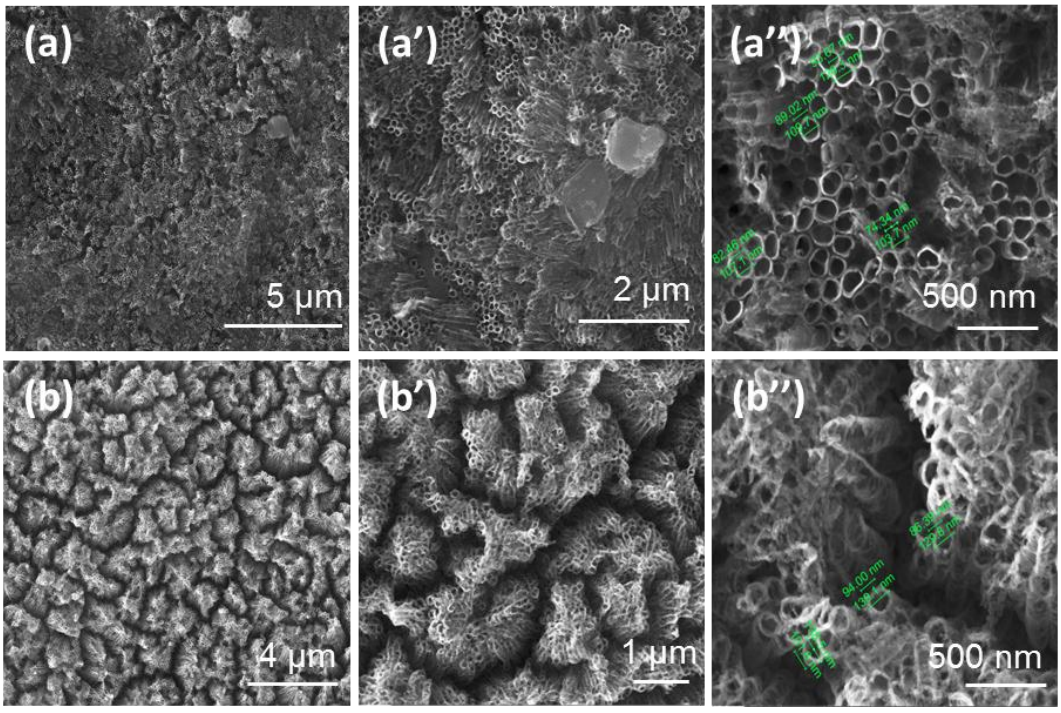

Raman spectra of DC-T and DC-TG photoanodes are shown in Fig. 23a,f. Ti foil, TNT and G photoanodes are presented for comparison (Fig. 23c,d,e). Analysis of the Raman spectra showed anatase (A) in TNT, G, DC-T and DC-TG photoanodes which is confirmed by the bands at 144, 197, 394, 516 and 634 cm^{-1} assigned to E_g, E_g, B_{1g}, A_{1g}, and B_{1g} vibrations [44]. The band at 318 cm^{-1} is coming from

superficial components of titanium foil (T) (Fig. 23c). For DC-T and DC-TG photoanodes, additional bands at 216 cm^{-1}, 242 cm^{-1}, 305 cm^{-1} and 416 cm^{-1} exhibit the appearance of a new phase, Fe_2TiO_5 (*). To confirm the existence of this novel phase, a comparison from literature was performed (Fig. 23b) [114]. Also, there were no bands related to magnetite, maghemite and/or cobalt ferrite. The iron titanate Fe_2TiO_5 (T) has been synthesized under similar conditions via solvothermal method by Bassi et al. [115]. On the other hand, G photoanode showed the D and G bands corresponding to graphene oxide modes [45]. It is important to note that D and G bands in DC-TG photoanode are overlapped by the fluorescence effect observed in this spectral region caused by iron inside TiO_2 [116].

Figure 23. Raman spectra of (a) DC-T (b) Fe_2TiO_5 obtained from literature [114] (c) Ti foil (d) TNT (e) G (f) DC-TG photoanodes. (A) TiO_2 anatase, (*) Fe_2TiO_5, (T) Titanium foil, D and G indicate graphene oxide vibrations.

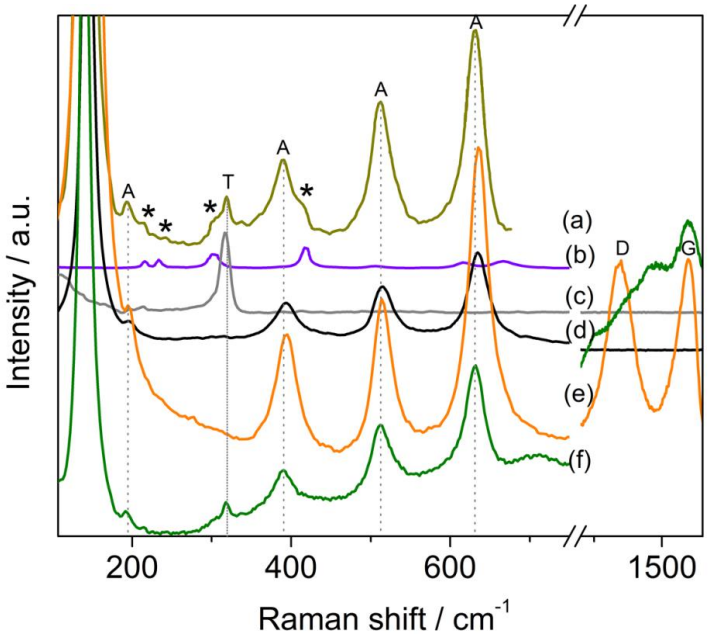

To confirm the results obtained from Raman spectroscopy, an XPS analysis was carried out. In Fig. 24 are shown the XPS high-resolution spectra of DC-TG and

TNT photoanodes. For comparison, in table 6 are shown the XPS contributions for all photoanodes. For DC-TG photoanode, the presence of C, O, N, F, Ti and Fe was observed. For C 1s spectrum, seven peaks were obtained. Binding energies at 283.0, 284.0, 284.6, 285.3, 286.0, 287.5 and 288.9 eV confirms the presence of O-Ti-C, C=C, C-C, C-O-H, C-O, C-N and O=C-O bonds, respectively [53,54]. When DC-TG photoanode is compared with TNT, G, F and FG photoanodes, carbon substitutional is observed. This is coming from ethylene glycol or the environment as shown previously. Also, the C-N bond suggests the presence of nitrogen functional groups. In the case of O 1s, seven contributions were obtained. Peaks at 528.3 and 529.4 eV are associated with oxygen incorporated in heterostructures which containing iron-titanium species [71]. The peak at 530 eV corresponds to the typical Ti-O bond from TiO_2 [78]. Peaks at 530.9, 532.3, 533.7 and 535.5 eV, agrees with OH, C-O-H, C=O and O=C-O-H groups, respectively [78,79]. The peak at 399.7 for N 1s high-resolution spectrum, indicates nitrogen into substitutional voids coming from NH_4F [53,57]. Also, a new peak at 398.3 eV for DC-TG photoanode, indicates the presence of C=N-C (pyridinic) bonds given by a graphene oxide modification from urea used in synthesis process. It is possible that a pyrrolic peak would be overlapped with nitrogen substitutional peak. For F 1s high-resolution spectrum, is also obtained a weak peak at 684.2 eV from the NH_4F compound [64]. In the case of Ti 2p spectrum, the signal typical from Ti^{4+} was found at 458.3 eV, while the signal at 459.3 eV, is related to Ti-O-Fe bonds [61]. For Fe 2p high resolution spectrum, the formation of a new phase is confirmed by the peak at 714.1 eV which could correspond with Fe^{3+} from Fe_2TiO_5, while the peak at 710.3 eV is proposed to correspond to Fe^{3+} in Fe-O-Ti bonds [117].

Figure 24. XPS high-resolution spectra of C 1s, O 1s, N 1s, F 1s, Ti 2p and Fe 2p for TNT and DC-TG photoanodes, as indicated in the figure legends.

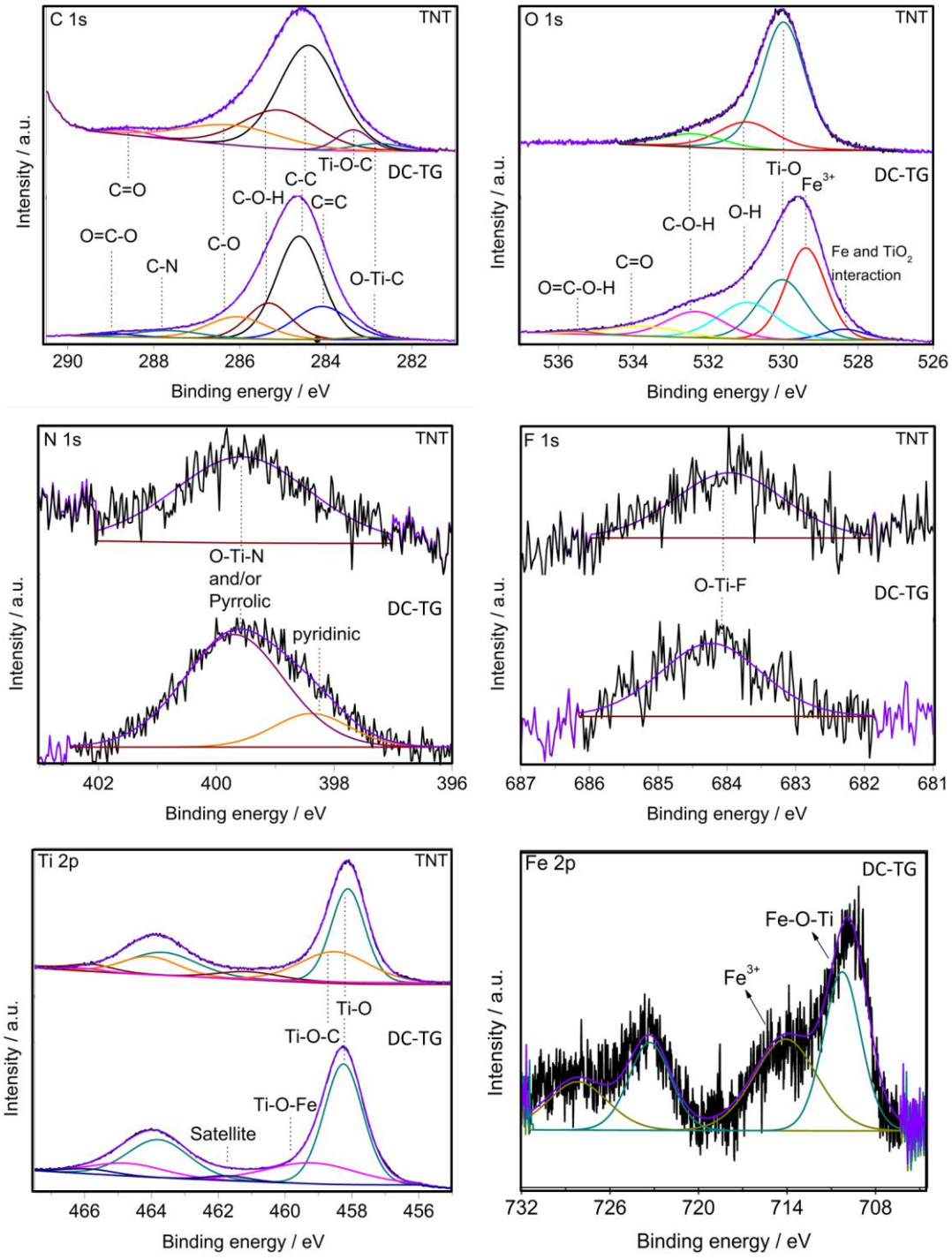

Table 6. XPS contributions for all photoanodes.

		TNT	G	F	FG	DC-TG	Ref.
Elem.	**Bonds**	**Binding energy (eV)**					
C	O-Ti-C	282.7	282.3	282.1	283.1	283.0	[53,54]
	Ti-O-C	283.3	283.4				[53,74, 75]
	C=C		284.1			284.0	[53,74, 75]
	C-C	284.6	284.6	284.6	284.6	284.6	[53,54]
	C-O-H	285.2	285.5	285.2	285.5	285.3	[53,54]
	C-O	286.3	286.6	286.4	286.2	286.0	[53,54]
	C-N				287.0	287.5	[55,56]
	C=O	288.4	287.5	288.1	288.1		[53,54]
	O=C-O		288.9		288.9	288.9	[53,74, 75]
N	Ti-O-N (Interstitial)			396.7	396.3		[58]
	C-N=C (Pyridinic)				398.1	398.3	[46]
	O-Ti-N (substitutional), or C-NH-C (pyrrolic), or N=C-O-H (pyridonic)	399.6	399.3	399.2	399.7	399.7	[53,57] [46]
	Quaternary nitrogen				402.2		[59]
	N-oxide				404.1		[60]
Ti ($2p_{3/2}$)	Ti-O-Ti	458.0	458.0	458.1	458.2	458.3	[76]
	Ti-O-C (interstitial)	458.8	458.4				[62,77]
	Ti-O-Fe			459.8	459.6	459.3	[61,63]
F	O-Ti-F	684.0	683.9	684.0	683.9	684.2	[64]

Fe ($2p_{3/2}$)	Fe^{2+} Fe_3O_4			709.9	709.4		[61,65–67]
	Ti-O-Fe, or Fe^{3+} γ-Fe_2O_3, or Fe^{3+} octahedral $CoFe_2O_4$			710.9	710.7	710.3	[61] [61,65–67] [68]
	Fe^{3+} tetrahedral $CoFe_2O_4$			712.6	712.2		[68]
	Fe^{3+} from Fe_2TiO_5					714.1	[117]
Co	Co^{2+} octahedral $CoFe_2O_4$			780.5	780.9		[68,70]
	Co^{2+} tetrahedral $CoFe_2O_4$			784.6	785.0		[68,70]
O	Interaction Fe_3O_4 with TiO_2				527.8	528.3	[71]
	Fe-O bonds			529.3	529.4	529.4	[71]
	Ti-O	529.9	529.8	530.2	530.0	530.0	[76] [78] [72]
	γ-Fe_2O_3 and Fe_3O_4			530.8	530.7		[65]
	OH	530.9				530.9	[78]
	$CoFe_2O_4$			531.3	531.5		[68]
	C-O-H	532.3	532.0	532.1	532.3	532.3	[79]
	C=O		534.2	533.4	533.2	533.7	[73]
	O=C-O-H		535.8		535.4	535.5	[73]

Optical properties were evaluated from modified Kubelka-Munk function versus energy absorption (Fig. 25). As shown previously, TNT, G, F and FG photoanodes exhibited an absorption edge about 3.2 eV typical from TiO_2 anatase. Also, an absorption edge of 1.42 eV was observed for TNT photoanode.

Figure 25. Kubelka-Munk function vs energy absorption of (a) TNT (b) G (c) DC-T and (d) DC-TG photoanodes. Inset shows the zoom view of photon energy.

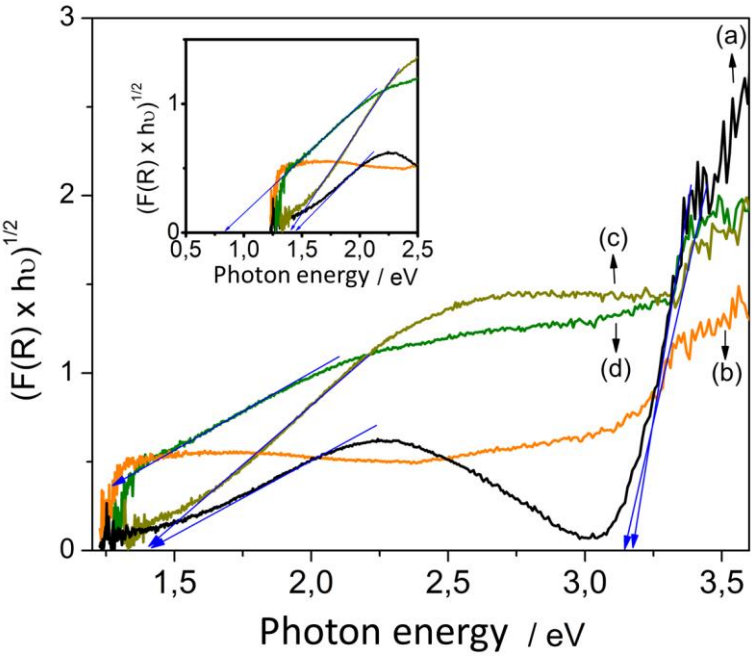

In the case of DC-T and DC-TG photoanodes a broadened of the absorption was observed. Have into account that the band gap value of Fe_2TiO_5 is 2.1 eV, it is suggested that absorptions in 2.1 eV corresponds to iron titanate [118]. In addition, absorption edges of 1.39 and 0.85 eV for DC-T and DC-TG photoanodes indicates that additional energetic states are included inside TiO_2 band gap (Fig. 25c,d). These states could come from iron given by the appearance of Ti-O-Fe bonds. This result indicates that the photoactivation of the photoanode could be carry out using lower energies, also it can be observed an improvement of visible light

harvesting after Fe_2TiO_5–GO sensitization. Elghniji et al. showed a Fe^{3+} ions diffusion to the surface of TiO_2 during heat treatment, which promotes a red shift of the TiO_2 absorption edge and an enhancement of light absorption in the visible light region [119].

4.2.2 Photoelectrochemical characterization of DC-T and DC-TG photoanodes. As shown previously, OCP represents an indirect measurement of energetic level of electrons in the semiconductor under illumination. This occur taking into account that under illumination electrons are accumulated in conduction band, while holes in valence band are transported to semiconductor/electrolyte interface to reacts with water. This set of phenomena caused a potential shift to negative values which is represented in OCP plots (Fig. 26). The V_{ph} values obtained for DC-TG, DC-T, G and TNT photoanodes were 0.194 V, 0.225 V, 0.085V and 0.097 V, respectively (Fig. 26a-d).

Figure 26. OCP measurements of (a) TNT (b) G (c) DC-T and (d) DC-TG photoanodes. Measurement conditions: active area of 2.4 cm^2, 0.1 M KH_2PO_4 and K_2HPO_4 electrolyte at pH 6.8. Light Source: LED driver λ = 655 nm.

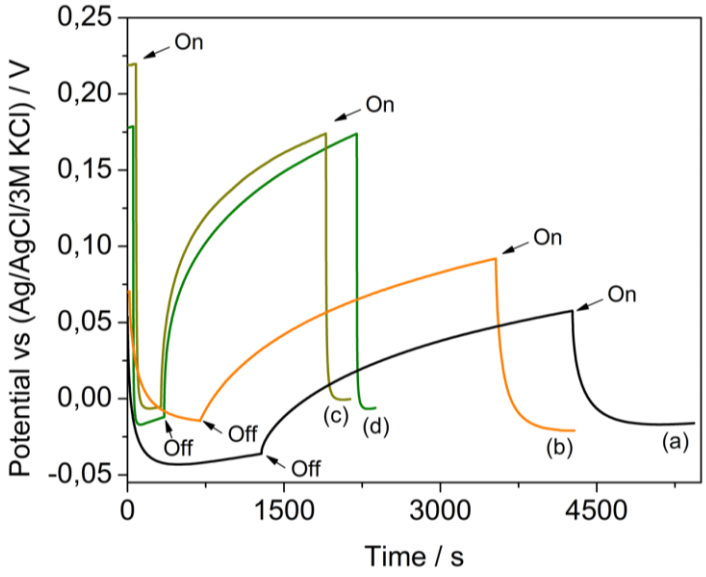

Despite DC-T photoanode exhibited the highest V_{ph} value, the potential decay do not reached the initial potential when illumination is retired. This decreases their availability to carry out reactions and therefore diminish its photocatalytic activity in comparison to DC-TG. On the other hand, DC-TG photoanode exhibited a higher V_{ph} value with respect to G and TNT photoanodes and reached the initial potential after a first illumination cycle indicating an improvement in photocatalytic activity. To compare V_{ph} values of DC-TG and DC-T photoanodes 0.194 V and 0.225 V with FG and F values 0.129 V and 0.122 V, it can be inferred that those prepared with DC technique would present higher photocatalytic activities. OCP measurements in presence of glycerol confirmed that glycerol acts as hole scavenger increasing the V_{ph} (Fig. 27). In table 7 is shown a summary of the V_{ph} generated under illumination in absence and presence of glycerol.

Figure 27. OCP measurements of (a) G (b) TNT (c) DC-T and (d) DC-TG photoanodes in presence of glycerol. Measurement conditions: active area of 2.4 cm^2, 0.1 M KH_2PO_4 and K_2HPO_4 and 1 mM glycerol at pH 6.8. Light Source: LED driver λ = 655 nm.

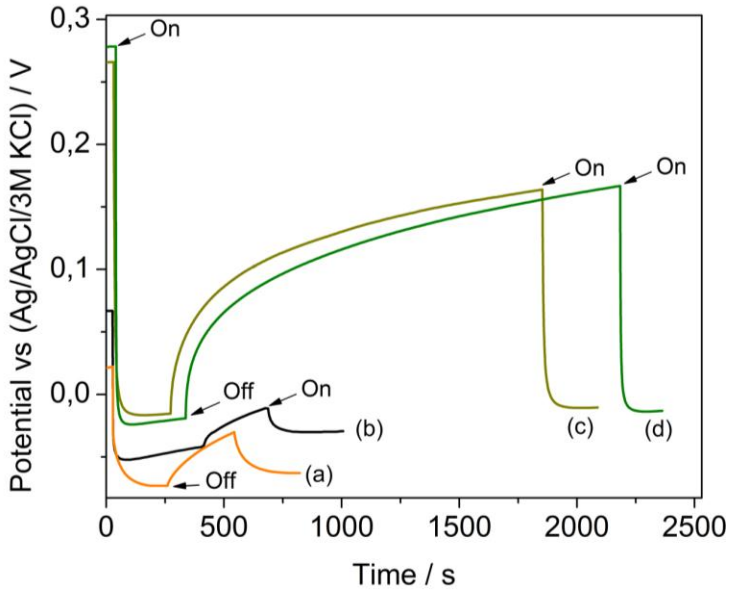

Table 7. Photopotential generated by TNT, G, F, FG, DC-T and DC-TG photoanodes in absence and presence of glycerol (V vs Ag/AgCl 3 M KCl).

Photoanode	G	TNT	F	FG	DC-T	DC-TG
V_{ph} glycerol absence	0.085	0.097	0.122	0.129	0.225	0.194
V_{ph} glycerol presence	0.094	0.118	0.128	0.144	0.281	0.302

LSV measurements of DC-TG, DC-T, G and TNT photoanodes are shown in Fig. 28, Table 8. For DC-T and DC-TG photoanodes an increment in photocurrent density is observed (Fig. 28c,d). TNT and G photoanodes are presented with comparative purposes (Fig. 28a,b). The photocurrent improvement of DC-T and DC-TG photoanodes is due to contribution of Fe_2TiO_5 sensitizer and states inter-band gap in TNT.

Figure 28. LSV of (a) TNT (b) G (c) DC-T and (d) DC-TG photoanodes using chopped light of 655 nm. Measurement conditions: active area of 2.4 cm^2, 1 mM glycerol and 0.1 M KH_2PO_4 and K_2HPO_4 electrolyte at pH 6.8 and 10 mV s^{-1}.

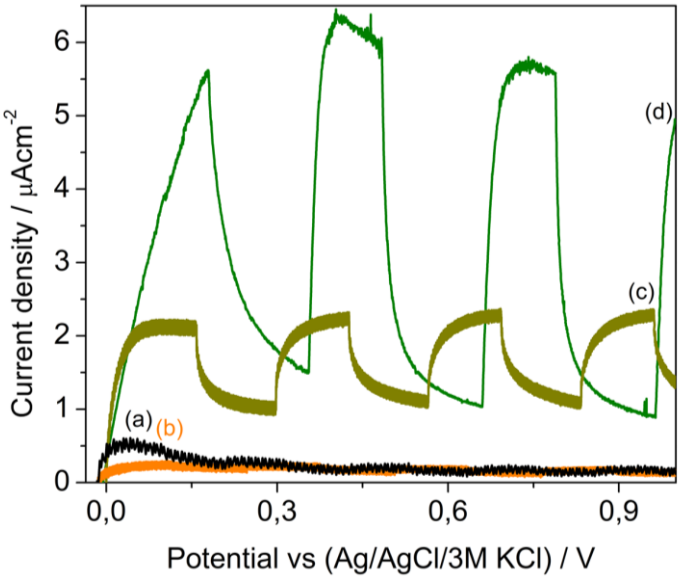

Some of these states could come from Fe^{3+} which inhibits the electron-hole pairs recombination. The mechanism of photoactivation indicates that e^- photogenerated in TiO_2 becomes Fe^{3+} ions in Fe^{2+} near to conduction band [119]. The low stability of Fe^{2+} compared to Fe^{3+} species, promotes a release of an electron to regenerate the Fe^{3+}. At the same time, Fe^{3+} states near to valence band acts as a holes trap becoming in Fe^{4+}. The Fe^{4+} obtained from Fe^{3+} oxidation are again reduced to Fe^{3+} by scavenging electron, while surface hydroxyl group transform into hydroxyl radical. These factors inhibit the recombination of photogenerated electron-hole pairs [119].

The difference between the photocurrent under illumination and current in dark conditions (ΔI_0) in the potential region of 0.8 V is shown in table 8. The ΔI_0 for DC-T and DC-TG photoanodes are 1.3400 and 4.9160 μA cm^{-2}, respectively, while for G, TNT, F, FG and A-FG photoanodes are 0.1230, 0.1341, 0.1504, 1.5450 and 0.1589 μA cm^{-2}, respectively.

Table 8. Difference between photocurrent under illumination and current under dark conditions generated by TNT, G, F, FG, A-FG, DC-T and DC-TG photoanodes (μA cm^{-2}).

Photoanode	**G**	**TNT**	**F**	**FG**	**A-FG**	**DC-T**	**DC-TG**
Maximum photocurrent	0.2180	0.2379	0.6469	2.310	2.9576	2.3600	5.8000
Minimum current	0.0950	0.1038	0.4965	0.7650	2.7987	1.0200	0.8840
Difference (ΔI_0)	0.1230	0.1341	0.1504	1.5450	0.1589	1.3400	4.9160
Maximum photocurrent	0.4337	0.4439	0.7520	2.3010	0.6610	4.1048	11.981
Minimum current	0.2160	0.1751	0.6030	0.7040	0.5820	1.0868	0.9503
Difference (ΔI_g)	0.2177	0.2688	0.1490	1.5960	0.0790	3.0180	11.0307

It can be observed higher ΔI_0 in DC-T and DC-TG photoanodes when are compared with those prepared by modified hydrothermal synthesis. This can be explain by the iron diffused into TNT's and also by PEC properties of Fe_2TiO_5 compared to the mixture of $CoFe_2O_4$, Fe_3O_4 and γ-Fe_2O_3. In DC-T and DC-TG photoanodes the amount of solution deposited on TNT lower than the used in FG and F photoanodes. This low amount of iron compared with modified hydrothermal method was crucial in the formation of sub-band gap states which improve the PEC responses. Recently, studies of iron quantity into TiO_2 in the increase of photocurrent have been carried out [119,120]. If the iron exceeds the optimum amount, an upward band bending occurs in Fe_2TiO_5/TiO_2 interface generating an energetic barrier to electron transport. On the other hand, LSV plots exhibited a current plateau for DC-T and DC-TG photoanodes indicating that in this potential range the photoanodes are highly stable.

In presence of glycerol (Fig. 29), the effect of current doubling for DC-T and DC-TG photoanodes is observed. As discussed previously, the effect is related to direct glycerol oxidation. Taking into account that the O 1s high-resolution XPS spectrum of DC-TG photoanode exhibited a hydroxylated surface, the direct oxidation could be a consequence of the strong adsorption of glycerol on the photoanode surface. In table 8 are shown the differences between photocurrent under illumination and under dark conditions in presence of glycerol (ΔI_g) for all photoanodes, where the highest value corresponds to DC-TG photoanode.

Figure 29. LSV of (a) TNT (b) G (c) DC-T and (d) DC-TG photoanodes under chopped light of 655 nm. Measurement conditions: active area of 2.4 cm^2, 1 mM glycerol and 0.1 M KH_2PO_4 and K_2HPO_4 electrolyte at pH 6.8 and 10 mV s^{-1}.

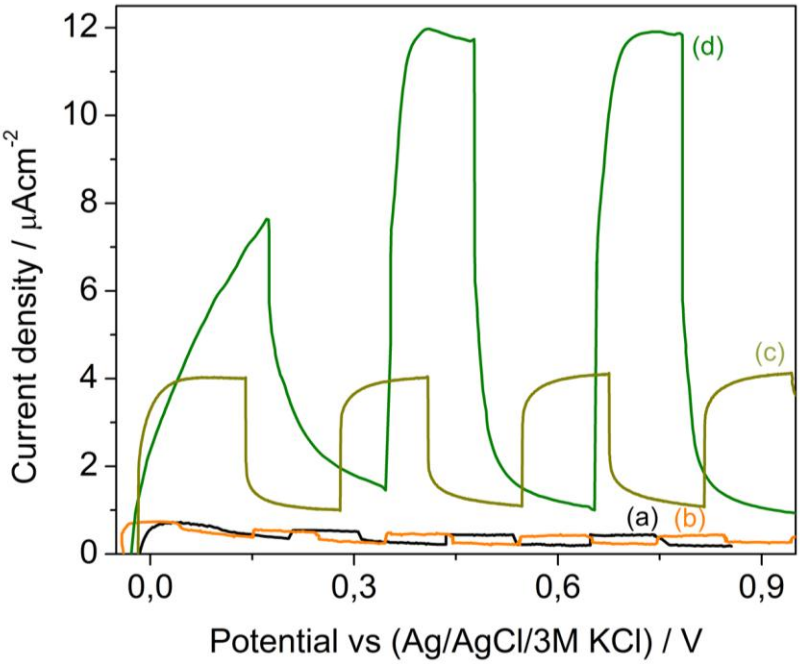

To evaluate the photoanodes stability at a potential of 0.8 V, photocurrent transients of DC-T and DC-TG photoanodes were carried out (Fig. 30). For DC-T and DC-TG photoanodes higher photocurrent densities were obtained (Fig. 30c,d). On the contrary, TNT and G photoanodes exhibited lower photocurrent densities (Fig. 30a,b). This indicates a positive effect in PEC response after TNT modification. The enhanced charge carrier transfer is due to Fe_2TiO_5/TiO_2 heterojunction separates effectively electrons and holes. This has been further investigated by Liu et al., where a direct electron injection from Fe_2TiO_5 to TNT was observed [114]. Furthermore, GO decreases recombination rates, trapping electrons and conducting them efficiently to the TNT surface. Comparing the photoanodes PEC responses obtained by the modified hydrothermal treatment with those obtained by the DC technique, the activity is suggested as follows: DC-

TG > DC-T > FG > F. In both cases, GO has a positive effect in the increasing of photocurrent density.

Figure 30. Photocurrent transients at 0.8 V of (a) TNT (b) G (c) DC-T and (d) DC-TG photoanodes. Measurement conditions: active area of 2.4 cm^2, 0.1 M KH_2PO_4 and K_2HPO_4 at pH 6.8. Light Source: LED driver λ = 655 nm.

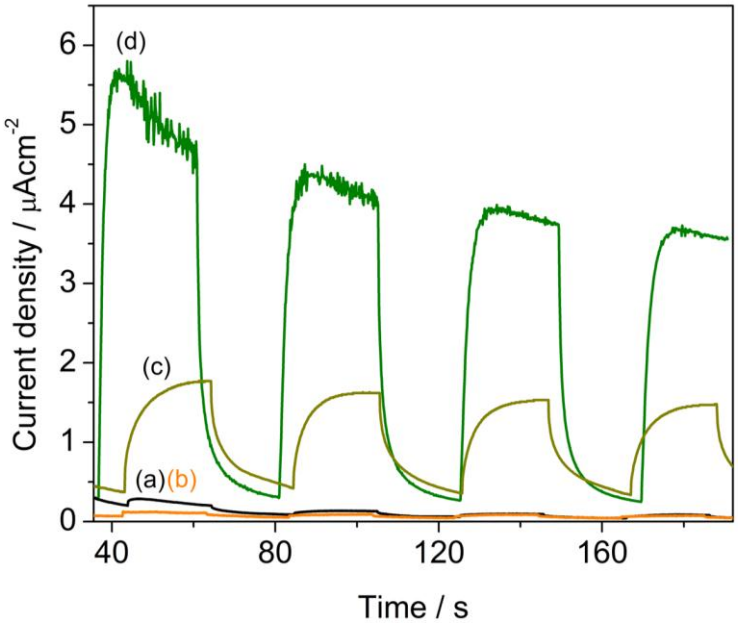

4.2.3 Photoelectrochemical glycerol oxidation. Fig. 31 shows the PEC glycerol oxidation activity using TNT, G, DC-T and DC-TG photoanodes. The applied potential was 0.8 V for 1 hour under visible light-illumination. The crude and pure glycerol solutions were used. The PEC pure glycerol oxidation exhibited 90%, 72%, 70% and 42% for DC-TG, DC-T, TNT and G photoanodes. This is in accordance with the activity proposed by photoelectrochemical measurements, where the oxidation follows the tendency: DC-TG > DC-T > TNT > G. In the case of crude glycerol, the DC-TG, DC-T, TNT and G photoanodes showed 78%, 70%, 50% and 36%, respectively.

Figure 31. C/C_o versus time plots obtained of PEC glycerol oxidation in crude and pure glycerol solutions using TNT, G, DC-T and DC-TG photoanodes.

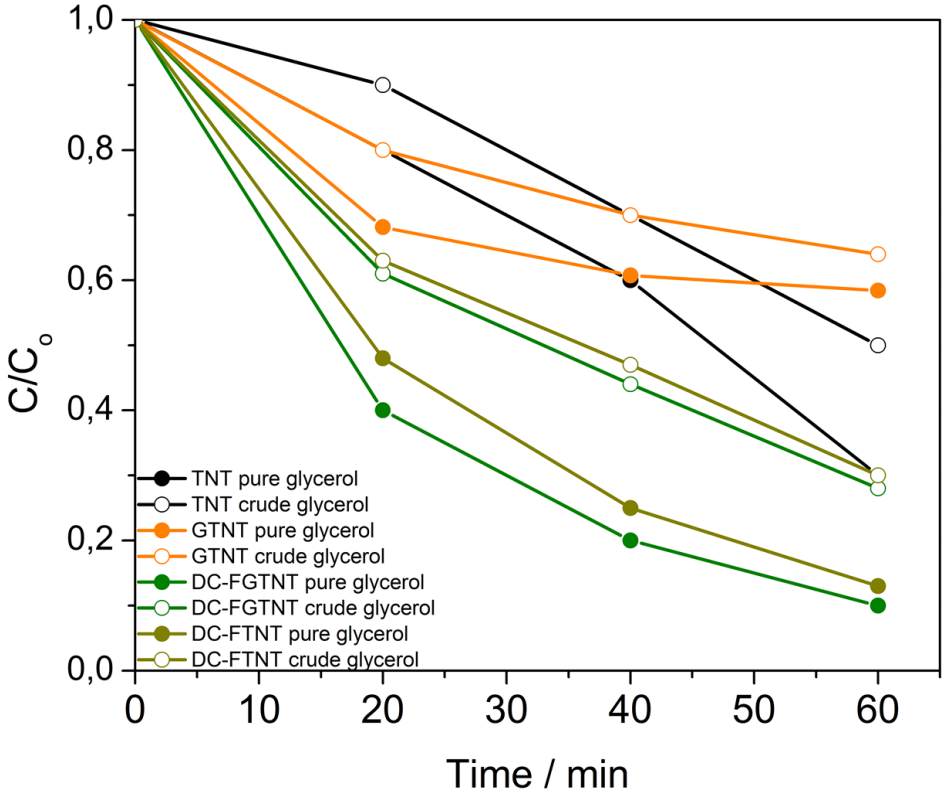

5. CONCLUSIONS

TNT photoanodes modified with GO and cobalt ferrite were prepared by hydrothermal modified route and dip-coating technique. In the case of hydrothermal synthesis, F and FG photoanodes were doped with C, N, F and Fe, which extended their absorption to visible region. A synergetic effect was established between TiO_2 (n-type) and $CoFe_2O_4$ (p-type), which promoted the injection of photogenerated electrons from the last to the former semiconductor. Incorporation of GO enhances the electron-hole separation, increasing both the photocurrent response and photocatalytic activity in FG photoanode. The photoelectrocatalytic degradation of glycerol on FG photoanode followed an oxidation through hydroxyl radical, hence an indirect mechanism was carried out. Contrary, a direct mechanism was observed on DC-TG photoanode obtained by dip-coating. Likewise, DC-TG photoanode showed the greater photocatalytic activity in regard to that obtained by the same synthesis route, which confirms the synergetic effect between TiO_2 and Fe_2TiO_5. In addition, DC-TG photoanode presented the highest photoactivity, because the synthesis rout prevents the formation of secondary oxides. The heterojunction between TiO_2 and either $CoFe_2O_4$ or Fe_2TiO_5 increase the capacitive behavior, which could be exploited for applications in energy storing devices.

6. RECOMMENDATIONS

Investigate other routes of synthesis to obtain $CoFe_2O_4$ in a more pure way.

To determine the optimum quantity of iron modifier to increase the photocatalytic activity of TNT photoanode.

To determine by GC-MS all the intermediaries produced during glycerol photo oxidation to propose an accurate mechanism of the reaction.

To measure total organic carbon (TOC) to monitor the mineralization of glycerol.

REFERENCES

[1] D.A. Keane, K.G. McGuigan, P. Fernández Ibáñez, M.I. Polo-López, A.J. Byrne, P. Dunlop, K. O'Shea, D. Dionysiou, S. Pillai, Solar photocatalysis for water disinfection : Materials and reactor design, *Catal. Sci. Technol.* 2014, 4, p. 1211–1226.

[2] Z. Gholami, A.Z. Abdullah, K.T. Lee, Dealing with the surplus of glycerol production from biodiesel industry through catalytic upgrading to polyglycerols and other value-added products, *Renew. Sustain. Energy Rev.* 2014, 39, p. 327–341.

[3] H.W. Tan, A.R. Abdul Aziz, M.K. Aroua, Glycerol production and its applications as a raw material: A review, *Renew. Sustain. Energy Rev.* 2013, 27, p. 118–127.

[4] J. Nowotny, M.A. Alim, T. Bak, M.A. Idris, M. Ionescu, K. Prince, M.Z. Sahdan, K. Sopian, M. Teridi, W. Sigmund, Defect chemistry and defect engineering of TiO_2-based semiconductors for solar energy conversion, *Chem. Soc. Rev.* 2015,.

[5] Y. Deng, R. Zhao, Advanced Oxidation Processes (AOPs) in Wastewater Treatment, *Curr. Pollut. Reports*. 2015, 1, p. 167–176.

[6] I. Sirés, E. Brillas, M.A. Oturan, M.A. Rodrigo, M. Panizza, Electrochemical advanced oxidation processes: today and tomorrow . A review, *Environ. Sci. Pollut. Res.* 2014, 21, p. 8336–8367.

[7] T.A. Egerton, P.A. Christensen, Advanced Oxidation Processes for Water and Wastewater Treatment, Simons Par, IWA, 2004.

[8] T. Ochiai, A. Fujishima, Photoelectrochemical properties of TiO_2 photocatalyst and its applications for environmental purification, *J. Photochem. Photobiol. C Photochem. Rev.* 2012, 13, p. 247–262.

[9] Y. Hou, X.Y. Li, Q.D. Zhao, X. Quan, G.H. Chen, Electrochemical Method for Synthesis of a $ZnFe_2O_4/TiO_2$ Composite Nanotube Array Modified Electrode with Enhanced Photoelectrochemical Activity, *Adv. Funct. Mater.* 2010, 20, p.

2165–2174.

[10] M. Law, L.E. Greene, J.C. Johnson, R. Saykally, P. Yang, Nanowire dye-sensitized solar cells, *Nat. Mater.* 2005, 4, p. 455–459.

[11] J. Bisquert, A. Zaban, M. Greenshtein, I. Mora-Seró, Determination of Rate Constants for Charge Transfer and the Distribution of Semiconductor and Electrolyte Electronic Energy Levels in Dye-Sensitized Solar Cells by Open-Circuit Photovoltage Decay Method, *J. Am. Chemi*. 2004, 126, p. 13550–13559.

[12] H.C. Liang, X.Z. Li, Effects of structure of anodic TiO_2 nanotube arrays on photocatalytic activity for the degradation of 2,3-dichlorophenol in aqueous solution, *J. Hazard. Mater.* 2009, 162, p. 1415–1422.

[13] A.M. Mohamed, A.S. Aljaber, S.Y. AlQaradawi, N.K. Allam, TiO_2 nanotubes with ultrathin walls for enhanced water splitting, *Chem. Commun. (Camb).* 2015, 51, p. 12617–20.

[14] K. Liang, X. Chen, Z. Guo, T. Hou, X. Zhang, Y. Li, Lithium intercalation and diffusion in TiO_2 nanotubes: a first-principles investigation, *Phys. Chem. Chem. Phys.* 2016, 18, p. 24370–24376.

[15] A. Selloni, Anatase shows its reactive side. Fluorine-containing species can cause titania to crystallize with an unusually large fraction of reactive {001} facets, *Nat. Mater.* 2008, 7, p. 613–615.

[16] X. Yang, C. Cao, L. Erickson, K. Hohn, R. Maghirang, K. Klabunde, Photo-catalytic degradation of Rhodamine B on C-, S-, N-, and Fe-doped TiO_2 under visible-light irradiation, *Appl. Catal. B Environ.* 2009, 91, p. 657–662.

[17] D. Ramírez-ortega, A.M. Meléndez, P. Acevedo-Peña, I. González, R. Arroyo, Semiconducting properties of ZnO/TiO_2 composites by electrochemical measurements and their relationship with photocatalytic activity, *Electrochim. Acta*. 2014, 140, p. 541–549.

[18] M. Batzill, E.H. Morales, U. Diebold, Influence of nitrogen doping on the defect formation and surface properties of TiO_2 rutile and anatase, *Phys. Rev. Lett.* 2006, 96, p. 1–4.

[19] B.L. Sharma, R.K. Purohit, Semiconductor Heterojunctions, Pergamon, 1974.

[20] H. Wang, L. Zhang, Z. Chen, J. Hu, S. Li, Z. Wang, J. Liu, X. Wang, Semiconductor heterojunction photocatalysts: design, construction, and photocatalytic performances, *Chem. Soc. Rev.* 2014, 43, p. 5234–44.

[21] J. Luo, X. Zhou, L. Ma, X. Xu, Enhanced visible-light-driven photocatalytic activity of WO_3/BiOI heterojunction photocatalysts, *J. Mol. Catal. A Chem.* 2015, 410, p. 168–176.

[22] B.X. Lei, W. Sun, Z.F. Sun, Synthesis of visible-light absorbing $CoFe_2O_4$ sensitized TiO_2 nanotube arrays electrode with enhanced photoelectrochemical performance, *Mater. Res. Bull.* 2013, 48, p. 3625–3629.

[23] C. Li, J. Wang, B. Wang, J. Gong, Z. Lin, A novel magnetically separable TiO_2/$CoFe_2O_4$ nanofiber with high photocatalytic activity under UV-vis light, *Mater. Res. Bull.* 2012, 47, p. 333–337.

[24] P. Sathishkumar, R. Mangalaraja, S. Anandan, M. Ashokkumar, $CoFe_2O_4$/TiO_2 nanocatalysts for the photocatalytic degradation of Reactive Red 120 in aqueous solutions in the presence and absence of electron acceptors, *Chem. Eng. J.* 2013, 220, p. 302–310.

[25] B.S. Holinsworth, D. Mazumdar, H. Sims, Q. Sun, M.K. Yurtisigi, S.K. Sarker, A. Gupta, W.H. Butler, J.L. Musfeldt, Chemical tuning of the optical band gap in spinel ferrites: $CoFe_2O_4$ vs $NiFe_2O_4$, *Appl. Phys. Lett.* 2013, 103,.

[26] C. Haw, W. Chiu, S. Abdul Rahman, P. Khiew, S. Radiman, R. Abdul Shukor, M.A. Hamid, N. Ghazali, The design of new magnetic-photocatalyst nanocomposites ($CoFe_2O_4$–TiO_2) as smart nanomaterials for recyclable-photocatalysis applications, *New J. Chem.* 2016, 40, p. 1124–1136.

[27] T.-F. Yeh, J. Cihlář, C.-Y. Chang, C. Cheng, H. Teng, Roles of graphene oxide in photocatalytic water splitting, *Mater. Today*. 2013, 16, p. 78–84.

[28] H. Cid, L. Argüello, A. Romano, C. Flores, M. Pérez, Síntesis y Caracterización de Grafeno, *Cent. Física Apl. Y Tecnol. Av.* 2012,.

[29] P. Song, X. Zhang, M. Sun, X. Cui, Y. Lin, Graphene oxide modified TiO_2 nanotube arrays: enhanced visible light photoelectrochemical properties, *Nanoscale*. 2012, 4, p. 1800.

[30] Y. Fu, H. Chen, X. Sun, X. Wang, Combination of cobalt ferrite and graphene: High-performance and recyclable visible-light photocatalysis, *Appl. Catal. B Environ.* 2012, 111–112, p. 280–287.

[31] I. Gómez, E. Mejía, R. Cabanzo, Synthesis of Graphene Oxide and Chemically Reduced Graphene Nanosheets, *Rev. Colomb. Mater.* 2013, 5, p. 177–184.

[32] J.P. Pineda Martínez, J.Z. Rojas Cristancho, Factores que afectan la polimerización del glicerol crudo para la producción de poliglicerol, Universidad Industrial de Santander, 2013.

[33] Ó.J. Martínez Santana, Y.A. Zorro Gutiérrez, Estudio de las variables de síntesis de poliuretanos a partir de aceite de ricino y glicerol crudo, Universidad Industrial de Santander, 2014.

[34] L. Zhang, J.C. Yu, Z. Zheng, C.W. Leung, Fabrication of hierarchical porous iron oxide films utilizing the Kirkendall effect, *Chem. Commun.* 2005, p. 2683–2685.

[35] Z. Xu, C. Shen, Y. Tian, X. Shi, H. Gao, Organic phase synthesis of monodisperse iron oxide nanocrystals using iron chloride as precursor, *Nanoscale*. 2010, 2, p. 1027–1032.

[36] a. Hunyek, C. Sirisathitkul, P. Harding, D.J. Harding, Structural and magnetic properties of cobalt ferrites synthesized using sol-gel techniques, *Mater. Sci.* 2012, 30, p. 278–281.

[37] V. Nguyen, M. Gauthier, O. Sandre, Templated Synthesis of Magnetic Nanoparticles through the Self-Assembly of Polymers and Surfactants, *Nanomaterials*. 2014, 4, p. 628–685.

[38] N.V. Long, Y. Yang, T. Teranishi, C.M. Thi, Y. Cao, M. Nogami, Related magnetic properties of $CoFe_2O_4$ cobalt ferrite particles synthesised by the polyol method with $NaBH_4$ and heat treatment: new micro and nanoscale

structures, *RSC Adv.* 2015, 5, p. 56560–56569.

[39] C. Karunakaran, P. Anilkumar, P. Gomathisankar, Photoproduction of iodine with nanoparticulate semiconductors and insulators, *Chem. Cent. J.* 2011, 5, p. 1–9.

[40] A. John K, J. Naduvath, S. Mallick, T. Shripathi, M. Thankamoniamma, R.R. Philip, A novel cost effective fabrication technique for highly preferential oriented TiO_2 nanotubes, *Nanoscale*. 2015, 7, p. 20386–20390.

[41] P. Raju, S.R. Murthy, Microwave-hydrothermal synthesis of $CoFe_2O_4$ - TiO_2 nanocomposites, *Adv. Mater. Lett.* 2013, 4, p. 99–105.

[42] W. Peternele, V. Monge Fuentes, M.L. Fascineli, J. Rodrigues Da Silva, R. Silva, C. Lucci, R. Bentes De Azevedo, Experimental Investigation of the Coprecipitation Method: An Approach to Obtain Magnetite and Maghemite Nanoparticles with Improved Properties, *J. Nanomater.* 2014,.

[43] N. Sanpo, A. Siao, M. Ang, F. Hasan, J. Wang, C.C. Berndt, Phases and microstructures of solution precursor plasma sprayed cobalt ferrite splats, in: Proc. 5th Asian Therm. Spray Conf., 2012: pp. 145–146.

[44] Y. Lai, L. Sun, Y. Chen, H. Zhuang, C. Lin, J.W. Chin, Effects of the Structure of TiO_2 Nanotube Array on Ti Substrate on Its Photocatalytic Activity, *J. Electrochem. Soc.* 2006, 153, p. D123–D127.

[45] V. Stengl, S. Bakardjieva, T.M. Grygar, J. Bludská, M. Kormunda, TiO_2-graphene oxide nanocomposite as advanced photocatalytic materials, *Chem. Cent. J.* 2013, 7,.

[46] J. Ma, A. Habrioux, Y. Luo, G. Ramos, L. Calvillo, G. Granozzi, P. Balbuena, N. Alonso-Vante, Electronic Interaction between Platinum Nanoparticles and Nitrogen-doped Reduced Graphene Oxide: Effect on the Oxygen Reduction Reaction, *J. Mater. Chem. A*. 2013, p. 1–15.

[47] N. Sanpo, C. Wen, C. Berndt, J. Wang, Advanced functional materials: Multifunctional Spinel Ferrite Nanoparticles for Biomedical Application, in: Adv. Funct. Mater., Lokman Uzun, Tiwari Ashutosh, Wiley, 2015: pp. 202–203.

[48] P. Chandramohan, M.P. Srinivasan, S. Velmurugan, S.V. Narasimhan, Cation distribution and particle size effect on Raman spectrum of $CoFe_2O_4$, *J. Solid State Chem.* 2011, 184, p. 89–96.

[49] A.P. Amaliya, S. Anand, S. Pauline, CTAB Assisted Synthesis of Cobalt Ferrite Nanoparticles and Its Characterizations, *J. Nanosci. Technol.* 2016, 2, p. 186–188.

[50] K.V. Sankar, R.K. Selvan, D. Meyrick, Electrochemical performances of $CoFe_2O_4$ nanoparticles and a rGO based asymmetric supercapacitor, *RSC Adv.* 2015, 5, p. 99959–99967.

[51] Y.-S. Li, J.S. Church, A.L. Woodhead, Infrared and Raman spectroscopic studies on iron oxide magnetic nano-particles and their surface modifications, *J. Magn. Magn. Mater.* 2012, 324, p. 1543–1550.

[52] O.N. Shebanova, P. Lazor, Raman spectroscopic study of magnetite ($FeFe_2O_4$): A new assignment for the vibrational spectrum, *J. Solid State Chem.* 2003, 174, p. 424–430.

[53] K. Siuzdak, M. Szkoda, M. Sawczak, A. Lisowska-Oleksiak, Novel nitrogen precursors for electrochemically driven doping of titania nanotubes exhibiting enhanced photoactivity, *New J. Chem.* 2015, 39, p. 2741–2751.

[54] J. Yu, G. Dai, Q. Xiang, M. Jaroniec, Fabrication and enhanced visible-light photocatalytic activity of carbon self-doped TiO_2 sheets with exposed {001} facets, *J. Mater. Chem.* 2011, 21, p. 1049–1057.

[55] H. Nolan, B. Mendoza-Sanchez, N. Ashok Kumar, N. McEvoy, S. O'Brien, V. Nicolosi, G.S. Duesberg, Nitrogen-doped reduced graphene oxide electrodes for electrochemical supercapacitors., *Phys. Chem. Chem. Phys.* 2014, 16, p. 2280–2284.

[56] D. Dreyer, S. Park, C. Bielawski, R. Ruoff, The chemistry of graphene oxide, *Chem. Soc. Rev.* 2010, 39, p. 228–240.

[57] P. Mazierski, M. Nischk, M. Gołkowska, W. Lisowski, M. Gazda, M. Winiarski, T. Klimczuk, A. Zaleska-medynska, Photocatalytic activity of nitrogen doped TiO_2 nanotubes prepared by anodic oxidation: The effect of

applied voltage, anodization time and amount of nitrogen dopant, *Appl. Catal. B Environ.* 2016, 196, p. 77–88.

[58] X. Liu, Y. Zhang, T. Wu, J. Huang, Hierarchical nanotubular titanium nitride derived from natural cellulose substance and its electrochemical properties, *Chem. Commun.* 2012, 48, p. 9992–9994.

[59] Y.C. Lin, C.Y. Lin, P.W. Chiu, Controllable graphene N-doping with ammonia plasma, *Appl. Phys. Lett.* 2010, 96,.

[60] B. Kumar, M. Asadi, D. Pisasale, S. Sinha-ray, B.A. Rosen, R. Haasch, J. Abiade, A.L. Yarin, A. Salehi-khojin, Renewable and metal-free carbon nanofibre catalysts for carbon dioxide reduction, *Nat. Commun.* 2013, 4, p. 2819.

[61] M. Pham, C. Dinh, G. Vuong, N. Ta, T. Do, Visible light induced hydrogen generation using a hollow photocatalyst with two cocatalysts separated on two surface sides †, *Phys. Chem. Chem. Phys.* 2014, 16, p. 5937–5941.

[62] A. Esfandiar, S. Ghasemi, A. Irajizad, O. Akhavan, M.R. Gholami, The decoration of TiO_2/reduced graphene oxide by Pd and Pt nanoparticles for hydrogen gas sensing, *Int. J. Hydrogen Energy*. 2012, 37, p. 15423–15432.

[63] A. Glisenti, The reactivity of a Fe-Ti-O mixed oxide under different atmospheres: Study of the interaction with simple alcohol molecules, *J. Mol. Catal. A Chem.* 2000, 153, p. 169–190.

[64] Q. Li, J.K. Shang, Self-Organized Nitrogen and Fluorine Co-doped Titanium Oxide Nanotube Arrays with Enhanced Visible Light Photocatalytic Performance, *Environ. Sci. Technol.* 2009, 43, p. 8923–8929.

[65] A. Grosvenor, B. Kobe, M. Biesinger, N. McIntyre, Investigation of multiplet splitting of Fe 2p XPS spectra and bonding in iron compounds, *Surf. Interface Anal.* 2004, 36, p. 1564–1574.

[66] R. Jung, H. Tsuchiya, S. Fujimoto, XPS characterization of passive films formed on Type 304 stainless steel in humid atmosphere, *Corros. Sci.* 2012, 58, p. 62–68.

[67] T. Fujii, F. Groot, G. Sawatzky, In situ XPS analysis of various iron oxide

films grown by NO_2-assisted molecular-beam epitaxy, *Phys. Rev. B*. 1999, 59, p. 3195–3202.

[68] Z. Zhou, Y. Zhang, Z. Wang, W. Wei, W. Tang, J. Shi, R. Xiong, Electronic structure studies of the spinel $CoFe_2O_4$ by X-ray photoelectron spectroscopy, *Appl. Surf. Sci.* 2008, 254, p. 6972–6975.

[69] K. Djebaili, Z. Mekhalif, A. Boumaza, A. Djelloul, XPS, FTIR, EDX, and XRD Analysis of Al_2O_3 Scales Grown on PM2000 Alloy, *J. Spectrosc.* 2015, p. 1–14.

[70] A. Walsh, K. Ahn, S. Shet, M. Huda, T. Deutsch, H. Wang, J. Turner, S.-H. Wei, Y. Yan, M. Al-Jassim, Ternary cobalt spinel oxides for solar driven hydrogen production: Theory and experiment, *Energy Environ. Sci.* 2009, 2, p. 774–782.

[71] W.S. Tung, W.A. Daoud, New Approach Toward Nanosized Ferrous Ferric Oxide and Fe_3O_4-doped Titanium Dioxide Photocatalysts., *ACS Appl. Mater. Interfaces*. 2009, 1, p. 2453–2461.

[72] S. Hejazi, N.T. Nguyen, A. Mazare, P. Schmuki, Aminated TiO_2 nanotubes as a photoelectrochemical water splitting photoanode, *Catal. Today*. 2016,.

[73] Y. Xie, T. Wang, O. Franklin, P. Sherwood, X-Ray Photoelectron Spectroscopic Studies of Carbon Fiber Surfaces. Part XVI: Core-Level and Valence-Band Studies of Pitch-Based Fibers Electrochemically Treated in Ammonium Carbonate Solution, *Appl. Spectrosc.* 1992, 46, p. 645–651.

[74] T. Yeh, J. Cihlar, C. Chang, C. Cheng, H. Teng, Roles of graphene oxide in photocatalytic water splitting, *Mater. Today*. 2013, 16, p. 78–84.

[75] M. Xing, X. Li, J. Zhang, Synergistic effect on the visible light activity of Ti(3+) doped TiO_2 nanorods/boron doped graphene composite., *Sci. Rep.* 2014, 4, p. 5493.

[76] S.W. Shin, J.Y. Lee, K. Ahn, S.H. Kang, J.H. Kim, Visible Light Absorbing TiO_2 Nanotube Arrays by Sulfur Treatment for Photoelectrochemical Water Splitting, *J. Phys. Chem. C*. 2015, 119, p. 13375–13383.

[77] G.M. Ingo, S. Dirè, F. Babonneau, XPS studies of SiO_2, -TiO_2, powders

prepared by sol-gel process, *Appl. Surf. Sci.* 1993, 710, p. 230–234.

[78] S.A. Pawar, D.S. Patil, U.T. Pawar, R.S. Devan, M.M. Karanjkar, Y.R. Ma, S.W. Shin, J.H. Kim, P.S. Patil, Photoelectrochemical solar cell based on surfactant mediated rutile TiO_2 nanorods, *J. Mater. Sci. Mater. Electron.* 2015, 26, p. 2595.

[79] N. Plylahan, S. Maria, T.N. Phan, M. Letiche, H. Martinez, C. Courrèges, P. Knauth, T. Djenizian, Enhanced electrochemical performance of Lithium-ion batteries by conformal coating of polymer electrolyte, *Nanoscale Res. Lett.* 2014, 9, p. 544.

[80] A. Nairan, M. Khan, U. Khan, M. Iqbal, S. Riaz, S. Naseem, Temperature-Dependent Magnetic Response of Antiferromagnetic Doping in Cobalt Ferrite Nanostructures, *Nanomaterials*. 2016, 6, p. 73.

[81] Y.H. Hou, Y.J. Zhao, Z.W. Liu, H.Y. Yu, X.C. Zhong, W.Q. Qiu, D.C. Zeng, L.S. Wen, Structural, electronic and magnetic properties of partially inverse spinel $CoFe_2O_4$: a first-principles study, *J. Phys. D. Appl. Phys.* 2010, 43, p. 445003.

[82] C. Chen, W. Cai, M. Long, B. Zou, Y. Wu, D. Wu, Y. Feng, Synthesis of Visible-Light Responsive Graphene Oxide/TiO_2 Composites with p/n Heterojunction, *ACS Nano*. 2010, 4, p. 6425–6432.

[83] M. Aleksandrzak, P. Adamski, W. Kukułka, B. Zielinska, E. Mijowska, Effect of graphene thickness on photocatalytic activity of TiO_2-graphene nanocomposites, *Appl. Surf. Sci.* 2015, 331, p. 193–199.

[84] T. Peng, K. Li, P. Zeng, Q. Zhang, X. Zhang, Enhanced Photocatalytic Hydrogen Production over Graphene Oxide−Cadmium Sulfide Nanocomposite under Visible Light Irradiation, *J. Phys. Chem. C*. 2012, 116, p. 22720–22726.

[85] S. Umrao, S. Abraham, F. Theil, S. Pandey, V. Ciobota, P. Shukla, C. Rupp, S. Chakraborty, R. Ahuja, J. Popp, B. Dietzek, A. Srivastava, A possible mechanism for the emergence of an additional band gap due to a Ti–O–C bond in the TiO_2–graphene hybrid system for enhanced photodegradation of

methylene blue under visible light, *RSC Adv.* 2014, 4, p. 59890–59901.

[86] K. Dai, T. Peng, D. Ke, B. Wei, Photocatalytic hydrogen generation using a nanocomposite of multi-walled carbon nanotubes and TiO_2 nanoparticles under visible light irradiation, *Nanotechnology*. 2009, 20, p. 1–6.

[87] R.A. Bepari, P. Bharali, B.K. Das, Controlled synthesis of α- and γ-Fe_2O_3 nanoparticles via thermolysis of PVA gels and studies on γ-Fe_2O_3 catalyzed styrene epoxidation, *J. Saudi Chem. Soc.* 2014,.

[88] M.H. Habibi, H.J. Parhizkar, FTIR and UV-vis diffuse reflectance spectroscopy studies of the wet chemical (WC) route synthesized nano-structure $CoFe_2O_4$ from $CoCl_2$ and $FeCl_3$, *Spectrochim. Acta - Part A Mol. Biomol. Spectrosc.* 2014, 127, p. 102–106.

[89] H. Ghandoor, H. Zidan, M. Khalil, M. Ismail, Synthesis and Some Physical Properties of Magnetite (Fe_3O_4) Nanoparticles, *Int. J. Electrochem. Sci.* 2012, 7, p. 5734–5745.

[90] D. Sharma, N. Khare, Tuning of optical bandgap and magnetization of $CoFe_2O_4$ thin films, *Appl. Phys. Lett.* 2014, 105, p. 1–5.

[91] D.H. Taffa, R. Dillert, A.C. Ulpe, K. Bauerfeind, T. Bredow, D. Bahnemann, M. Wark, Photoelectrochemical and theoretical investigations of spinel type ferrites ($M_xFe_{3-x}O_4$) for water splitting: a mini-review, *J. Photonics Energy*. 2016, 7, p. 1–24.

[92] R. Memming, Solar Energy Conversion By Photoelectrochemical Processes, *Electrochim. Acta*. 1980, 25, p. 77–88.

[93] K.S. Raja, V.K. Mahajan, M. Misra, Determination of photo conversion efficiency of nanotubular titanium oxide photo-electrochemical cell for solar hydrogen generation, *J. Power Sources*. 2006, 159, p. 1258–1265.

[94] H.U. Harten, The Semiconductor/Electrolyte Interface: Potentials, Charges and Carriers, *Electrochim. Acta*. 1968, 13, p. 1255–1261.

[95] W.S. dos Santos, M. Rodriguez, A.S. Afonso, J.P. Mesquita, L.L. Nascimento, A.O. Patrocínio, A.C. Silva, L.C. Oliveira, J.D. Fabris, M.C. Pereira, A hole inversion layer at the $BiVO_4/Bi_4V_2O_{11}$ interface produces a

high tunable photovoltage for water splitting, *Sci. Rep.* 2016, 6,.

[96] Y. Lin, Y. Xu, M. Mayer, Z. Simpson, G. McMahon, S. Zhou, D. Wang, Growth of p-Type Hematite by Atomic Layer Deposition and Its Utilization for Improved Solar Water Splitting, *J. Am. Chem. Soc.* 2012, 134, p. 5508–5511.

[97] C. Du, X. Yang, M.T. Mayer, H. Hoyt, J. Xie, G. McMahon, G. Bischoping, D. Wang, Hematite-based water splitting with low turn-on voltages, *Angew. Chemie - Int. Ed.* 2013, 52, p. 12692–12695.

[98] P. Wang, H. Wu, Y. Tang, R. Amal, Y.H. Ng, Electrodeposited Cu_2O as Photoelectrodes with Controllable Conductivity Type for Solar Energy Conversion, *J. Phys. Chem. C*. 2015, 119, p. 26275–26282.

[99] H.A. Becerril, J. Mao, Z. Liu, R.M. Stoltenberg, Z. Bao, Y. Chen, Evaluation of Solution-Processed Reduced Graphene Oxide Films as Transparent Conductors, *ACS Nano*. 2008, 2, p. 463–470.

[100] S. Shen, J. Jiang, P. Guo, L. Guo, Facile Growth of Porous Hematite Films for Photoelectrochemical Water Splitting, *Int. J. Photoenergy*. 2013, p. 1–9.

[101] Z. Xiang, X. Zhou, G. Wan, G. Zhang, D. Cao, Improving Energy Conversion Efficiency of Dye-Sensitized Solar Cells by Modifying TiO_2 Photoanodes with Nitrogen-Reduced Graphene Oxide, *ACS Sustain. Chem. Eng.* 2014, 2, p. 1234–1240.

[102] Y. Tang, C. Lee, J. Xu, Z. Liu, Z. Chen, Z. He, Y. Cao, G. Yuan, H. Song, L. Chen, L. Luo, H. Cheng, W. Zhang, I. Bello, S. Lee, Incorporation of Graphenes in Nanostructured TiO_2 Films via Molecular Grafting for Dye-Sensitized Solar Cell Application, *ACS Nano*. 2010, 4, p. 3482–3488.

[103] P. Karthika, Functionalized Exfoliated Graphene Oxide as Supercapacitor Electrodes, *Soft Nanosci. Lett.* 2012, 2, p. 59–66.

[104] E. Kalamaras, P. Lianos, Current Doubling effect revisited: Current multiplication in a PhotoFuelCell, *J. Electroanal. Chem.* 2015, 751, p. 37–42.

[105] S. Palmas, A. Da Pozzo, M. Mascia, A. Vacca, R. Matarrese, Investigation on the Adsorption and Photooxidation of Glycerol at TiO_2 Nanotubular Arrays, *Int. J. Photoenergy*. 2012, 2012, p. 1–7.

[106] S. Palmas, A. Da Pozzo, M. Mascia, A. Vacca, P.C. Ricci, R. Matarrese, On the redox behaviour of glycerol at TiO_2 electrodes, *J. Solid State Electrochem.* 2012, 16, p. 2493–2502.

[107] K. Carlson, C. Elliott, S. Walker, M. Misra, S. Mohanty, An Effective, Point-of-Use Water Disinfection Device Using Immobilized Black TiO_2 Nanotubes as an Electrocatalyst, *J. Electrochem. Soc.* 2016, 163, p. H395–H401.

[108] I. Mintsouli, N. Philippidis, I. Poulios, S. Sotiropoulos, Photoelectrochemical characterisation of thermal and particulate titanium dioxide electrodes, *J. Appl. Electrochem.* 2006, 36, p. 463–474.

[109] D. Patel, K.R. Chauhan, I. Mukhopadhyay, Revealing the Charge Transport Mechanism of a Photoelectrochemical cell: Analysis by A.C. voltage perturbation, *Phys. Chem. Chem. Phys.* 2014, 16, p. 20900–20908.

[110] M.I. Díez-García, T. Lana-Villarreal, R. Gómez, Study of Copper Ferrite as a Novel Photocathode for Water Reduction: Improving Its Photoactivity by Electrochemical Pretreatment, *ChemSusChem*. 2016, 9, p. 1504–1512.

[111] Z. Chen, H.N. Dinh, E. Miller, Photoelectrochemical water splitting standards, experimental methods, and protocols, 2013.

[112] N.H. Tran, G.S.K. Kannangara, Conversion of glycerol to hydrogen rich gas., *Chem. Soc. Rev.* 2013, 42, p. 9454–79.

[113] M. Li, Y. Li, S. Peng, G. Lu, S. Li, Photocatalytic hydrogen generation using glycerol wastewater over Pt/TiO_2, *Front. Chem. China*. 2009, 4, p. 32–38.

[114] Q. Liu, J. He, T. Yao, Z. Sun, W. Cheng, S. He, Y. Xie, Y. Peng, H. Cheng, Aligned Fe_2TiO_5-containing nanotube arrays with low onset potential for visible-light water oxidation, *Nat. Commun.* 2014, 5, p. 1–7.

[115] P.S. Bassi, R.P. Antony, P.P. Boix, Y. Fang, J. Barber, L.H. Wong, Crystalline Fe_2O_3/Fe_2TiO_5 heterojunction nanorods with efficient charge separation and hole injection as photoanode for solar water oxidation, *Nano Energy*. 2016, 22, p. 310–318.

[116] N. Sijakovic-Vujicic, M. Ivanda, M. Gotic, S. Music, S. Popovic, Synthesis and Microstructural Properties of Fe-TiO_2 Nanocrystalline Particles Obtained

by a Modified Sol-Gel Method, *J. Sol-Gel Sci. Technol.* 2004, 30, p. 5–19.

[117] M. Pham, Visible light induced hydrogen generation using a hollow photocatalyst with two cocatalysts separated on two surface sides †, 2014, p. 5937–5941.

[118] D. Monllor–Satoca, M. Bärtsch, C. Fàbrega, A. Genç, S. Hilaire, T. Andreu, J. Arbiol, M. Niederberger, J.R. Morante, What Do you Do, Titanium? Insight into the Role of Titanium Oxide as Water Oxidation Promoter in Hematite-based Photoanodes, *Energy Environ. Sci.* 2015, 8, p. 3242–3254.

[119] K. Elghniji, A. Atyaoui, S. Livraghi, L. Bousselmi, E. Giamello, M. Ksibi, Synthesis and characterization of Fe^{3+} doped TiO_2 nanoparticles and films and their performance for photocurrent response under UV illumination, *J. Alloys Compd.* 2012, 541, p. 421–427.

[120] L. Sun, J. Li, C.L. Wang, S.F. Li, H.B. Chen, C.J. Lin, An electrochemical strategy of doping Fe^{3+} into TiO_2 nanotube array films for enhancement in photocatalytic activity, *Sol. Energy Mater. Sol. Cells*. 2009, 93, p. 1875–1880.

BIBLIOGRAPHY

A. Esfandiar, S. Ghasemi, A. Irajizad, O. Akhavan, M.R. Gholami, The decoration of TiO_2/reduced graphene oxide by Pd and Pt nanoparticles for hydrogen gas sensing, Int. J. Hydrogen Energy. 2012, 37, p. 15423–15432.

A. Glisenti, The reactivity of a Fe-Ti-O mixed oxide under different atmospheres: Study of the interaction with simple alcohol molecules, J. Mol. Catal. A Chem. 2000, 153, p. 169–190.

A. Grosvenor, B. Kobe, M. Biesinger, N. McIntyre, Investigation of multiplet splitting of Fe 2p XPS spectra and bonding in iron compounds, Surf. Interface Anal. 2004, 36, p. 1564–1574.

A. Hunyek, C. Sirisathitkul, P. Harding, D.J. Harding, Structural and magnetic properties of cobalt ferrites synthesized using sol-gel techniques, Mater. Sci. 2012, 30, p. 278–281.

A. John K, J. Naduvath, S. Mallick, T. Shripathi, M. Thankamoniamma, R.R. Philip, A novel cost effective fabrication technique for highly preferential oriented TiO_2 nanotubes, Nanoscale. 2015, 7, p. 20386–20390.

A. Nairan, M. Khan, U. Khan, M. Iqbal, S. Riaz, S. Naseem, Temperature-Dependent Magnetic Response of Antiferromagnetic Doping in Cobalt Ferrite Nanostructures, Nanomaterials. 2016, 6, p. 73.

A. Selloni, Anatase shows its reactive side. Fluorine-containing species can cause titania to crystallize with an unusually large fraction of reactive {001} facets, Nat. Mater. 2008, 7, p. 613–615.

A. Walsh, K. Ahn, S. Shet, M. Huda, T. Deutsch, H. Wang, J. Turner, S.-H. Wei, Y. Yan, M. Al-Jassim, Ternary cobalt spinel oxides for solar driven hydrogen production: Theory and experiment, Energy Environ. Sci. 2009, 2, p. 774–782.

A.M. Mohamed, A.S. Aljaber, S.Y. AlQaradawi, N.K. Allam, TiO2 nanotubes with ultrathin walls for enhanced water splitting, Chem. Commun. (Camb). 2015, 51, p. 12617–20.

A.P. Amaliya, S. Anand, S. Pauline, CTAB Assisted Synthesis of Cobalt Ferrite Nanoparticles and Its Characterizations, J. Nanosci. Technol. 2016, 2, p. 186–188.

B. Kumar, M. Asadi, D. Pisasale, S. Sinha-ray, B.A. Rosen, R. Haasch, J. Abiade, A.L. Yarin, A. Salehi-khojin, Renewable and metal-free carbon nanofibre catalysts for carbon dioxide reduction, Nat. Commun. 2013, 4, p. 2819.

B.L. Sharma, R.K. Purohit, Semiconductor Heterojunctions, Pergamon, 1974.

B.S. Holinsworth, D. Mazumdar, H. Sims, Q. Sun, M.K. Yurtisigi, S.K. Sarker, A. Gupta, W.H. Butler, J.L. Musfeldt, Chemical tuning of the optical band gap in spinel ferrites: $CoFe_2O_4$ vs $NiFe_2O_4$, Appl. Phys. Lett. 2013, 103.

B.X. Lei, W. Sun, Z.F. Sun, Synthesis of visible-light absorbing $CoFe_2O_4$ sensitized TiO_2 nanotube arrays electrode with enhanced photoelectrochemical performance, Mater. Res. Bull. 2013, 48, p. 3625–3629.

C. Chen, W. Cai, M. Long, B. Zou, Y. Wu, D. Wu, Y. Feng, Synthesis of Visible-Light Responsive Graphene Oxide/TiO_2 Composites with p/n Heterojunction, ACS Nano. 2010, 4, p. 6425–6432.

C. Du, X. Yang, M.T. Mayer, H. Hoyt, J. Xie, G. McMahon, G. Bischoping, D. Wang, Hematite-based water splitting with low turn-on voltages, Angew. Chemie - Int. Ed. 2013, 52, p. 12692–12695.

C. Haw, W. Chiu, S. Abdul Rahman, P. Khiew, S. Radiman, R. Abdul Shukor, M.A. Hamid, N. Ghazali, The design of new magnetic-photocatalyst nanocomposites ($CoFe_2O_4$–TiO_2) as smart nanomaterials for recyclable-photocatalysis applications, New J. Chem. 2016, 40, p. 1124–1136.

C. Karunakaran, P. Anilkumar, P. Gomathisankar, Photoproduction of iodine with nanoparticulate semiconductors and insulators, Chem. Cent. J. 2011, 5, p. 1–9.

C. Li, J. Wang, B. Wang, J. Gong, Z. Lin, A novel magnetically separable TiO_2/$CoFe_2O_4$ nanofiber with high photocatalytic activity under UV-vis light, Mater. Res. Bull. 2012, 47, p. 333–337.

D. Dreyer, S. Park, C. Bielawski, R. Ruoff, The chemistry of graphene oxide, Chem. Soc. Rev. 2010, 39, p. 228–240.

D. Monllor–Satoca, M. Bärtsch, C. Fàbrega, A. Genç, S. Hilaire, T. Andreu, J. Arbiol, M. Niederberger, J.R. Morante, What Do you Do, Titanium? Insight into the Role of Titanium Oxide as Water Oxidation Promoter in Hematite-based Photoanodes, Energy Environ. Sci. 2015, 8, p. 3242–3254.

D. Patel, K.R. Chauhan, I. Mukhopadhyay, Revealing the Charge Transport Mechanism of a Photoelectrochemical cell: Analysis by A.C. voltage perturbation, Phys. Chem. Chem. Phys. 2014, 16, p. 20900–20908.

D. Ramírez-ortega, A.M. Meléndez, P. Acevedo-Peña, I. González, R. Arroyo, Semiconducting properties of ZnO/TiO_2 composites by electrochemical

measurements and their relationship with photocatalytic activity, Electrochim. Acta. 2014, 140, p. 541–549.

D. Sharma, N. Khare, Tuning of optical bandgap and magnetization of $CoFe_2O_4$ thin films, Appl. Phys. Lett. 2014, 105, p. 1–5.

D.A. Keane, K.G. McGuigan, P. Fernández Ibáñez, M.I. Polo-López, A.J. Byrne, P. Dunlop, K. O'Shea, D. Dionysiou, S. Pillai, Solar photocatalysis for water disinfection : Materials and reactor design, Catal. Sci. Technol. 2014, 4, p. 1211–1226.

D.H. Taffa, R. Dillert, A.C. Ulpe, K. Bauerfeind, T. Bredow, D. Bahnemann, M. Wark, Photoelectrochemical and theoretical investigations of spinel type ferrites ($M_xFe_{3-x}O_4$) for water splitting: a mini-review, J. Photonics Energy. 2016, 7, p. 1–24.

E. Kalamaras, P. Lianos, Current Doubling effect revisited: Current multiplication in a PhotoFuelCell, J. Electroanal. Chem. 2015, 751, p. 37–42.

G.M. Ingo, S. Dirè, F. Babonneau, XPS studies of SiO_2-TiO_2, powders prepared by sol-gel process, Appl. Surf. Sci. 1993, 710, p. 230–234.

H. Cid, L. Argüello, A. Romano, C. Flores, M. Pérez, Síntesis y Caracterización de Grafeno, Cent. Física Apl. Y Tecnol. Av. 2012.

H. Ghandoor, H. Zidan, M. Khalil, M. Ismail, Synthesis and Some Physical Properties of Magnetite (Fe_3O_4) Nanoparticles, Int. J. Electrochem. Sci. 2012, 7, p. 5734–5745.

H. Nolan, B. Mendoza-Sanchez, N. Ashok Kumar, N. McEvoy, S. O'Brien, V. Nicolosi, G.S. Duesberg, Nitrogen-doped reduced graphene oxide electrodes for electrochemical supercapacitors., Phys. Chem. Chem. Phys. 2014, 16, p. 2280–2284.

H. Wang, L. Zhang, Z. Chen, J. Hu, S. Li, Z. Wang, J. Liu, X. Wang, Semiconductor heterojunction photocatalysts: design, construction, and photocatalytic performances, Chem. Soc. Rev. 2014, 43, p. 5234–44.

H.A. Becerril, J. Mao, Z. Liu, R.M. Stoltenberg, Z. Bao, Y. Chen, Evaluation of Solution-Processed Reduced Graphene Oxide Films as Transparent Conductors, ACS Nano. 2008, 2, p. 463–470.

H.C. Liang, X.Z. Li, Effects of structure of anodic TiO_2 nanotube arrays on photocatalytic activity for the degradation of 2,3-dichlorophenol in aqueous solution, J. Hazard. Mater. 2009, 162, p. 1415–1422.

H.U. Harten, The Semiconductor/Electrolyte Interface: Potentials, Charges and Carriers, Electrochim. Acta. 1968, 13, p. 1255–1261.

H.W. Tan, A.R. Abdul Aziz, M.K. Aroua, Glycerol production and its applications as a raw material: A review, Renew. Sustain. Energy Rev. 2013, 27, p. 118–127.

I. Gómez, E. Mejía, R. Cabanzo, Synthesis of Graphene Oxide and Chemically Reduced Graphene Nanosheets, Rev. Colomb. Mater. 2013, 5, p. 177–184.

I. Mintsouli, N. Philippidis, I. Poulios, S. Sotiropoulos, Photoelectrochemical characterisation of thermal and particulate titanium dioxide electrodes, J. Appl. Electrochem. 2006, 36, p. 463–474.

I. Sirés, E. Brillas, M.A. Oturan, M.A. Rodrigo, M. Panizza, Electrochemical advanced oxidation processes: today and tomorrow . A review, Environ. Sci. Pollut. Res. 2014, 21, p. 8336–8367.

J. Bisquert, A. Zaban, M. Greenshtein, I. Mora-Seró, Determination of Rate Constants for Charge Transfer and the Distribution of Semiconductor and Electrolyte Electronic Energy Levels in Dye-Sensitized Solar Cells by Open-Circuit Photovoltage Decay Method, J. Am. Chemi. 2004, 126, p. 13550–13559.

J. Luo, X. Zhou, L. Ma, X. Xu, Enhanced visible-light-driven photocatalytic activity of WO_3/BiOI heterojunction photocatalysts, J. Mol. Catal. A Chem. 2015, 410, p. 168–176.

J. Ma, A. Habrioux, Y. Luo, G. Ramos, L. Calvillo, G. Granozzi, P. Balbuena, N. Alonso-Vante, Electronic Interaction between Platinum Nanoparticles and Nitrogen-doped Reduced Graphene Oxide: Effect on the Oxygen Reduction Reaction, J. Mater. Chem. A. 2013, p. 1–15.

J. Nowotny, M.A. Alim, T. Bak, M.A. Idris, M. Ionescu, K. Prince, M.Z. Sahdan, K. Sopian, M. Teridi, W. Sigmund, Defect chemistry and defect engineering of TiO_2-based semiconductors for solar energy conversion, Chem. Soc. Rev. 2015.

J. Yu, G. Dai, Q. Xiang, M. Jaroniec, Fabrication and enhanced visible-light photocatalytic activity of carbon self-doped TiO_2 sheets with exposed {001} facets, J. Mater. Chem. 2011, 21, p. 1049–1057.

J.P. Pineda Martínez, J.Z. Rojas Cristancho, Factores que afectan la polimerización del glicerol crudo para la producción de poliglicerol, Universidad Industrial de Santander, 2013.

K. Carlson, C. Elliott, S. Walker, M. Misra, S. Mohanty, An Effective, Point-of-Use Water Disinfection Device Using Immobilized Black TiO_2 Nanotubes as an Electrocatalyst, J. Electrochem. Soc. 2016, 163, p. H395–H401.

K. Dai, T. Peng, D. Ke, B. Wei, Photocatalytic hydrogen generation using a nanocomposite of multi-walled carbon nanotubes and TiO_2 nanoparticles under visible light irradiation, Nanotechnology. 2009, 20, p. 1–6.

K. Djebaili, Z. Mekhalif, A. Boumaza, A. Djelloul, XPS, FTIR, EDX, and XRD Analysis of Al_2O_3 Scales Grown on PM2000 Alloy, J. Spectrosc. 2015, p. 1–14.

K. Elghniji, A. Atyaoui, S. Livraghi, L. Bousselmi, E. Giamello, M. Ksibi, Synthesis and characterization of Fe^{3+} doped TiO_2 nanoparticles and films and their performance for photocurrent response under UV illumination, J. Alloys Compd. 2012, 541, p. 421–427.

K. Liang, X. Chen, Z. Guo, T. Hou, X. Zhang, Y. Li, Lithium intercalation and diffusion in TiO_2 nanotubes: a first-principles investigation, Phys. Chem. Chem. Phys. 2016, 18, p. 24370–24376.

K. Siuzdak, M. Szkoda, M. Sawczak, A. Lisowska-Oleksiak, Novel nitrogen precursors for electrochemically driven doping of titania nanotubes exhibiting enhanced photoactivity, New J. Chem. 2015, 39, p. 2741–2751.

K.S. Raja, V.K. Mahajan, M. Misra, Determination of photo conversion efficiency of nanotubular titanium oxide photo-electrochemical cell for solar hydrogen generation, J. Power Sources. 2006, 159, p. 1258–1265.

K.V. Sankar, R.K. Selvan, D. Meyrick, Electrochemical performances of $CoFe_2O_4$ nanoparticles and rGO based asymmetric supercapacitor, RSC Adv. 2015, 5, p. 99959–99967.

L. Sun, J. Li, C.L. Wang, S.F. Li, H.B. Chen, C.J. Lin, An electrochemical strategy of doping Fe^{3+} into TiO_2 nanotube array films for enhancement in photocatalytic activity, Sol. Energy Mater. Sol. Cells. 2009, 93, p. 1875–1880.

L. Zhang, J.C. Yu, Z. Zheng, C.W. Leung, Fabrication of hierarchical porous iron oxide films utilizing the Kirkendall effect, Chem. Commun. 2005, p. 2683–2685.

M. Aleksandrzak, P. Adamski, W. Kukułka, B. Zielinska, E. Mijowska, Effect of graphene thickness on photocatalytic activity of TiO_2-graphene nanocomposites, Appl. Surf. Sci. 2015, 331, p. 193–199.

M. Batzill, E.H. Morales, U. Diebold, Influence of nitrogen doping on the defect formation and surface properties of TiO_2 rutile and anatase, Phys. Rev. Lett. 2006, 96, p. 1–4.

M. Law, L.E. Greene, J.C. Johnson, R. Saykally, P. Yang, Nanowire dye-sensitized solar cells, Nat. Mater. 2005, 4, p. 455–459.

M. Li, Y. Li, S. Peng, G. Lu, S. Li, Photocatalytic hydrogen generation using glycerol wastewater over Pt/TiO_2, Front. Chem. China. 2009, 4, p. 32–38.

M. Pham, C. Dinh, G. Vuong, N. Ta, T. Do, Visible light induced hydrogen generation using a hollow photocatalyst with two cocatalysts separated on two surface sides †, Phys. Chem. Chem. Phys. 2014, 16, p. 5937–5941.

M. Pham, Visible light induced hydrogen generation using a hollow photocatalyst with two cocatalysts separated on two surface sides †, 2014, p. 5937–5941.

M. Xing, X. Li, J. Zhang, Synergistic effect on the visible light activity of Ti(3+) doped TiO_2 nanorods/boron doped graphene composite., Sci. Rep. 2014, 4, p. 5493.

M.H. Habibi, H.J. Parhizkar, FTIR and UV-vis diffuse reflectance spectroscopy studies of the wet chemical (WC) route synthesized nano-structure $CoFe_2O_4$ from $CoCl_2$ and $FeCl_3$, Spectrochim. Acta - Part A Mol. Biomol. Spectrosc. 2014, 127, p. 102–106.

M.I. Díez-García, T. Lana-Villarreal, R. Gómez, Study of Copper Ferrite as a Novel Photocathode for Water Reduction: Improving Its Photoactivity by Electrochemical Pretreatment, ChemSusChem. 2016, 9, p. 1504–1512.

N. Plylahan, S. Maria, T.N. Phan, M. Letiche, H. Martinez, C. Courrèges, P. Knauth, T. Djenizian, Enhanced electrochemical performance of Lithium-ion batteries by conformal coating of polymer electrolyte, Nanoscale Res. Lett. 2014, 9, p. 544.

N. Sanpo, A. Siao, M. Ang, F. Hasan, J. Wang, C.C. Berndt, Phases and microstructures of solution precursor plasma sprayed cobalt ferrite splats, in: Proc. 5th Asian Therm. Spray Conf., 2012: pp. 145–146.

N. Sanpo, C. Wen, C. Berndt, J. Wang, Advanced functional materials: Multifunctional Spinel Ferrite Nanoparticles for Biomedical Application, in: Adv. Funct. Mater., Lokman Uzun, Tiwari Ashutosh, Wiley, 2015: pp. 202–203.

N. Sijakovic-Vujicic, M. Ivanda, M. Gotic, S. Music, S. Popovic, Synthesis and Microstructural Properties of Fe-TiO_2 Nanocrystalline Particles Obtained by a Modified Sol-Gel Method, J. Sol-Gel Sci. Technol. 2004, 30, p. 5–19.

N.H. Tran, G.S.K. Kannangara, Conversion of glycerol to hydrogen rich gas., Chem. Soc. Rev. 2013, 42, p. 9454–79.

N.V. Long, Y. Yang, T. Teranishi, C.M. Thi, Y. Cao, M. Nogami, Related magnetic properties of $CoFe_2O_4$ cobalt ferrite particles synthesised by the polyol method with $NaBH_4$ and heat treatment: new micro and nanoscale structures, RSC Adv. 2015, 5, p. 56560–56569.

Ó.J. Martínez Santana, Y.A. Zorro Gutiérrez, Estudio de las variables de síntesis de poliuretanos a partir de aceite de ricino y glicerol crudo, Universidad Industrial de Santander, 2014.

O.N. Shebanova, P. Lazor, Raman spectroscopic study of magnetite ($FeFe_2O_4$): A new assignment for the vibrational spectrum, J. Solid State Chem. 2003, 174, p. 424–430.

P. Chandramohan, M.P. Srinivasan, S. Velmurugan, S.V. Narasimhan, Cation distribution and particle size effect on Raman spectrum of $CoFe_2O_4$, J. Solid State Chem. 2011, 184, p. 89–96.

P. Karthika, Functionalized Exfoliated Graphene Oxide as Supercapacitor Electrodes, Soft Nanosci. Lett. 2012, 2, p. 59–66.

P. Mazierski, M. Nischk, M. Gołkowska, W. Lisowski, M. Gazda, M. Winiarski, T. Klimczuk, A. Zaleska-medynska, Photocatalytic activity of nitrogen doped TiO_2

nanotubes prepared by anodic oxidation: The effect of applied voltage, anodization time and amount of nitrogen dopant, Appl. Catal. B Environ. 2016, 196, p. 77–88.

P. Raju, S.R. Murthy, Microwave-hydrothermal synthesis of $CoFe_2O_4$ - TiO_2 nanocomposites, Adv. Mater. Lett. 2013, 4, p. 99–105.

P. Sathishkumar, R. Mangalaraja, S. Anandan, M. Ashokkumar, $CoFe_2O_4/TiO_2$ nanocatalysts for the photocatalytic degradation of Reactive Red 120 in aqueous solutions in the presence and absence of electron acceptors, Chem. Eng. J. 2013, 220, p. 302–310.

P. Song, X. Zhang, M. Sun, X. Cui, Y. Lin, Graphene oxide modified TiO_2 nanotube arrays: enhanced visible light photoelectrochemical properties, Nanoscale. 2012, 4, p. 1800.

P. Wang, H. Wu, Y. Tang, R. Amal, Y.H. Ng, Electrodeposited Cu_2O as Photoelectrodes with Controllable Conductivity Type for Solar Energy Conversion, J. Phys. Chem. C. 2015, 119, p. 26275–26282.

P.S. Bassi, R.P. Antony, P.P. Boix, Y. Fang, J. Barber, L.H. Wong, Crystalline Fe_2O_3/Fe_2TiO_5 heterojunction nanorods with efficient charge separation and hole injection as photoanode for solar water oxidation, Nano Energy. 2016, 22, p. 310–318.

Q. Li, J.K. Shang, Self-Organized Nitrogen and Fluorine Co-doped Titanium Oxide Nanotube Arrays with Enhanced Visible Light Photocatalytic Performance, Environ. Sci. Technol. 2009, 43, p. 8923–8929.

Q. Liu, J. He, T. Yao, Z. Sun, W. Cheng, S. He, Y. Xie, Y. Peng, H. Cheng, Aligned Fe2TiO5-containing nanotube arrays with low onset potential for visible-light water oxidation, Nat. Commun. 2014, 5, p. 1–7.

R. Jung, H. Tsuchiya, S. Fujimoto, XPS characterization of passive films formed on Type 304 stainless steel in humid atmosphere, Corros. Sci. 2012, 58, p. 62–68.

R. Memming, Solar Energy Conversion By Photoelectrochemical Processes, Electrochim. Acta. 1980, 25, p. 77–88.

R.A. Bepari, P. Bharali, B.K. Das, Controlled synthesis of α- and γ-Fe_2O_3 nanoparticles via thermolysis of PVA gels and studies on γ-Fe_2O_3 catalyzed styrene epoxidation, J. Saudi Chem. Soc. 2014.

S. Hejazi, N.T. Nguyen, A. Mazare, P. Schmuki, Aminated TiO_2 nanotubes as a photoelectrochemical water splitting photoanode, Catal. Today. 2016.

S. Palmas, A. Da Pozzo, M. Mascia, A. Vacca, P.C. Ricci, R. Matarrese, On the redox behaviour of glycerol at TiO_2 electrodes, J. Solid State Electrochem. 2012, 16, p. 2493–2502.

S. Palmas, A. Da Pozzo, M. Mascia, A. Vacca, R. Matarrese, Investigation on the Adsorption and Photooxidation of Glycerol at TiO_2 Nanotubular Arrays, Int. J. Photoenergy. 2012, 2012, p. 1–7.

S. Shen, J. Jiang, P. Guo, L. Guo, Facile Growth of Porous Hematite Films for Photoelectrochemical Water Splitting, Int. J. Photoenergy. 2013, p. 1–9.

S. Umrao, S. Abraham, F. Theil, S. Pandey, V. Ciobota, P. Shukla, C. Rupp, S. Chakraborty, R. Ahuja, J. Popp, B. Dietzek, A. Srivastava, A possible mechanism

for the emergence of an additional band gap due to a Ti–O–C bond in the TiO_2–graphene hybrid system for enhanced photodegradation of methylene blue under visible light, RSC Adv. 2014, 4, p. 59890–59901.

S.A. Pawar, D.S. Patil, U.T. Pawar, R.S. Devan, M.M. Karanjkar, Y.R. Ma, S.W. Shin, J.H. Kim, P.S. Patil, Photoelectrochemical solar cell based on surfactant mediated rutile TiO_2 nanorods, J. Mater. Sci. Mater. Electron. 2015, 26, p. 2595.

S.W. Shin, J.Y. Lee, K. Ahn, S.H. Kang, J.H. Kim, Visible Light Absorbing TiO_2 Nanotube Arrays by Sulfur Treatment for Photoelectrochemical Water Splitting, J. Phys. Chem. C. 2015, 119, p. 13375–13383.

T. Fujii, F. Groot, G. Sawatzky, In situ XPS analysis of various iron oxide films grown by NO_2-assisted molecular-beam epitaxy, Phys. Rev. B. 1999, 59, p. 3195–3202.

T. Ochiai, A. Fujishima, Photoelectrochemical properties of TiO_2 photocatalyst and its applications for environmental purification, J. Photochem. Photobiol. C Photochem. Rev. 2012, 13, p. 247–262.

T. Peng, K. Li, P. Zeng, Q. Zhang, X. Zhang, Enhanced Photocatalytic Hydrogen Production over Graphene Oxide−Cadmium Sulfide Nanocomposite under Visible Light Irradiation, J. Phys. Chem. C. 2012, 116, p. 22720–22726.

T. Yeh, J. Cihlar, C. Chang, C. Cheng, H. Teng, Roles of graphene oxide in photocatalytic water splitting, Mater. Today. 2013, 16, p. 78–84.

T.A. Egerton, P.A. Christensen, Advanced Oxidation Processes for Water and Wastewater Treatment, Simons Par, IWA, 2004.

T.-F. Yeh, J. Cihlář, C.-Y. Chang, C. Cheng, H. Teng, Roles of graphene oxide in photocatalytic water splitting, Mater. Today. 2013, 16, p. 78–84.

V. Nguyen, M. Gauthier, O. Sandre, Templated Synthesis of Magnetic Nanoparticles through the Self-Assembly of Polymers and Surfactants, Nanomaterials. 2014, 4, p. 628–685.

V. Stengl, S. Bakardjieva, T.M. Grygar, J. Bludská, M. Kormunda, TiO_2-graphene oxide nanocomposite as advanced photocatalytic materials, Chem. Cent. J. 2013, 7.

W. Peternele, V. Monge Fuentes, M.L. Fascineli, J. Rodrigues Da Silva, R. Silva, C. Lucci, R. Bentes De Azevedo, Experimental Investigation of the Coprecipitation Method: An Approach to Obtain Magnetite and Maghemite Nanoparticles with Improved Properties, J. Nanomater. 2014.

W.S. dos Santos, M. Rodriguez, A.S. Afonso, J.P. Mesquita, L.L. Nascimento, A.O. Patrocínio, A.C. Silva, L.C. Oliveira, J.D. Fabris, M.C. Pereira, A hole inversion layer at the $BiVO_4/Bi_4V_2O_{11}$ interface produces a high tunable photovoltage for water splitting, Sci. Rep. 2016, 6.

W.S. Tung, W.A. Daoud, New Approach Toward Nanosized Ferrous Ferric Oxide and Fe_3O_4-doped Titanium Dioxide Photocatalysts., ACS Appl. Mater. Interfaces. 2009, 1, p. 2453–2461.

X. Liu, Y. Zhang, T. Wu, J. Huang, Hierarchical nanotubular titanium nitride derived from natural cellulose substance and its electrochemical properties, Chem. Commun. 2012, 48, p. 9992–9994.

X. Yang, C. Cao, L. Erickson, K. Hohn, R. Maghirang, K. Klabunde, Photo-catalytic degradation of Rhodamine B on C-, S-, N-, and Fe-doped TiO_2 under visible-light irradiation, Appl. Catal. B Environ. 2009, 91, p. 657–662.

Y. Deng, R. Zhao, Advanced Oxidation Processes (AOPs) in Wastewater Treatment, Curr. Pollut. Reports. 2015, 1, p. 167–176.

Y. Fu, H. Chen, X. Sun, X. Wang, Combination of cobalt ferrite and graphene: High-performance and recyclable visible-light photocatalysis, Appl. Catal. B Environ. 2012, 111–112, p. 280–287.

Y. Hou, X.Y. Li, Q.D. Zhao, X. Quan, G.H. Chen, Electrochemical Method for Synthesis of a $ZnFe_2O_4/TiO_2$ Composite Nanotube Array Modified Electrode with Enhanced Photoelectrochemical Activity, Adv. Funct. Mater. 2010, 20, p. 2165–2174.

Y. Lai, L. Sun, Y. Chen, H. Zhuang, C. Lin, J.W. Chin, Effects of the Structure of TiO_2 Nanotube Array on Ti Substrate on Its Photocatalytic Activity, J. Electrochem. Soc. 2006, 153, p. D123–D127.

Y. Lin, Y. Xu, M. Mayer, Z. Simpson, G. McMahon, S. Zhou, D. Wang, Growth of p-Type Hematite by Atomic Layer Deposition and Its Utilization for Improved Solar Water Splitting, J. Am. Chem. Soc. 2012, 134, p. 5508–5511.

Y. Tang, C. Lee, J. Xu, Z. Liu, Z. Chen, Z. He, Y. Cao, G. Yuan, H. Song, L. Chen, L. Luo, H. Cheng, W. Zhang, I. Bello, S. Lee, Incorporation of Graphenes in Nanostructured TiO_2 Films via Molecular Grafting for Dye-Sensitized Solar Cell Application, ACS Nano. 2010, 4, p. 3482–3488.

Y. Xie, T. Wang, O. Franklin, P. Sherwood, X-Ray Photoelectron Spectroscopic Studies of Carbon Fiber Surfaces. Part XVI: Core-Level and Valence-Band Studies of Pitch-Based Fibers Electrochemically Treated in Ammonium Carbonate Solution, Appl. Spectrosc. 1992, 46, p. 645–651.

Y.C. Lin, C.Y. Lin, P.W. Chiu, Controllable graphene N-doping with ammonia plasma, Appl. Phys. Lett. 2010, 96.

Y.H. Hou, Y.J. Zhao, Z.W. Liu, H.Y. Yu, X.C. Zhong, W.Q. Qiu, D.C. Zeng, L.S. Wen, Structural, electronic and magnetic properties of partially inverse spinel $CoFe_2O_4$: a first-principles study, J. Phys. D. Appl. Phys. 2010, 43, p. 445003.

Y.-S. Li, J.S. Church, A.L. Woodhead, Infrared and Raman spectroscopic studies on iron oxide magnetic nano-particles and their surface modifications, J. Magn. Magn. Mater. 2012, 324, p. 1543–1550.

Z. Chen, H.N. Dinh, E. Miller, Photoelectrochemical water splitting standards, experimental methods, and protocols, 2013.

Z. Gholami, A.Z. Abdullah, K.T. Lee, Dealing with the surplus of glycerol production from biodiesel industry through catalytic upgrading to polyglycerols and other value-added products, Renew. Sustain. Energy Rev. 2014, 39, p. 327–341.

Z. Xiang, X. Zhou, G. Wan, G. Zhang, D. Cao, Improving Energy Conversion Efficiency of Dye-Sensitized Solar Cells by Modifying TiO_2 Photoanodes with Nitrogen-Reduced Graphene Oxide, ACS Sustain. Chem. Eng. 2014, 2, p. 1234–1240.

Z. Xu, C. Shen, Y. Tian, X. Shi, H. Gao, Organic phase synthesis of monodisperse iron oxide nanocrystals using iron chloride as precursor, Nanoscale. 2010, 2, p. 1027–1032.

Z. Zhou, Y. Zhang, Z. Wang, W. Wei, W. Tang, J. Shi, R. Xiong, Electronic structure studies of the spinel $CoFe_2O_4$ by X-ray photoelectron spectroscopy, Appl. Surf. Sci. 2008, 254, p. 6972–6975.

ANNEXES

ANNEX A. Crude glycerol composition supplied by Biocombustibles Sostenibles del Caribe S.A.

Element	Concentration[a]
K	46.705±3.542 mg/Kg
Na	22850±3860 mg/Kg
Ca	17.09±1.782 mg/Kg
Mg	8.616±0.684 mg/Kg
Methanol	0.01-0.5 %p/p
Glycerin	75±1.414 %p/p
Methyl fatty acid esters	63.28%
Ashes	3.489±0.424%
pH	6.135±0.05
Density	1.275±0.01 g/cm^3
Humidity	10.52±0.01 %

[a]A detailed description of the methods used in the determination of each concentration can be consulted elsewhere [32,33].

ANNEX B. Wide-scan XPS spectrum and high-resolution spectra of C 1s, N 1s, F 1s, Ti 2p and O 1s for TNT.

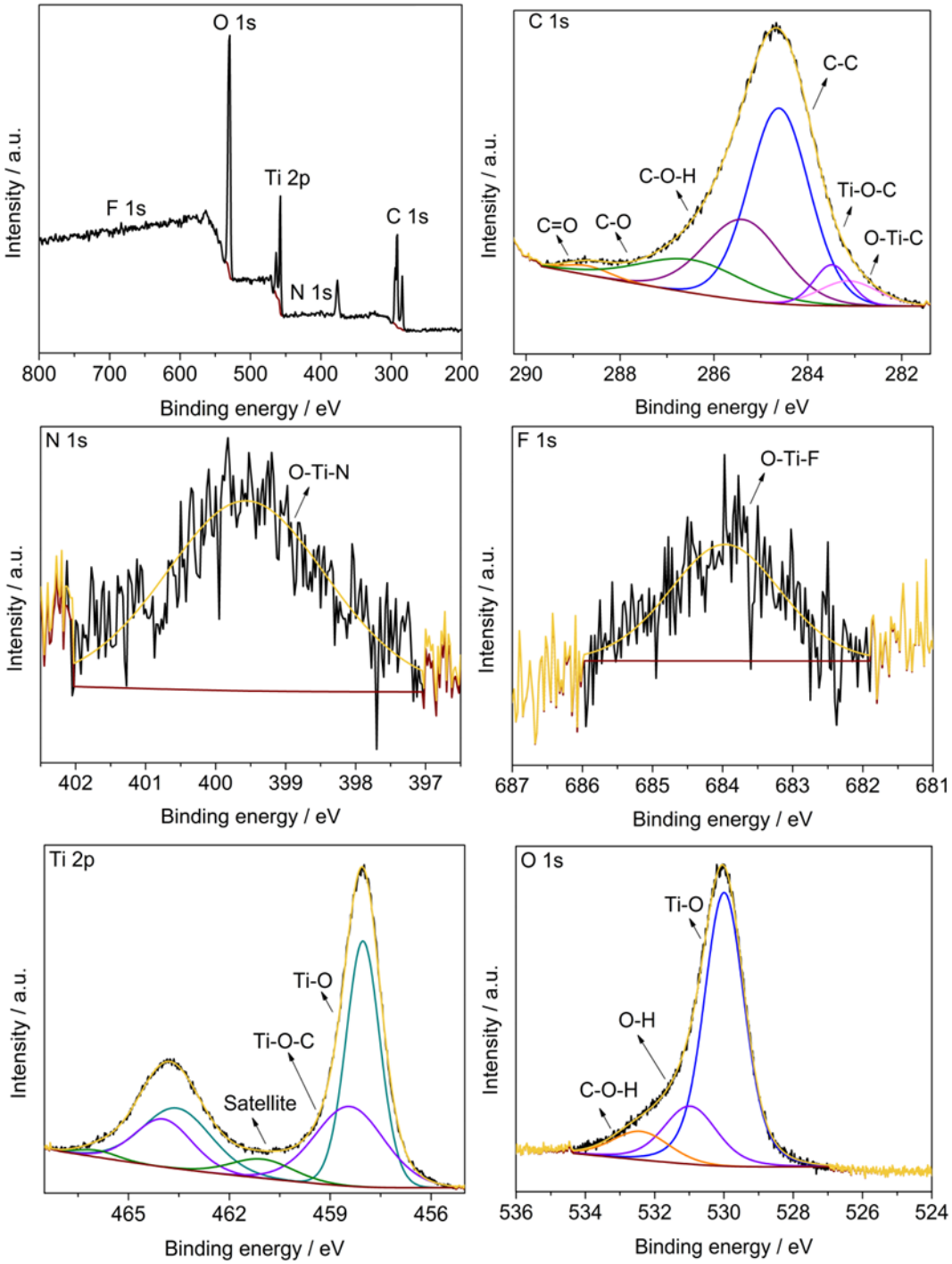

ANNEX C. Wide-scan XPS spectra of G, F and FG photoanodes, as indicated in the figure legends.

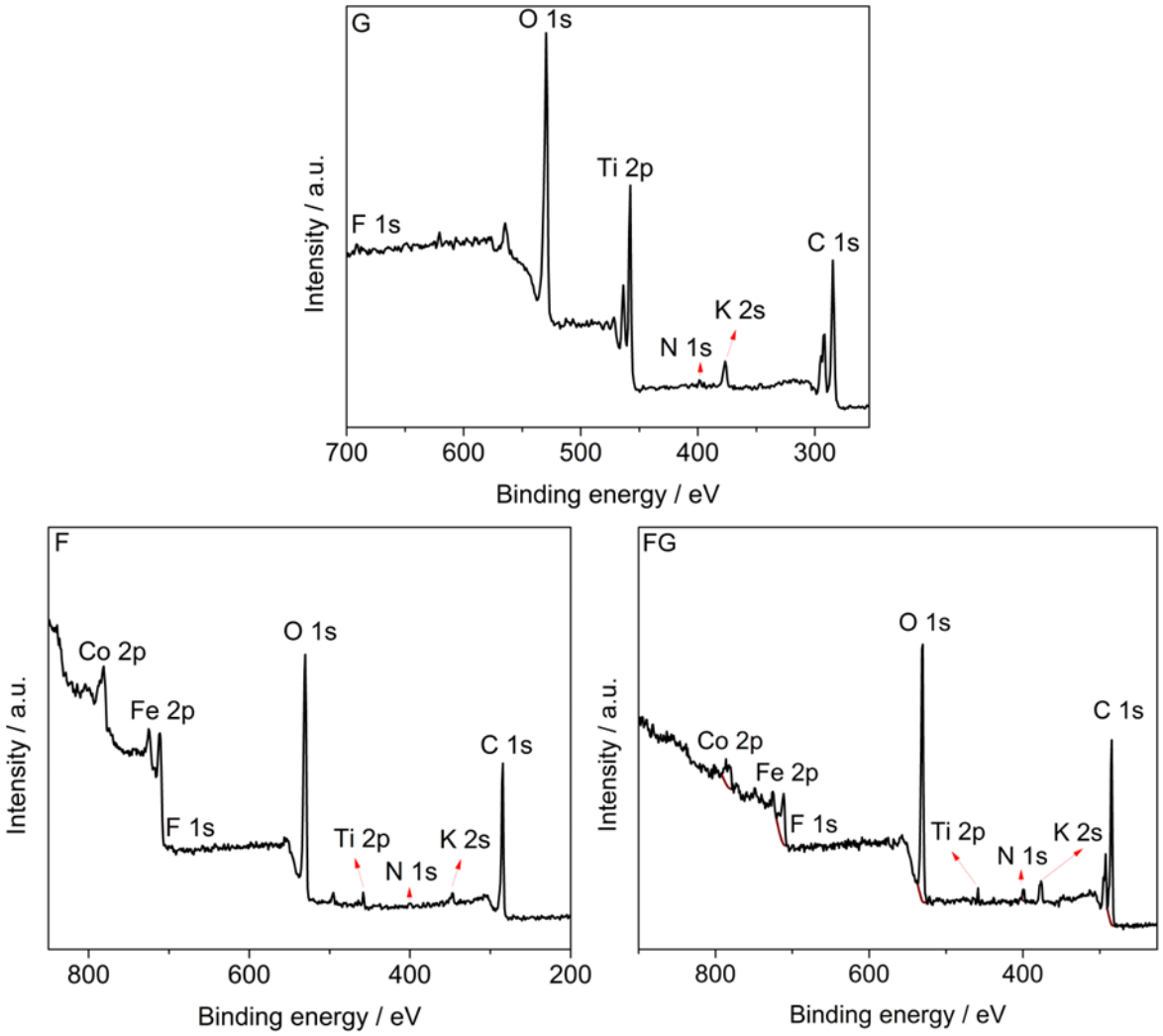

ANNEX D. Mott-Schottky equation to obtain flat band potential

Mott-Schottky plots were obtained in order to analyze the electron mobility mechanism in TNT photoanode and F photoelectrode based on charge carrier density (N_d) and flat band potential E_{fb}. The abovementioned parameters can be estimated by using the following equation:

$$\frac{1}{C_{sc}^2} = \frac{2}{N_d A^2 q \varepsilon \varepsilon_0}\left(E - E_{fb} - \frac{kT}{q}\right)$$

where C_{sc}^2 is space charge capacitance, N_d is the density of donors, A is the photoanode geometric area, q is the electron charge, ε is the relative permittivity of TiO_2 (ε=50 for anatase) and cobalt ferrite (ε=35 for $CoFe_2O_4$), ε_0 is the vacuum permittivity, k is the Boltzman constant, T is the absolute temperature in K, E is the measuring potential and E_{fb} is the flat band potential.

ANNEX E. Gas chromatography spectrum of glycerol solution at the first 20 minutes of reaction using FG photoanode under visible light illumination

```
Operator  : Elena Stashenko-UIS
Sample    : 10 MIN SLN BUFFER FOSFATO
Misc      : 10 MIN SLN BUFFER FOSFATO
ALS Vial  : 33   Sample Multiplier: 1

Search Libraries:   C:\Database\Adams.L              Minimum Quality:  75
                    C:\Database\NIST05.L             Minimum Quality:   0
                    C:\Database\wiley7n.l

Unknown Spectrum:   Apex
Integration Events: ChemStation Integrator - autoint1.e
```

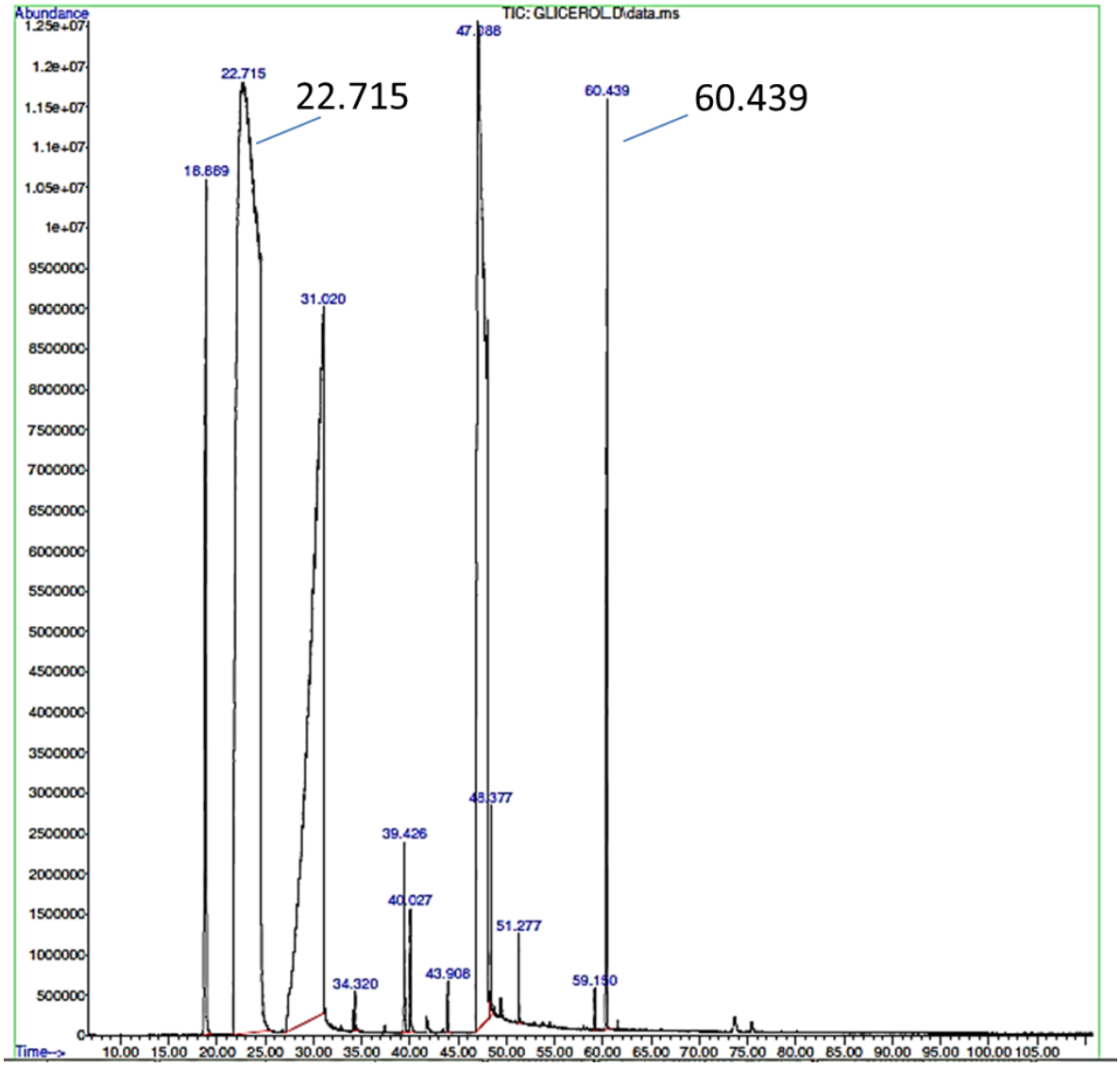

ANNEX F. Mass spectra fragmentation obtained from peaks in glycerol solution at the first 20 minutes of reaction using FG photoanode under visible light illumination

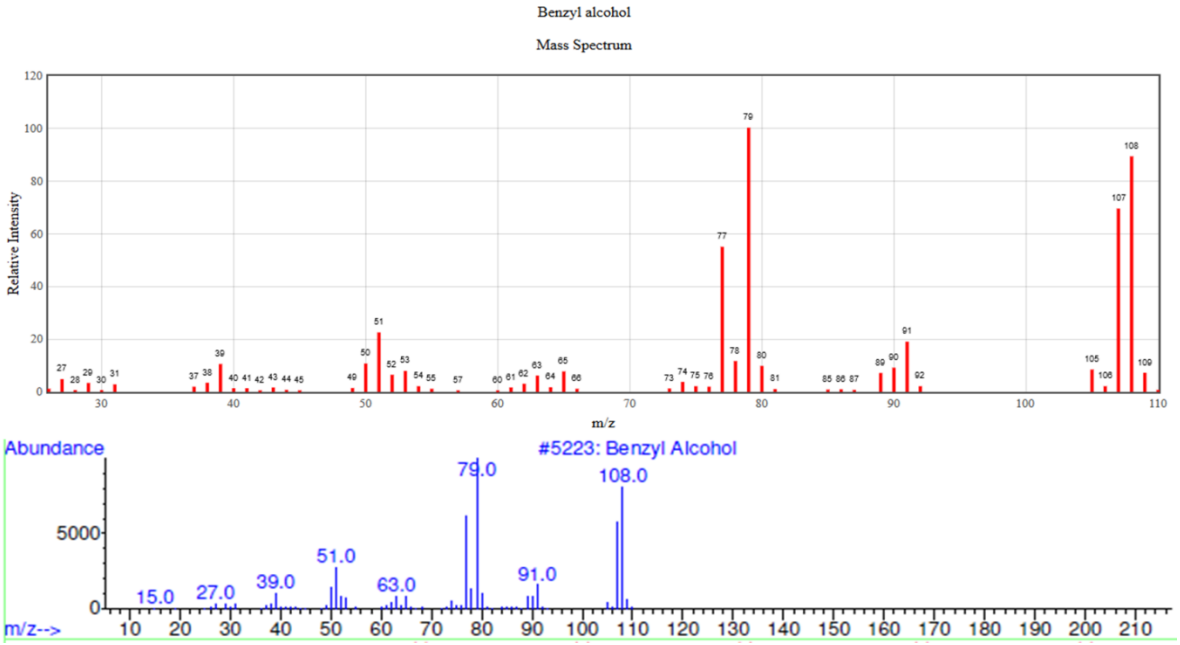

The spectrum on the top corresponds to benzyl alcohol (obtained from database NIST05). The spectrum showed down corresponds to fragmentation of peak at 22.715 minutes.

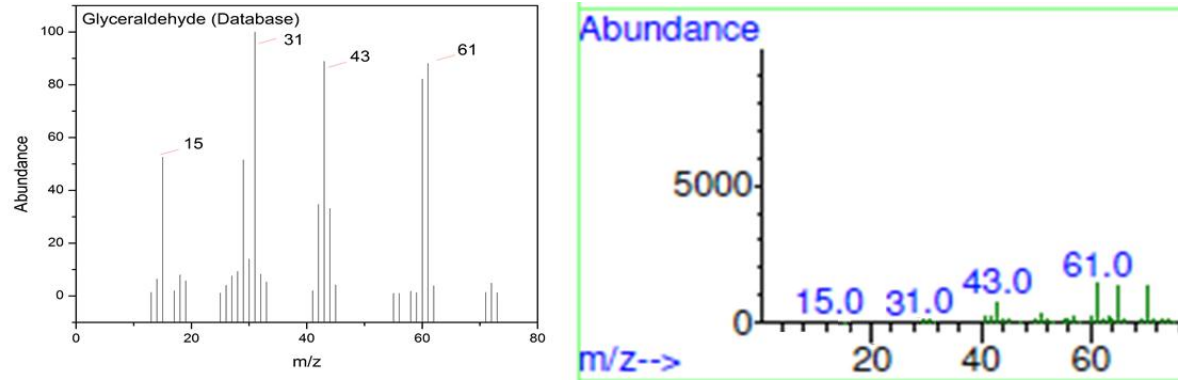

The spectrum on the top corresponds to glyceraldehyde (obtained from database http://sdbs.db.aist.go.jp/sdbs/cgi-bin/direct_frame_top.cgi). The spectrum showed down corresponds to fragmentation of peak at 60.439 minutes.